Insights into the vaccinia virus assembly mechanism provided by cellular electron cryo-tomography

von Clara Andrea Feldmann

an der Universität Hamburg eingereichte Dissertation

zur Erlangung des Doktorgrades

Fakultät für Mathematik, Informatik und Naturwissenschaften

Fachbereich Chemie

Graduate School des Leibniz Instituts für Virologie

2025 in Hamburg

Examiners

Reviewer 1:

Prof. Dr. Kay Grünewald

Reviewer 2:

Prof. Dr. Tobias Beck

Examination committee members:

Head of committee:

Prof. Dr. Kay Grünewald

Deputy Head of committee:

Prof. Dr. Maya Topf

Member:

Prof. Dr. Charlotte Uetrecht

Member:

Prof. Dr. Thomas Gerhard Dobner

Member:

Prof. Dr. Andrew Torda

Date of the defense:

July 11th 2025

Conduction of Research Work

The work for this dissertation was conducted at the Leibniz Institute of Virology (LIV) in the LIV-partner institute, the Centre for Structural Systems Biology (CSSB) in Hamburg from 15.10.2021 to 22.05.2025. This project was supervised by Prof. Dr. Kay Grünewald (Universität Hamburg, LIV) and co-supervised by Prof. Dr. Charlotte Uetrecht (Universität zu Lübeck, LIV-associated) as a co-supervisor in the LIV-Graduate School and Dr. Emmanuelle Quemin (Institute for Integrative Biology of the Cell, I2BC, CNRS UMR9198)) as an independent advisor.

Table of Contents

List of Abbreviations

ATP	adenosine triphosphate
CCC	cross-correlation coefficient
CEMOVIS	electron cryo-microscopy of vitreous sections
cryoCLEM	correlative light and electron microscopy under cryo-conditions
cryoEM	electron cryo-microscopy
cryoET	electron cryo-tomography
CSSB	Centre for Structural Systems Biology
CTF	contrast transfer function
DMEM	Dulbecco's modified Eagle medium
DMSO	dimethyl sulfoxide
dsDNA	double-stranded desoxyribonucleic acid
EM	electron microscopy
ER	endoplasmic reticulum
ERGIC	endoplasmic reticulum – Golgi - intermediate compartment
FBS	fetal bovine serum
FIB	focused ion beam
FIB-SEM	focused ion beam – scanning electron microscopy
FSC	Fourier shell correlation
GHS	globally harmonized system
HIV	human immune deficiency virus
hpi	hours post infection
iFLM	in-line fluorescence microscope
IV	immature virion
J1	jelly roll 1

J2	jelly roll 2
mito	mitochondrion
MOI	multiplicity of infection
MPXV	monkeypox virus
MV	mature virion
NCLDVs	nucleocytoplasmic large DNA viruses
NEC	nuclear egress complex
PFA	paraformaldehyde
PI	propidium iodide
pix	pixel
SEM	scanning electron microscopy
SIRT	simultaneous iterative reconstruction technique
SNR	signal-to-noise ratio
SPA	Single particle analysis
SVA	subvolume averaging
TEM	transmission electron microscopy
TFS	Thermo Fisher Scientific
VACV	vaccinia virus
VMAP	viral membrane assembly protein
wbp	weighted back projection
WHO	World Health Organization
WT	wild type
YFP	yellow fluorescent protein

Abstract

Poxviruses are large, enveloped cytoplasmic dsDNA viruses with epidemic potential. Among them, **vaccinia virus (VACV)**, historically used as a live vaccine to eradicate smallpox, serves as a well-established model for studying poxvirus biology. Unlike conventional viral membrane acquisition via budding or wrapping, **poxvirus morphogenesis** follows a unique mechanism: cellular membranes are recruited to the cytoplasmic viral assembly site, disrupted, and extensively remodeled into precursors with stabilized **open ends**. Binding of these membrane precursors to a **viral scaffold protein** induces a distinct curvature, forming the characteristic **crescent-shaped** intermediates. As these crescents expand, they encapsulate viral DNA and proteins, forming spherical, immature virions. These immature particles undergo dramatic structural remodeling during **maturation**, culminating in the formation of infectious virions with a complex internal core.

Despite extensive studies, the molecular mechanisms underlying poxvirus assembly and maturation remain largely unknown. Here, I employed **cellular electron cryo-tomography (cryoET)** to investigate the **stepwise VACV assembly in infected cells**. Using **correlative imaging** and **focused ion beam (FIB)-milling** of plunge-frozen VACV-infected cells, I analyzed viral assembly sites by cryoET and captured individual viral particles ***in situ*** across all stages of morphogenesis.

This approach enabled direct visualization of viral genome incorporation, a process that remains poorly understood. Additionally, I identified possible maturation intermediates, offering new insights into **viral core formation**. Focusing on the viral membrane, **segmentation analysis** revealed distinct features such as the size, shape, curvature, and continuity of membrane precursors and growing crescents. Finally, **subvolume averaging** provided novel insights into the structural organization and **lattice arrangement** of the viral scaffold protein responsible for inducing membrane curvature in crescents and immature virions.

Zusammenfassung

Pockenviren sind große, behüllte zytoplasmatische dsDNA-Viren mit epidemischem Potenzial. **Vaccinia-Virus (VACV)**, einst als Lebendimpfstoff zur Ausrottung der Pocken eingesetzt, dient nun als etabliertes Modell zur Untersuchung der Pockenvirus-Biologie. Im Gegensatz zur klassischen Membranbildung durch Knospung oder Umhüllung erfolgt die **Morphogenese** dieser Viren über einen einzigartigen Mechanismus. Die Assemblierung von VACV findet in bestimmten, durch das Virus umorganisierten Bereichen des Zytoplasmas statt. Zelluläre Membranen werden dorthin rekrutiert, geöffnet und zu viralen Vorläufern mit stabilisierten, **offenen Membranenden** umstrukturiert. Bindung an das **virale Gerüstprotein D13** induziert eine spezifische Membrankrümmung, wodurch die charakteristischen **halbmondförmigen Membranstrukturen** entstehen. Diese „Halbmonde" wachsen weiter, um sich zu sphärischen, unreifen Viruspartikeln zu schließen. Dabei nehmen sie virale DNA und Proteine in sich auf. Während der anschließenden Reifung erfahren diese Partikel tiefgreifende strukturelle Veränderungen, darunter die Bildung einer komplexen internen Kernstruktur. Trotz intensiver Forschung sind die molekularen Mechanismen dieser Prozesse noch weitgehend ungeklärt.

Um die schrittweise **Assemblierung von VACV in infizierten Zellen** zu untersuchen, setzte ich **zelluläre Elektronen-kryo-Tomographie (cryoET)** ein. Mithilfe **korrelativer Bildgebung** und **FIB-Fräsung (Focused Ion Beam)** von tiefgefrorenen VACV-infizierten Zellen gelang es mir, virale Assemblierungsregionen gezielt zu analysieren und individuelle Viruspartikel ***in situ*** in verschiedenen Entwicklungsstadien abzubilden.

Dabei konnte ich virale Partikel während der **Genominkorporierung** beobachten – ein Prozess, der bislang wenig verstanden ist. Zudem identifizierte ich potenzielle **Reifungsintermediate**, die neue Einblicke in die Ausbildung der viralen Kernstruktur liefern. Virale Halbmondmembranen und ihre Vorläufer wurden mithilfe von **Segmentierungen** anhand ihrer Morphologie, lokalen Eigenschaften und Kontinuität untereinander charakterisiert. Durch die Prozessierung von Subvolumina, welche das virale Protein D13 enthalten, konnte ich eine **gemittelte Struktur** der Anordnung dieses Proteins im nativen viralen Gerüst auflösen. Diese bietet wichtige neue Einblicke in die strukturelle Organisation und **Gitteranordnung**, welche für die Krümmung der Membran in „Halbmonden" und unreifen Virionen verantwortlich ist.

1. Introduction

1.1 Poxvirus History and Relevance

Poxviruses are large, enveloped viruses with a double-stranded DNA (dsDNA) genome that infect a wide range of vertebrate and invertebrate host species. Within the *Poxviridae* family, the genus *Orthopoxvirus* encompasses viruses that are highly pathogenic to mammalian hosts, including humans (Olson & Shchelkunov, 2017). Most prominent among these is variola virus, the causative agent of the deadly smallpox disease with fatality rates of up to 40 % in unvaccinated individuals. It had been plaguing human populations for centuries until its worldwide eradication through vaccination in 1980 (Fenner et al., 1988). This huge civilizational success is currently the only example of a human infectious disease ever to be completely eradicated on a global scale (Caplan & Mamo, 2024). It can be partially accredited to the fact that variola virus exhibits a very narrow host range specific to humans and therefore does not have an animal reservoir. Chiefly, however, the eradication of smallpox was made possible through a globally coordinated regulatory and logistical effort preceded by centuries of targeted technological development and innovation, all motivated by the need to defeat so severe a disease. Indeed, the very concept of vaccination was discovered and developed specifically to provide protection against smallpox – as it is illustrated by the term 'vaccination' itself referring to the *Orthopoxvirus* vaccinia virus (VACV) that was used to immunize humans against variola virus.

A key technique that paved the way for the development of vaccination several hundred years later is variolation. This method confers immunity against smallpox by inoculating people with variola virus-containing material derived from patients with comparatively mild cases of the disease. Different methods of variolation are first documented to have been practiced in China and India in the middle of the 16th century (Boylston, 2012). The origins of variolation remain unclear and could be much older with some sources indicating that it might have been developed in China as early as 1000 AD. By the 17th century it was widely established in the Ottoman Empire and parts of North Africa and Europe. In 1796, observing dairy workers being protected against smallpox through previous infections with cowpox lead Edward Jenner to the invention of vaccination (Damaso, 2018). This discovery exploited the cross-reactivity of an elicited immune response against closely related viruses, based on empirical findings, before the emergence of the scientific fields of immunology and virology.

Though the terms "vaccinia virus" and concomitantly "vaccination" are derived from the cow, the VACV we know today is distinct from cowpox. It has no identified natural host species and possibly originated from recombination events between cowpox and now extinct horsepox

viruses, both used by the early vaccinators in the 19th century (Esparza et al., 2017). In the global smallpox eradication campaign of the World Health Organization (WHO) that commenced in 1966, several defined vaccine strains of VACV were used (Jacobs et al., 2009). VACV has since become a widely established laboratory model and is used as a tool for fundamental cell biology as well as vaccine development (Volz & Sutter, 2017). It is also often referred to as the "prototypical poxvirus" and serves as a tractable model system in the study of fundamental aspects of poxvirus biology (El-Jesr et al., 2020; Meng et al., 2012). Furthering our understanding of poxviruses, particularly the genus *Orthopoxvirus*, remains highly relevant for global health today.

Though variola virus, the historically most concerning member of the *Poxviridae* has been successfully eradicated, laboratory stocks still exist in the USA and Russia[1]. More immediately, several zoonotic poxviruses also pose a threat to humans, including orthopoxviruses like cowpox, camelpox and monkeypox (MPXV) and other viruses from the *Chordopoxvirinae* subfamily (Yang et al., 2021). Mpox, the disease caused by MPXV, has recently been declared a public health emergency of international concern by the WHO (Brüssow, 2025). Currently, MPXV clade IIb (since 2022) and clade Ib (since 2024) are circulating via human-to-human transmission beyond west and central Africa, the respective sites of zoonotic spillover into the human population[2]. Surging mpox outbreaks coincide with a lack of anti-poxviral immunity in the younger generations who have not been vaccinated during the WHO smallpox eradication campaign. Also, very few drugs against poxviruses are currently available and have proven ineffective against MPXV in recent outbreaks (PALM007 Writing Group et al., 2025). There is therefore a clear need for the development of novel strategies that specifically act against conserved poxviral targets. A prerequisite for this is the thorough understanding of critical steps in the poxvirus infection cycle on the molecular level.

[1] WHO Advisory Committee on variola Virus Research: report of the twenty-fifth meeting, Geneva, Switzerland, 25-26 October 2023. Geneva: World Health Organization; 2024

[2] Mpox global strategic preparedness and response plan: World Health Organization; 2025

1.2 Poxvirus Cellular Biology and Infection Cycle

As nucleocytoplasmic large DNA viruses (NCLDVs), poxviruses do not exploit the nuclear DNA replication and transcription machinery of the host cell. Instead, they complete their viral cycle in the host cytoplasm. The NCLDVs, which also include the giant viruses of amoebae, have recently been classified into the new phylum *Nucleocytoviricota* (Aylward et al., 2021; Koonin et al., 2020). The viral families within this phylum share a conserved DNA replication and translation machinery, a DNA-packaging ATPase and – except for pandoraviruses – a major capsid protein (Rodrigues et al., 2021). All these viruses, including the *Poxviridae*, are highly complex and fundamental aspects of their biology remain poorly understood. The genome of the comparatively well-studied VACV encodes more than 200 open reading frames, over 10 % of which have currently unknown functions (Deng et al., 2025). Poxvirus gene expression is temporally regulated, allowing the classification into early, intermediate and late genes. The infection cycle of VACV, which serves as a model for *Orthopoxvirus* biology, is described in the following paragraphs and schematically illustrated in **figure 1**.

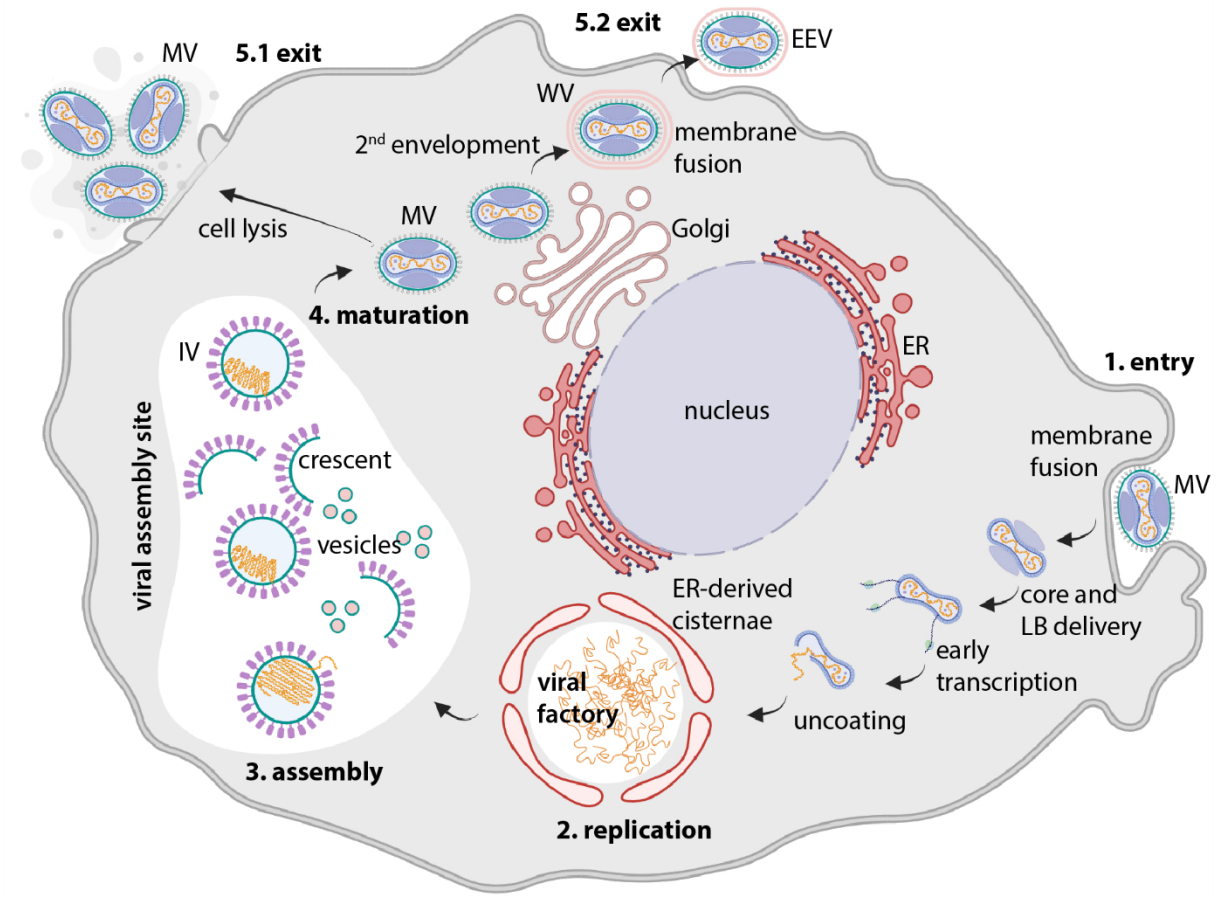

Figure 1: Overview of the viral cycle of VACV in infected cells. Mature virions (MV) enter the cell via fusion of the viral membrane (green) with the host cell membrane to deliver its lateral bodies (LB, purple) and viral core (blue) into the cytoplasm. LB dissolve quickly. The core contains the viral DNA genome (orange). Early genes are transcribed within the core and viral mRNA (black) leaves the core. After opening of the core and delivery of the genome, viral DNA is replicated in the virus-induced viral factory surrounded by host ER-derived membranes. Later, the viral factory becomes the site of progeny virion assembly. There, spherical immature virions (IV) are formed from viral crescent membranes. These are generated from ER-derived membranes that are scaffolded by the viral protein D13 (pink). IV mature to form the brick-shaped MV. MV can exit the host cell upon cell lysis. A subset of MV undergoes secondary envelopment at the Golgi, resulting in intracellular wrapped virions (WV). These exit the cell via fusion at the plasma membrane, resulting in double-enveloped particles termed extracellular enveloped virions (EEV). This figure was created using biorender.

1.2.1 Mature virion structure and host cell entry

The infectious, brick-shaped mature virion (MV) is surrounded by a single membrane envelope and has dimensions of 360 x 250 x 270 nm (Cyrklaff et al., 2005). Within the MV, the dsDNA genome is encased in a proteinaceous viral core that typically has a biconcave, dumbbell-like shape and is flanked by two lateral bodies (Greseth & Traktman, 2022). The proteinaceous structure of the VACV core has recently been demonstrated by cryoET, rejecting earlier hypotheses of an internal membrane delineating the core (Datler et al., 2024; J. Liu et al., 2024). The smooth inner core wall is likely formed by the viral protein A3 and is decorated with a spikey palisade layer. This palisade is formed by homotrimers of the viral protein A10, arranged in a

loosely hexagonal order. Within the palisade layer, a flower-shaped structure is observed, apparently forming a pore in the core wall. Further proteins enriched in the core and likely to have a structural role are A4 and L4.

MVs enter the host cell via membrane fusion, either directly at the plasma membrane or after uptake through macropinocytosis (Moss, 2016). Thereby, the lateral bodies and the viral core are delivered into the host cell cytoplasm. The lateral bodies dissolve quickly, thus liberating viral proteins that modulate the host cell and antagonize the innate immune response, specifically cellular DNA-sensors and interferon γ signaling (Bidgood & Mercer, 2015; El-Jesr et al., 2020). Major components of the lateral bodies are the phosphoprotein F17, the viral oxidoreductase G4 and the phosphatase H1. The delivered core, in turn, stays intact throughout the transcription of early viral genes within the core upon core activation (Greseth & Traktman, 2022). Transcription is mediated by the viral RNA polymerase holoenzyme which is packaged into the viral core during particle assembly along with early transcription factors and an RNA-capping enzyme. Early transcription requires the entry of nucleoside-triphosphates into the core and the exit of the capped viral mRNA, possibly through the observed putative pore structures (Datler et al., 2024; Hernandez-Gonzalez et al., 2023). Early transcripts are then translated by host cell ribosomes. Early gene products are required for the delivery of the viral genome by opening the core and for subsequent DNA replication and intermediate gene expression.

1.2.2 Viral DNA replication

The viral DNA is replicated by the virally encoded DNA-dependent DNA polymerase in dedicated, virus-induced compartments within the cytoplasm. These sites of viral DNA replication are termed viral factory. They are surrounded by membrane cisternae from the host cell endoplasmic reticulum (ER) and have been described as “mini-nuclei” (Tolonen et al., 2001). A recent study on the viral factories of mimivirus suggests that poxvirus factories, too, could exhibit the properties of a liquid-liquid phase separated organelle (Rigou et al., 2024). The fundamental principle of separating viral replication from the host cytoplasm is a common theme among cytoplasmically replicating viruses, which includes the NCLDVs and most RNA-viruses (Glingston et al., 2019). Many RNA-viruses protect their genome in membranous compartments like the double-membrane vesicles induced by coronaviruses (Roingeard et al., 2022). Phase separation resulting in a membrane-less compartment is an alternative strategy that is employed by non-segmented negative strand RNA viruses, including Ebola virus and rabies virus (Vallbracht et al., 2025).

Poxvirus DNA replication is mediated by virally encoded enzymes and cofactors and independent from the host nucleus. However, a recent study suggests that some nuclear factors are recruited to the viral factory in poxvirus infection to support viral replication (Veratti et al., 2024). Intermediate and late gene expression is mediated by the viral transcription machinery based on the replicated viral genomes. VACV induces an extensive host-cell shutoff to favor viral gene expression and protein translation (Dhungel et al., 2020).

1.2.3 Assembly of the immature virion

Late in infection, after DNA replication and viral protein translation, the viral factory becomes the site of progeny virion assembly. Replicated viral DNA and translated structural proteins are packaged in a membrane envelope derived from the host cell (Moss, 2015). The membrane acquisition of poxviruses is different from known cellular membrane remodeling pathways which are commonly exploited by most enveloped viruses. Such canonical mechanisms include the ESCRT-dependent budding at the plasma membrane employed by retro-, paramyxo- and filoviruses (Rheinemann et al., 2021) as well as budding or wrapping at cellular compartments of the secretory pathway (Hassan et al., 2021). Instead, members of the *Nucleocytoviricota* utilize membrane rupture to generate open-ended membrane sheets that are then re-shaped and sealed around viral contents to form the viral envelope (Rodrigues et al., 2021). This mechanism is generally poorly understood but best studied in VACV. Viral open-ended membrane structures were first described in VACV-infected cells in 1968 (Dales & Mosbach, 1968). These membrane assembly intermediates are termed crescents due to their characteristic, open half-moon shape in 2D electron microscopic images. Historically, a mechanism of complete *de novo* membrane biogenesis had been proposed to explain these observations of open-ended single lipid bilayer structures within the cytoplasm. Others rejected the concept of open-ended membranes within the cell and proposed an alternative explanation. It was argued that the appearance of viral crescents as single lipid bilayers might be an artefact of sample preparation causing the two apposing membranes of a cisterna with a minimal lumen to collapse into each other. By now, the open-ended nature of VACV crescent membranes has been clearly demonstrated using various complementary electron microscopical techniques and the following model of the VACV assembly mechanism is widely accepted (Moss, 2018).

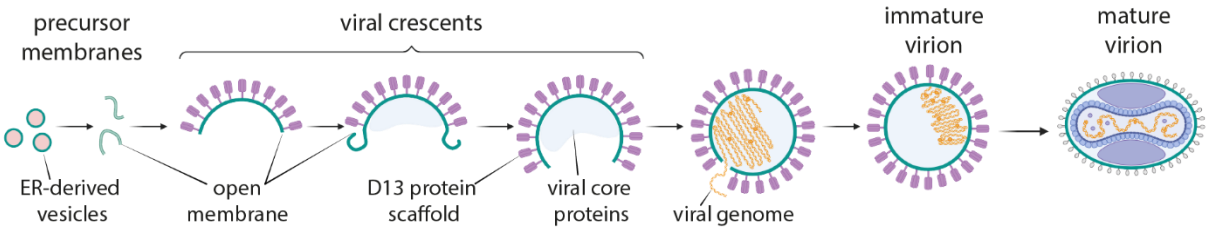

Figure 2: Schematic representation of the current model for VACV assembly. This figure was created with biorender.

Cellular membranes are recruited to the viral assembly site and ruptured by viral effector proteins (**figure 2**). The precise mechanism of membrane rupture and stabilization of the resulting membrane sheets' open edges is unclear, but a set of five essential viral proteins has been identified by mutagenesis (Moss, 2015). These proteins are termed viral membrane assembly proteins (VMAPs). Two of these, namely L2 and A30.5, are small transmembrane proteins that are embedded in the ER membrane. The other VMAPs (H7, A11 and A6) are soluble proteins. However, they have been shown to co-localize with ER- and viral membranes and contain different membrane- or lipid binding motifs (Pathak et al., 2018). There seems to be a close interplay between them as the deletion of any one VMAP leads to an abrogation of viral crescent formation even in the presence of the other four (Weisberg et al., 2017). These VMAP deletion mutants appear to specifically affect the rupture and stabilization of the open membrane. They exhibit the same phenotype with IV-like particles budding into the ER lumen while the viral membrane is continuous with the otherwise apparently intact ER membrane. Thus, the VMAP deletion phenotypes support the hypothesis that the viral membrane is derived from the host ER (Moss, 2015, 2018).

The viral membrane adopts the typical crescent shape through the association with a viral scaffold protein that imposes the specific spherical curvature. This scaffold protein D13 is highly conserved among poxviruses and corresponds to the generally conserved major capsid protein of the phylum *Nucleocytoviricota* (Rodrigues et al., 2021). D13 binds to the viral protein A17 which is embedded within the viral membrane. The antibiotic rifampicin blocks the assembly of crescents and immature virions by inhibiting the D13-A17 interaction, resulting in the accumulation of D13 in dense "rifampicin-bodies" (Garriga et al., 2018). On the surface of the viral membrane, D13 self-assembles to form a continuous, spherical honeycomb-like lattice. The fixed curvature of the viral crescent and IV membrane is defined by the self-assembly of the scaffold. However, this mechanism of spherical D13 self-assembly is not clear and currently an active area of research. Employing deep-etch electron microscopy, the D13 lattice has been described as mostly hexagonal but containing pentagonal and heptagonal lattice facets as well (Heuser, 2005). Following Caspar-Klug theory, these deviations from hexagonal symmetry are

required to enable a spherical lattice (Indelicato et al., 2020). The protein D13 and its self-assembly mechanism have also been studied *in vitro*, yielding several atomic structures of the D13 homotrimer solved by X-ray crystallography and more recently single particle cryoEM (Bahar et al., 2011; J.-K. Hyun et al., 2011; J. Hyun et al., 2022). These revealed the double jelly-roll fold of the protein and its homology to the viral capsid proteins of adenoviruses. Depending on the protein construct used and experimental conditions *in vitro*, D13 is capable of self-assembly into several different higher-order structures with the homotrimers as building blocks, i.e. subunits. These range from flat honeycomb lattices formed by interlacing hexamers of D13 trimers on functionalized lipid bilayers to spherical and tubular assemblies. In these experiments, a displacement of the N-terminal helix through the addition of an N-terminal poly-histidine tag or N-terminal truncation of the protein appears to be essential for D13 self-assembly.

Viral crescents appear to grow by incorporating new membrane material at their open edges that are derived from a pool of precursor membranes in the assembly site (Chlanda et al., 2009). How these fusion events are regulated remains poorly understood. Eventually, a complete spherical shape is achieved through the continuous incorporation of new membrane material and scaffolding of these membrane areas by an extension of the D13 scaffold. The membrane is then sealed by an unknown mechanism, resulting in the spherical, immature virion (IV).

The components of the viral core associate with these crescent membranes and thus get enclosed in the growing, spherical immature virion. Although the precise mechanism of this selective packing of core and lateral body proteins is not known, a complex of seven viral proteins situated on the inside of the viral membrane is essential (L. Liu et al., 2014). Mutants of this seven-protein complex result in the formation of defective, empty IVs devoid of core proteins and DNA. The mechanism of viral genome incorporation is not fully understood, either. Three viral proteins are required for the packing of the genome into nascent IV particles, among them the putative DNA-packaging ATPase A32 which is conserved in *Nucleocytoviricota* (Greseth & Traktman, 2022; Talbert et al., 2023). Further, the viral membrane protein A13 and the protein I6, which binds to the telomeric hairpins at the end of the viral genome, are required. Deleting any of these proteins results in aberrant, DNA-deficient IV. A model has been proposed for VACV genome uptake through a portal formed by the viral ATPase that is anchored to the viral membrane via A13 and translocates the viral DNA into the immature virion (Greseth & Traktman, 2022). Specificity for the genome was suggested to be conferred via protein-protein interaction between the ATPase A32 and I6, bound to the viral DNA telomeric hairpins. However, it is unclear if A32 really forms a portal in the membrane of the immature viral particle and how this relates to the closure and sealing of the viral membrane. Further, it is not known how the viral genome is structured and condensed

inside the virion. In electron microscopic data, the genome is often observed as a dense nucleoid inside the immature viral particle, sometimes apparently entering the particle through a large opening in the viral membrane (Chlanda et al., 2009; Condit et al., 2006).

1.2.4 Maturation of the viral particle

After the immature virion is complete with internal structural proteins, the transcription machinery and the viral DNA genome, a complex multi-step maturation process is required to form infectious, mature virions. This process is highly regulated by protein modifications like phosphorylation, disulfide bond formation and proteolytic processing. This includes the proteolytic processing of structural components of the core like the A3 protein. Identified key regulators are the viral protein kinase F10, the viral proteases I7 and G1 and the proteins of the virally encoded redox system (L. Liu et al., 2014). Further, there are indications for the involvement of host factors such as phosphatidylinositol 3-kinases. The morphology of the viral particles changes dramatically during maturation: The spherical shape of the IV changes to the more elongated, brick-like shape of the mature viral particle. This is concomitant with the removal of the D13 scaffold. This specific scaffold disassembly step is known to be regulated by the viral protease I7 cleaving the viral transmembrane protein A17, which connects the D13 scaffold to the viral membrane. The maturation process is accompanied by a reduction in the overall volume enclosed by the viral particle and a corrugation of the MV envelope (Hernandez-Gonzalez et al., 2023). Internally, two lateral bodies and the complex core structure encasing the genome are formed. The mechanism of this core formation is not understood, as intermediates of core formation have been elusive. The prevailing view is that maturation from IV to MV occurs in the viral assembly site and that MVs subsequently leave the assembly site (L. Liu et al., 2014). Indeed, active microtubule-dependent intracellular transport of MV has been demonstrated (Ward, 2005). However, in electron microscopic images of infected cells, MVs and IVs appear to form distinct, separated clusters (Moss, 2015).

1.2.5 Cell exit and dissemination of progeny virions

Intracellular mature virions with a complete internal structure and a single membrane envelope are infectious and are released from the host cell through cell lysis. A subset of the intracellular MVs, however, leaves the cell on an alternative route and ultimately forms a second type of infectious particles (Bidgood & Mercer, 2015; Monticelli et al., 2020). These particles first undergo secondary envelopment at the Golgi compartment. In a process that resembles the formation of double-membrane vesicles in other viral infections or the mechanism of lysosome formation from phagophores, the virion is wrapped in a Golgi membrane cisterna, resulting in two additional membranes surrounding the MV (Sivan et al., 2016). These intracellular viral particles with three

concentric membrane envelopes are referred to as wrapped virions (WV). WVs then leave the host cell independently of lysis by fusion of their outermost envelope with the plasma membrane. The result are extracellular virions with two concentric membranes that are termed extracellular enveloped virions (EEV). While this mechanism of secondary envelopment and non-lytic particle release is not strictly required to produce infectious progeny virions, EEVs are thought to be essential for the dissemination of infectious virions within the host organism. Interestingly, the approved smallpox drug Tecovirimat targets secondary envelopment, but has proven ineffective against clade I MPXV in recent outbreaks (Chenchula et al., 2025). A subset of the EEVs, in turn, are not freely disseminated but stay attached to the host cell as cell-associated extracellular enveloped virions. They are believed to move via a viral surfing mechanism that includes the polymerization of intracellular actin tails propelling the attached virions on cellular protrusions (Bidgood & Mercer, 2015).

During infection of a new host cell, the outermost envelope of EEVs is disrupted by endosomal acidification after macropinocytotic uptake (Schmidt et al., 2011). This exposes the underlying MV membrane to initiate fusion with the endosomal membrane and delivery of the viral content into the cytoplasm

1.3 Electron cryo-Tomography

1.3.1 Electron (cryo-)microscopy

Electron microscopy (EM) has been a powerful tool in the study of virus samples since the beginning of modern virology (van Helvoort & Sankaran, 2019). In turn, isolated viral particles were among the first samples ever to be imaged with electron microscopes. The two fundamental modes of electron microscopy are scanning electron microscopy (SEM) and transmission electron microscopy (TEM) (Egerton, 2016). In SEM, back-scattered electrons are detected, and the image is a representation of a biological sample's surface. In TEM, electrons are detected after passing through the sample, forming a projection image through the sample volume. This text mainly discusses TEM approaches. Since electrons can be accelerated to much shorter wavelengths than photons of visible light, electron microscopy can resolve features several orders of magnitude smaller than light microscopy. However, imaging with a condensed electron beam requires a vacuum in the electron microscope. Therefore, samples for EM need to be fixed, either by dehydration, embedding in resin or cryo-fixation.

For conventional TEM of isolated samples such as viral particles, these are dried on EM support grids and stained with electron-dense heavy metals, thereby generating contrast. Thus, this method does not image biological densities directly, but the heavy metals of the stain. Cellular

samples for conventional TEM are chemically fixed and then dehydrated, stained with heavy metals and embedded in resin (Ayache et al., 2010). An alternative is high-pressure freezing and subsequent resin-embedding by freeze-substitution. Thin, electron-transparent cellular sections for TEM imaging can then be produced from resin-embedded blocks with an ultramicrotome. All these sample preparation methods generate durable samples for high-contrast TEM imaging, at the cost of protein aggregation and lipid extraction artefacts. In 1981, Alastair McDowell and Jaques Dubochet discovered that vitreous ice can be formed by plunge-freezing in a cryogen with sufficiently high cooling rates (Dubochet, 2012). This enabled electron cryo-microscopy (cryoEM) - the direct observation of biological specimens that are natively conserved in a frozen-hydrated state, eliminating fixation, dehydration and staining artefacts. Originally, this technique was applied to purified samples in solution like isolated viruses and large protein complexes (Adrian et al., 1984).

While the direct observation of native-like biological material in cryoEM has great advantages, TEM imaging of such samples generates insufficient electron scattering contrast due to the absence of heavy atoms. CryoEM image formation therefore relies on phase contrast that is introduced by acquiring images out of focus (Franken et al., 2020). The phase shift results in a defocus-dependent, oscillating contrast contribution across spatial frequencies. It is described by the contrast transfer function (CTF) which depends on the effective defocus value and the fixed spherical aberration and acceleration voltage of the electron microscope. Higher defocus values result in better contrast but also in attenuation of high-resolution signal and a blurring of the image. The second fundamental challenge of biological cryoEM is the destruction of the sample during imaging. As the electron beam interacts with the biological material, thermal energy is deposited, causing beam-induced sample damage. Thus, information is progressively lost during imaging, beginning with high-resolution features. This strictly limits the electron dose that can be used in cryoEM. Due to the limited dose, cryoEM images have an intrinsically low signal-to-noise ratio (SNR). With the advent of direct electron detectors, the obtainable image quality and thus the resolution power improved significantly. The SNR can be improved through the acquisition of dose-fractionated movie frames and subsequent frame alignment, compensating for beam-induced motion of the sample during imaging. Further, an energy filter before the detector and an objective aperture in the back focal plane of the electron microscope column improve the SNR and contrast by excluding inelastically scattered electrons from contributing to the image.

1.3.2 Single particle analysis

Aligning and averaging the 2D projections of identical particles dramatically increases the SNR and thus elevates the high-resolution features present in the image above the background noise level. Provided a high enough number of particles in a range of poses, presenting the same object from all sides, an average 3D reconstruction can be obtained from the 2D projections. This single particle analysis (SPA) approach to cryoEM was first applied to large, symmetrical assemblies like icosahedral viral capsids (Prasad et al., 1988; Ruma et al., 2025). The field has been advancing rapidly ever since (Patwardhan et al., 2025). It is now a well-established technique, routinely yielding high-resolution structures of purified macromolecules, continuously pushing the size and resolution limits (M. Wu & Lander, 2020). Combined with 3D classification analysis, even structural heterogeneity and flexibility can be resolved (Kinman et al., 2023).

1.3.3. Tomography

In the case of unique or pleiomorphic, irregular structures like poxviruses, SPA is not applicable, and 3D reconstructions must be obtained from a single biological object. This can be achieved through tomography. By acquiring a series of 2D images under a range of sample tilt angles and aligning these tilted projections, the 3D volume can be backprojected. However, as the effective thickness of the sample in tilted TEM acquisition rises with increasing tilt angle, the angular range that can be sampled is usually limited to about ± 60 ° (Hagen et al., 2017). The inaccessible tilt angles result in a wedge of missing information in Fourier space. In real space, this missing wedge artefact causes anisotropic resolution of the reconstructed tomographic volume. This particularly affects the resolution along the tomogram z axis, i.e. the axis that is parallel to the incident electron beam on the un-tilted sample. Electron cryo-tomography (cryoET) of frozen-hydrated biological samples is further limited by radiation damage, as the available electron dose must be distributed on the entire tilt series, further reducing the dose per image.

The advantage of cryoET is that it allows direct 3D imaging of pleiomorphic biological samples, preserved in a close-to-native state (Baker et al., 2017). Early cryoET studies of purified viral samples provided unprecedented insights into the structure of the enveloped herpes simplex virus (HSV) particle and, later, vaccinia virus MV (Cyrklaff et al., 2005; Grünewald et al., 2003). As is the case for cryoEM in general, cryoET has profited greatly from technological advancements in hardware and processing power in recent years and continues to be a rapidly evolving field. Tomographic approaches are also applied in medical imaging and electron tomography of conventionally prepared, resin-embedded biological TEM samples. They are particularly powerful in complex environments like the inside of cells, where various biological structures would appear superimposed in simple 2D projection images.

1.3.4 Cellular electron cryo-tomography

CryoET applied to cellular samples can directly visualize biological structures in their native environment and provides detailed 3D insights into biological processes like virus-host interactions. Adherent cells can be grown on pre-treated EM support grids and vitrified by plunge-freezing. However, only the peripheral regions of some cell types are thin enough to be directly imaged by TEM. To access the interior of the cell body, samples must be physically thinned (E. R. J. Quemin et al., 2020). This was first achieved through electron cryo-microscopy of vitreous sections (CEMOVIS). For this, thin sections of high-pressure frozen cells are prepared with a cryo-ultramicrotome and transferred to EM grids for TEM and cryoET. This enabled the study of HSV in the nucleus and the cytoplasmic assembly of VACV. However, sectioning itself is challenging and prone to introduce severe compression artefacts into the sample (Dubochet, 2012; Pierson et al., 2011).

A breakthrough in the field of cellular cryoET was the production of thin, cellular samples through cryo-focused ion beam (FIB)-milling (Rigort et al., 2012). Vitrified cells on EM support grids are loaded onto a cryo-stage in a dual-beam FIB-SEM microscope and first coated with a protective layer of platinum. Then, a focused beam of gallium ions is used to ablate cellular material in defined areas until only a thin, electron-transparent section, termed lamella, remains. Such cryo-lamellae are then used for cryoET data acquisition in a cryoTEM microscope and provide access to the cellular interior. Typically, lamellae are prepared with a thickness between 100 and 300 nm. Thinner lamellae result in better contrast because their TEM projections are less noisy, but they contain a smaller sample volume and less contextual information. Recent investigations have demonstrated that the milling process introduces a damage layer of ~ 30 nm from the exposed milling surface, limiting the usefulness of very thin lamellae (Lucas & Grigorieff, 2023; Tuijtel et al., 2024). It should be noted that this damage layer affects only higher-resolution features of particles as assessed by subvolume averaging or template-matching approaches. The cryoFIB-milling workflow is now widely established in the field of cellular cryoET and its specific application to adherent cells that are vitrified through plunge-freezing is depicted in **figure 3**.

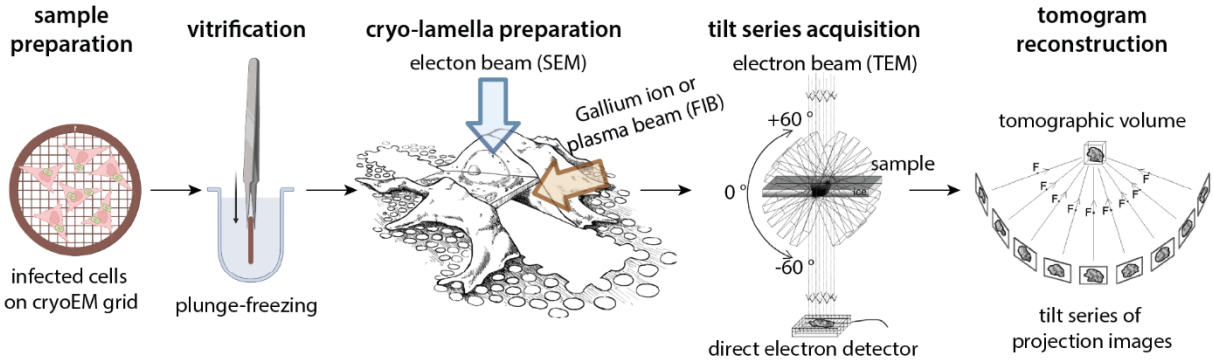

Figure 3: Illustration of the cellular cryoET workflow employed here for adherent cells grown on cryoEM support grids and vitrified by plunge-freezing in a liquid ethane-propane mixture. The middle panel, illustrating the production of a thin lamella from a cell on the grid using cryoFIB-SEM is reproduced from Villa et al., 2013 with permission from Elsevier and minor modifications. The last two panels, representing the collection of tilt series on the lamella sample in cryoTEM and subsequent tomographic reconstruction are reproduced and modified from Grünewald et al., 2002 with permission from Elsevier.

Recent developments in sample preparation workflows for cellular cryoET include the introduction of plasma FIB-milling (Berger et al., 2023). Xenon and argon plasma achieve faster milling rates than gallium ion beams, with a similar milling damage layer. This enhances high throughput milling in automation as well as the milling of thicker “waffle” samples. The waffle method is a recent innovation in the preparation of vitreous samples using high-pressure freezing of biological material directly on EM grids (Kelley et al., 2022). This enables lamella preparation and cellular cryoET on samples that are not amenable to the conventional cryoFIB-milling workflow (**figure 3**) due to size, concentration or preferential orientation. Vitrification by high pressure freezing like in the waffle method is particularly advantageous for thick samples above 10 µm that cannot be properly vitrified by plunge-freezing due to the inherent depth-dependent cooling rates. With improved high pressure-freezing methods and related innovations in FIB-milling approaches like waffle milling or cryo-lift-out, much larger samples such as organoids, tissue biopsies and even whole, small model organisms become accessible to *in situ* 3D imaging by cryoET (Creekmore et al., 2024; Klumpe et al., 2025; Nguyen et al., 2024).

Fluorescence-guided positioning of lamella production sites is possible with cryo-fluorescence microscopes (cryoFM) and correlative light and electron microscopy (CLEM) approaches (E. R. J. Quemin et al., 2020). This is indispensable for the targeting of specific, rare events in a sample for cellular cryoET. CryoCLEM has become more powerful through the recent development of in-line fluorescence microscopes integrated into cryoFIB-SEM systems (Boltje et al., 2022; Li et al., 2023). Beyond choosing target sites for lamella production, cryoCLEM can provide valuable contextual fluorescence-based information, guiding cryoET data acquisition and complementing the structures observed in cryoTEM (Moser et al., 2019). This is applicable to milled lamellae through on-lamella correlation as well as to naturally thin, peripheral regions of adherent cells

(Klein et al., 2021). Ongoing improvements of cryoFM such as cryo-confocal fluorescence imaging, cryo-immersion objectives and cryo-superresolution techniques are improving the precision in such cryoCLEM workflows (Faul et al., 2025; Sexton et al., 2022).

1.3.5 Data processing and analysis

With cryoET, biological specimens, including the interior of cells, can be accessed while preserved in a close-to-native state, allowing direct imaging at the nm scale. Yet, cryoET image data can contain high-resolution details beyond this range. These are, however, obscured by noise due to the low dose available during imaging, and corrupted by the missing wedge. However, with a suitable subvolume averaging (SVA) strategy, both these limitations can be overcome if a structure is repeatedly found in the sample, covering a sufficient range of poses. Ideal targets for in-cell SVA are highly abundant structures like ribosomes or regular higher-order structures such as cytoskeletal elements, viral capsids or lattice-forming proteins. Analogous to single particle analysis of 2D cryoEM images, the high-resolution details present in tomographic data can be brought out from the noise by extraction of repetitive subvolumes, alignment to a common reference and averaging (Pyle & Zanetti, 2021). The missing wedge of information in Fourier space is recovered in the average subvolume, if particles have different orientations within the whole tomogram. CryoEM images are modulated by the contrast transfer function (CTF) during defocused data acquisition and must be CTF-corrected during tomogram reconstruction as a preprocessing step for SVA. The CTF oscillates and is zero for some spatial frequencies where no information can be recovered. Other spatial frequencies contribute negative contrast, and their phases must be flipped during CTF-correction. As the CTF depends on the defocus value, a correct estimate of the defocus of the sample is required for accurate phase-flipping. This is obtained by fitting a modelled CTF curve to the Fourier transform of the image. The effective defocus changes while tilting the sample and therefore must be estimated on a per-tilt-image basis. Also, the defocus is not equal throughout the sample volume, but in fact a gradient. For optimal recovery of spatial information required for SVA, the CTF is therefore estimated and corrected in small volume slabs to achieve 3D-CTF-correction (Turoňová et al., 2017). To achieve optimal conditions for SVA, errors in the tomogram reconstruction must be minimized. For this, a correct alignment of the tilt series is essential. The best alignment is currently achieved by tracking gold fiducials of a defined diameter which can be added to *in vitro* samples. On cellular lamella samples, this is not possible, and alignment must be performed manually on serendipitous fiducials or with cross correlation-based tracking of patches, which is less accurate (Pyle & Zanetti, 2021).

There is no unified data processing pipeline for SVA but a range of different software packages, often with limited transferability and standardization between them. A suitable strategy specific to each project must be chosen and often customized, especially regarding particle picking. CryoET and SVA of purified in vitro samples such as ribosomes or virus-like particles can provide high-resolution structures. High-end processing approaches to in-cell SVA can achieve comparably high resolution when applied to some very abundant and regular structures (Kudryashev, 2024). The main advantage of performing SVA on cellular cryoET data remains that it provides access to native biological structures and assemblies within the cellular context. Even at intermediate resolutions, average volumes thus obtained can be used to fit known structural models that were obtained by complementary, high-resolution techniques.

Most features within cellular tomograms, however, are pleiomorphic or unique and not amenable to SVA. To analyze them at the contextual level and bring out the full complexity of the cellular environment, tomographic volumes are binned and filtered to increase contrast at the expense of high resolution. A range of filtering techniques are applicable, including band-pass frequency filtering, anisotropic diffusion filters and CTF-deconvolution (Frangakis, 2021; Tegunov & Cramer, 2019). Filtered tomogram volumes are valuable for direct, morphological and contextual analysis of pleomorphic structures like membranes, filaments or virions. A powerful tool for this type of analysis are volume-based segmentations that assign tomogram voxels to different classes according to the biological structures they belong to. Segmentations enable 3D rendering of the annotated biological structures for visual analysis and provide annotated 3D data for downstream processing. Segmentation processes can be partially automated by machine learning to recognize general features such as cellular membranes, or custom-trained features (Heebner et al., 2022; Lamm et al., 2024). As volume-based segmentations are direct interpretations of tomographic data, they are affected by the anisotropic resolution caused by the missing wedge.

Recently, several deep learning-based approaches have been developed that aim to compensate for this missing wedge of information computationally (Y. Liu et al., 2022; Van Veen et al., 2024; Wiedemann & Heckel, 2024). However, such approaches can be prone to hallucination and with the real ground truth data in the missing wedge not being sampled, there is no straightforward way to validate a prediction against the ground truth in real-world scenarios (Antun et al., 2020; Bhadra et al., 2021; Turk & Baumeister, 2020; Wiedemann & Heckel, 2024).

State-of-the art cellular cryoET and data analysis by segmentation and SVA is a powerful tool to investigate viral processes *in situ*. For example, recent studies have shown the HIV capsid disrupting the nuclear pore during transit into the host cell nucleus (Kreysing et al., 2025) and the

assemblies of the nuclear egress complex on the inner nuclear membrane that allow herpesviruses to exit the nucleus (Pražák et al., 2024). In the cytoplasm, recent cryoET studies revealed the structure of the protein pore spanning the double membrane vesicles that are the replication organelles of SARS coronavirus 2 (Zimmermann et al., 2023) and the organization of the Ebola virus viral factory (Vallbracht et al., 2025).

2. Objectives

The aim of this thesis is to improve our understanding of the complex poxvirus assembly and maturation process. The mechanism of membrane assembly from open-ended precursors in particular calls for three-dimensional imaging approaches that are close to the native state.

Building on previous data on vaccinia virus (VACV)-infected cells from electron microscopy studies, state-of-the-art electron cryo-tomography (cryoET) was employed here to showcase viral assembly intermediates pristinely preserved directly inside the cellular context, at high resolution and in 3D. Focused ion beam milling provides the necessary access to the cellular interior and viral assembly sites. With such a dataset in combination with custom segmentation pipelines and tailored subvolume averaging approaches, I intended to both map the landscape of virion morphologies at different stages of assembly and to resolve the interplay between viral membranes and proteins at the level of individual macromolecular complexes. Specific questions to be addressed were the properties of the open-ended viral crescent membrane and its small vesicle precursors and the molecular architecture of the curvature-inducing D13 protein scaffold decorating these viral membranes. Given the variability of D13 *in vitro* assemblies reported in the literature, probing the arrangement of the curved lattice directly on the native viral membrane is key to understanding its formation and function during the assembly of progeny virions.

Beyond the assembly of the viral membrane, the processes of genome packaging into the viral particle and the dramatic changes in virion morphology during subsequent maturation steps remain poorly understood. Developing a strategy to target the sites of viral assembly and maturation within infected cells for cryoET opens the possibility to localize and analyze such elusive intermediates of virion morphogenesis. HeLa cells infected with vaccinia virus were chosen as a well-established and tractable model system. To facilitate the characterization of this experimental system by fluorescence microscopy and allow the targeting of viral assembly in frozen-hydrated cells using correlative light and electron microscopy approaches, a fluorescently labelled virus (A3-YFP) was used in parallel to wild type virus.

Recent dramatic improvements in the automation of cryoET sample preparation and data acquisition require novel tools to fully exploit this new abundance of data. Accordingly, I worked towards the development of new custom workflows to aid segmentation-based contextual and morphological analysis as well as subvolume averaging of the viral scaffold protein D13.

3. Results

3.1 Characterization of VACV-infected Cells

Poxviruses complete their infection cycle entirely within the host cell cytoplasm which is heavily reorganized during infection. This can be observed and characterized by fluorescence-based confocal microscopy. As a model system, I used HeLa cells and vaccinia virus (VACV) of the Western Reserve strain, both wild-type virus and an engineered strain which encodes for a fluorescent YFP label fused to the viral core protein A3 (kindly provided by Prof. Michael Way, described in Arakawa et al., 2007). These two strains are characterized and compared in **figure 4** and referred to throughout this thesis as wild-type (WT) virus and A3-YFP virus, respectively.

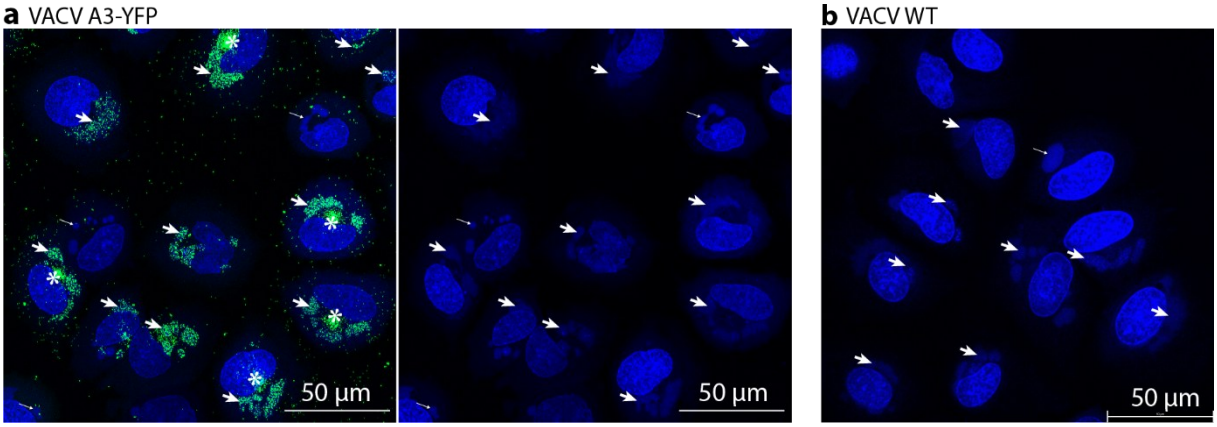

Figure 4: Fluorescence-based characterization of the model system: HeLa cells were infected with A3-YFP VACV (a) at an MOI of 20 or wild-type VACV (b) at an MOI of 10, fixed with PFA 8 hpi and imaged in a confocal point-scanning fluorescence microscope. The blue channel displays Hoechst signal staining cellular and viral DNA, the green channel displays the YFP signal from the labelled viral core protein A3. In a), viral assembly sites are indicated with thick arrows based on co-localization of green and blue signal. Viral replication sites (only blue, no green signal) are indicated with thin arrows. In b), the respective sites are annotated the same way but based on morphological comparison with the Hoechst channel in a) due to the lack of YFP-signal in the un-labelled wild-type virus. Asterisks in a) indicate clusters of virions observed as bright localized YFP signal in the perinuclear region.

Staining of VACV-infected cells with Hoechst dye labels not only the host cell DNA in the nucleus but also viral extranuclear DNA which becomes apparent starting 4 hpi. Such extranuclear DNA is absent in uninfected control samples. These sites of extranuclear DNA correspond to virus-induced compartments within the host cytoplasm where the viral genome is replicated and protected from the cellular antiviral immune sensors. At later timepoints in infection with A3-YFP virus (**figure 4a**), the extranuclear DNA signal co-localizes with fluorescence from the labelled viral core protein A3, signifying the change from a viral replication to a viral assembly compartment where the replicated DNA, the translated viral proteins, and a pool of cell-derived membranes come together to form progeny virions. As the synchronization of the infection in this

experiment is not perfect, single cells within the same sample may be in different stages of the viral infection cycle even at the same nominal timepoint post infection. Therefore, cells with viral replication compartments and those containing viral assembly compartments can be observed next to each other. Because of the high multiplicity of infection, superinfection may lead to cells that contain more than one viral compartment.

Notably, the morphology of the viral compartment as assessed by fluorescence microscopy changes over the course of infection (**figure 4**). Early replication compartments show a compact and smooth spherical shape. Over time, the viral compartment becomes larger, less densely stained by Hoechst and more amorphous in shape as the viral cycle progresses and viral assembly is taking place as indicated by the appearance of A3-YFP signal. The assembly sites (sites where Hoechst DNA-stain and A3-YFP signal colocalize) can be subdivided into early assembly sites that still retain a largely spherical appearance and have only a few, dim spots of A3-YFP signal and late assembly sites that show very bright, abundant A3-YFP signal. These late assembly sites can also show distinct spots of very bright DNA signal, probably corresponding to highly condensed viral genomes. The morphological characteristics of the viral compartments in replication, early and late assembly stages observed in A3-YFP VACV infected cells are also distinguishable in the wild-type infected samples based on the Hoechst staining alone (**figure 4b**). This enables a comparison by fluorescence microscopy between the labeled and the wild-type virus and verifies that the progression of the viral infection cycle and the morphology of the virus-induced compartment are highly similar between the two systems.

In some A3-YFP virus-infected cells that contain late assembly sites, there is an additional area of bright A3-YFP signal concentrated next to the kidney-shaped nucleus. This corresponds to assembled virions clustering in the perinuclear region awaiting secondary envelopment or cell lysis for host cell exit. As this observation is contingent on the A3-YFP label, there is no equivalent to be observed in the wild-type samples.

The A3-YFP label can be used to localize the viral assembly compartment in infected cells after plunge-freezing under cryogenic conditions. This allows to specifically target lamella preparation to viral assembly sites for cryoET studies. **Figure 5** summarizes two such cryo-correlative light and electron microscopy (cryoCLEM) approaches which I applied to generate the data presented in this thesis. These two cryoCLEM approaches each used the microscope hardware available at the CSSB cryoEM platform at the time when the respective experiments were conducted.

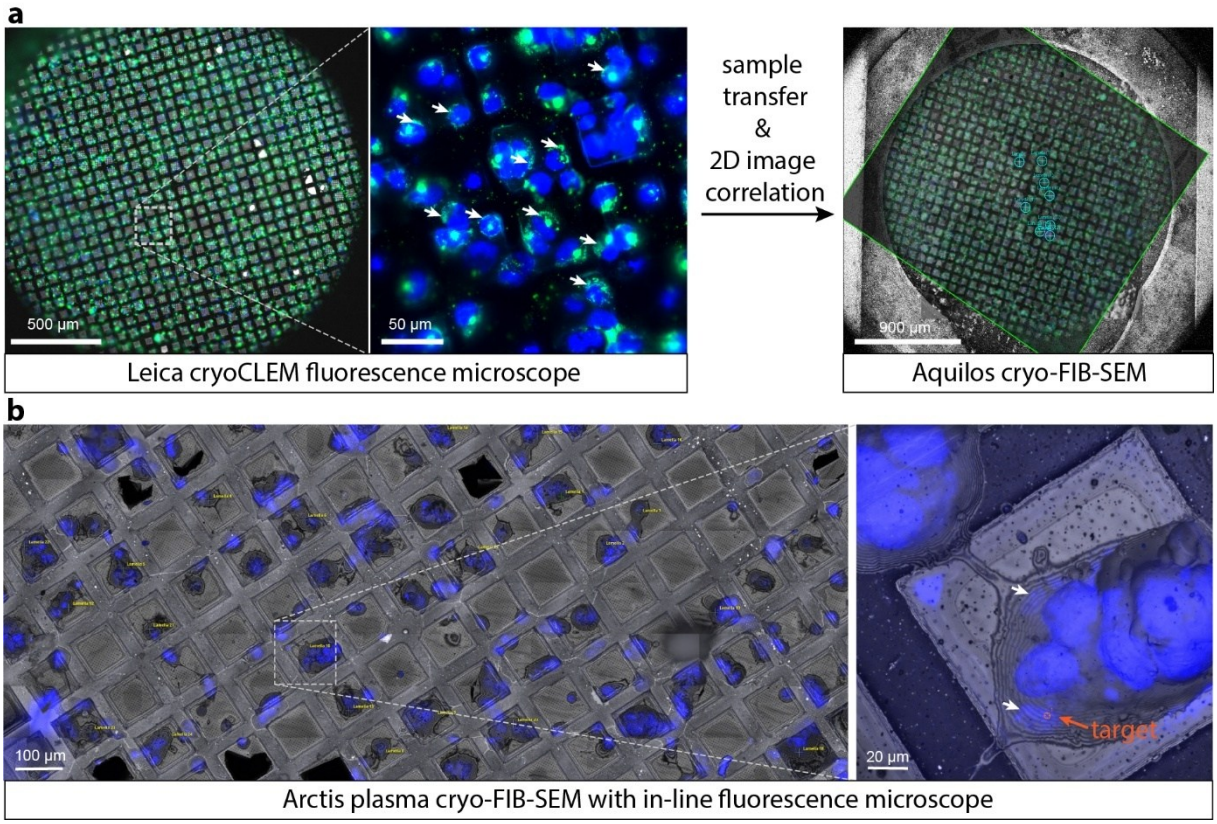

Figure 5: Comparison of cryoCLEM targeting approaches applied to A3-YFP and WT virus samples: Panel a) shows a grid with A3-YFP virus-infected cells, first imaged in a standalone Leica cryoCLEM wide field fluorescence microscope at low (left) and high magnification (middle). The blue channel displays Hoechst-stained DNA and the green channel the YFP-labelled viral core protein A3. The right panel in a) shows an SEM image of the same grid subsequently acquired on the Aquilos cryoFIB-SEM microscope overlayed with the correlated fluorescence image. Cells are chosen as targets for lamella production based on the YFP-signal (cyan crosshairs). Panel b) shows a wild-type sample imaged with the SEM and the integrated fluorescence microscope in the Arctis plasma cryoFIB-SEM system at low (left) and high (right) magnification. On the grid overview image (left), cells of interest for lamella production are annotated in yellow. The right panel shows the precise targeting of a viral assembly site (orange) for lamella production based on the extranuclear DNA signal. Viral assembly sites are indicated with white arrows.

Early experiments with A3-YFP virus (**figure 5a**) relied on a workflow employing two separate microscopes: a fluorescence light microscope with a cryo-stage for fluorescence data acquisition and the Aquilos cryoFIB-SEM system for SEM imaging and lamella preparation. The assembly sites in infected cells on the frozen cryoEM grid were identified in the fluorescence microscope based on the A3-YFP signal. After transferring the sample into the FIB-SEM system, the assembly sites were recovered on the SEM overview of the grid sample based on simple manual 2D image correlation and set up for lamella preparation. This approach allowed direct, albeit rough targeting in the xy plane, but provided no direct information about the positioning in z. The z height for manual lamella placement in the FIB-view therefore had to be estimated based on fluorescence z-stacks previously acquired.

This first cryoCLEM approach provided a means for rough targeting in 2D at the cost of time spent on fluorescence imaging as well as additional sample handling and transfers. Crucially, this also brings about an increased risk of atmospheric water accumulating on the sample in the form of contaminating ice crystals which cause problems during platinum coating and lamella milling. Notably, recognition of assembly sites solely based on extranuclear DNA signal (as described for room-temperature confocal microscopy) is not possible in this cryo-fluorescence microscopy setup due to limited resolution. The high abundance of assembly sites under my optimized experimental conditions and the fact that they occupy a large part of the cytoplasm as seen in **figure 4a**, raised the question whether fluorescence-based targeting was indeed required. In fact, omitting this targeting step and instead selecting lamella sites solely based on the FIB- and SEM views resulted in a sufficient success rate. In A3-YFP samples, more than 60 % of the lamellae produced with this “blind” milling procedure contained virus.

Despite the similarity of the A3-YFP and the wild-type virus systems as assessed by confocal microscopy of fixed room-temperature samples, the workflow established for cryoET sample preparation was not directly transferable from A3-YFP VACV infected cells to WT virus samples. Applying the blind milling workflow to WT-infected cells yielded no virus-containing lamellae in several independent experiments. Instead, these lamellae consistently showed disintegrating cytoplasm filled with vesicles indicative of dying cells. However, control cells left in the cell culture dish showed the expected phenotype with viral assembly sites in confocal fluorescence microscopy. Staining these samples with propidium iodide confirmed that there was no elevated number of apoptotic cells. Apparently, WT virus infected cells on cryoEM grids, but not those attached to the cell culture dish, were significantly less viable than cells infected with A3-YFP virus. Accordingly, the majority of analyses presented in this thesis were performed on data from the A3-YFP system.

During the course of this study, an Arctis plasma-FIB system with an in-line fluorescence microscope (iFLM) became available that also allowed a higher grid screening throughput. The increased resolution of the iFLM and the elimination of sample transfers between microscopes enabled the detection and direct targeting of viral assembly sites based on the Hoechst-stained DNA signal alone (**figure 5b**). Thus informed by fluorescence information directly on grids, I first optimized the sample preparation workflow for WT virus infected samples. Lowering the multiplicity of infection from 20 to 10 and switching from UltrAu foil to SiO_2 film grids resulted in viable WT samples exhibiting assembly sites on cryoEM grids. Targeting these sites in Arctis successfully produced WT virus-containing cryo-lamellae suitable for cryoET data acquisition and subsequent comparison to the A3-YFP-derived data.

3.2 The Viral Assembly Site

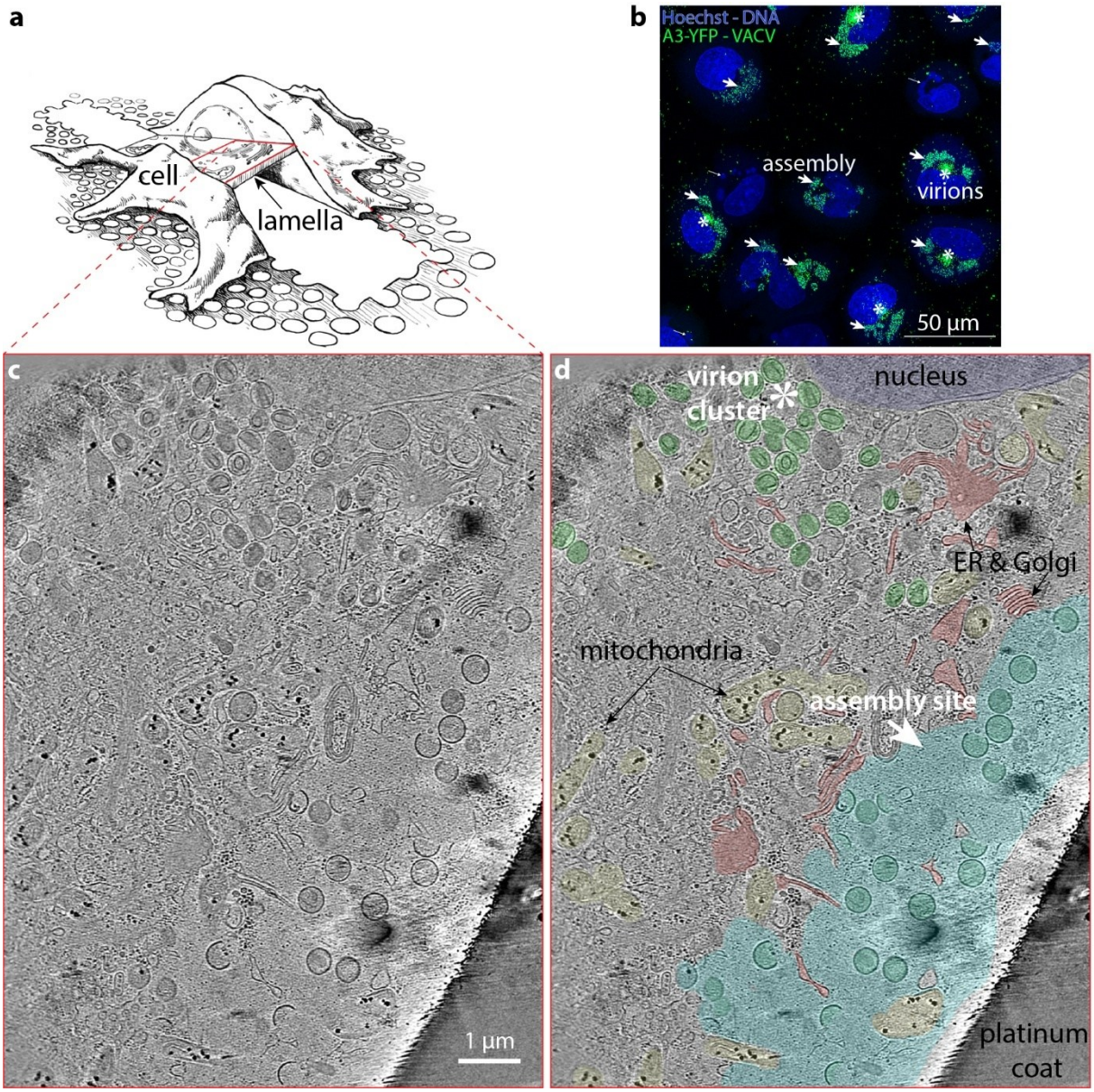

Figure 6: Overview of a lamella at the cryoTEM exhibiting VACV assembly observed directly inside the host cell cytoplasm: a) Schematic representation of a lamella milled into an adherent eukaryotic cell (reproduced from Villa et al., 2013 with permission from Elsevier and minor modifications). b) Representative fluorescence image showing typical features of A3-YFP VACV-infected HeLa cells at 8 hpi and reproduced from **figure 4a** of this thesis. c,d) Slice through an overview tomogram after reconstruction from a tilt series taken at low magnification on most of the lamella at the cryoTEM. In d), cellular features are annotated in black and highlighted by colouring (nucleus and nuclear envelope: dark blue, mitochondria: yellow, ER cisternae and Golgi stacks: red). Viral features are colorised in cyan (viral assembly site with crescents and IVs) and green (virions within perinuclear cluster) and annotated in white with symbols as in **figure 4**. The platinum coat deposited at the front of the lamella is also indicated.

The established workflows to obtain virus-containing cellular lamellae provide access to the interior of infected HeLa cells for transmission electron microscopy (TEM). Overview imaging reveals the reorganization of the cytoplasm on the sub-µm scale (**figure 6**). A typical example is shown in **figure 6c, d**, containing both a viral assembly site and a separate, perinuclear cluster of

virions. Both features correspond well to the organization as observed by fluorescence microscopy (**figure 6b**). The viral assembly site has an amorphous shape and no clear boundary or delineating structure such as a membrane or proteinaceous shell. However, it can be differentiated from the surrounding cytoplasm based on the observation that it contains typical crescent-shaped assembly intermediates and spherical virions. Simultaneously, cellular organelles such as mitochondria are being excluded, but are clearly visible in neighboring regions. The background granularity of this viral compartment is distinct from that of the surrounding cytoplasm, further indicating the exclusion of typical cellular components such as ribosomes and cytoskeletal elements.

Another population of viral particles is found outside of the assembly compartment in a cluster adjacent to the host cell nucleus. This localization corresponds to the bright clusters of A3-YFP fluorescence signals nested next to the nucleus typically observed in confocal microscopy of comparable samples. The viral particles found in these clusters have morphologies that are distinct from those found in the assembly site. One group comprises the mature virions that are electron-dense with brick-shaped membranes and complete internal core structures. More ovoid particles with only partially formed internal structures are also located there.

Targeting the viral assembly site for the acquisition of high-magnification cellular tomograms provides more detailed information about its organization and viral assembly intermediates on the nm scale (**figure 7**). To aid the analysis of the tomographic data, I performed segmentations of densities belonging to identifiable biological objects in the tomogram volume. Such volume-based segmentations provide a three-dimensional representation of these biological structures (**figure 7c**). Of note, these segmentations miss out on membrane areas that are oriented parallel to the image plane as their density is obscured by the missing wedge artefact inherent to tomography. A tomogram acquired at the edge of a viral assembly compartment shows the distinction between the area occupied by the viral factory and the adjacent cytoplasmic area (**figure 7**). While the latter is populated by a relatively high number of ribosomes and actin filaments, these elements are less frequent in the viral assembly site. This exclusion of specific components without a physical barrier is reminiscent of liquid-liquid phase separation phenomena or molecular crowding and appears to play a role in supporting viral assembly by promoting the concentration of specific components. In contrast to other cytoskeletal elements such as actin, microtubules seem to be less strictly excluded from the viral assembly compartments and are regularly observed in the vicinity of immature virions and crescents.

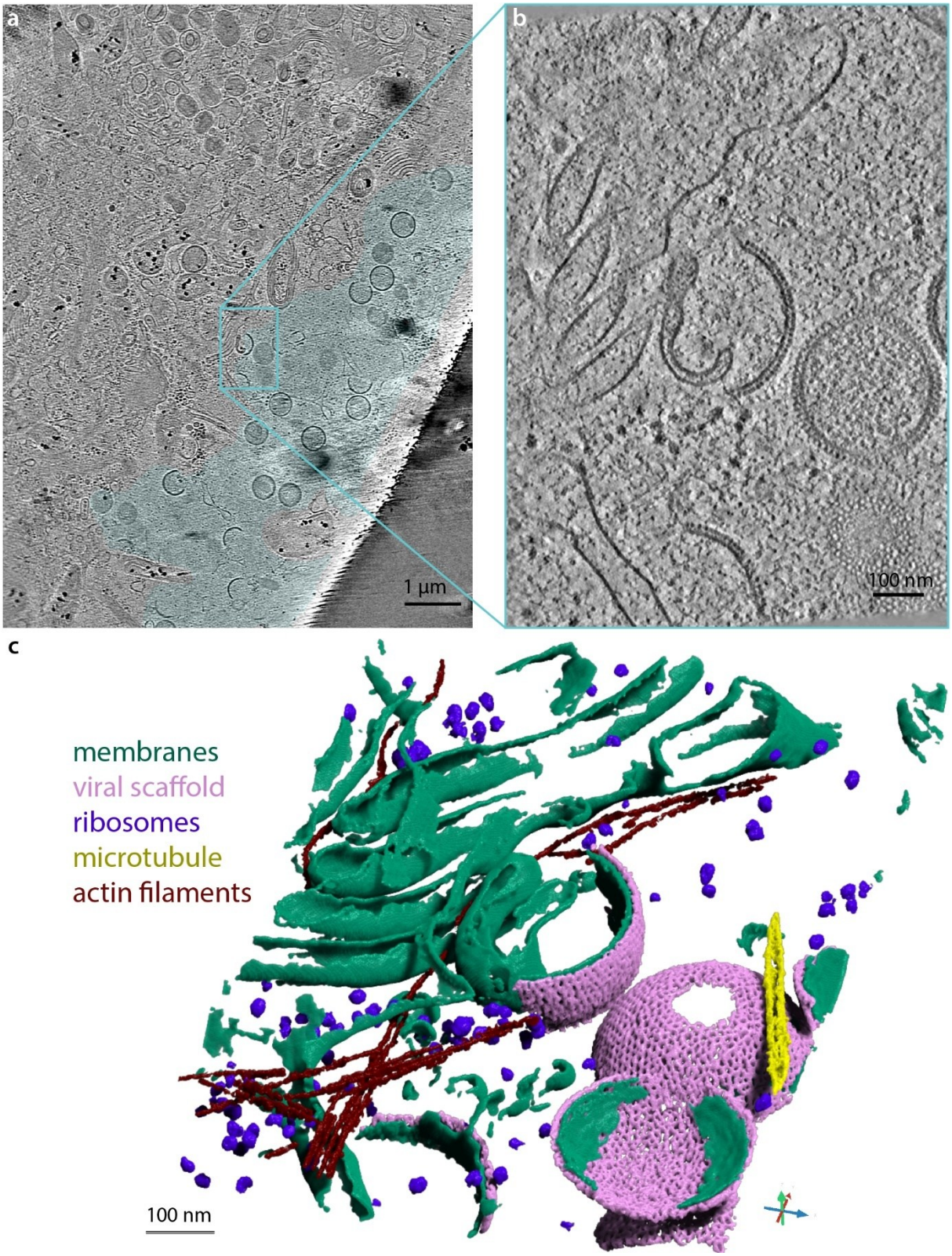

Figure 7: The edge of a viral assembly compartment: Panel a) is a section of figure 6d with the viral assembly site highlighted in cyan. The high-magnification tomogram M2_027 in b) was acquired on the boxed-in region. In b), a slice through the tomographic volume is shown and c) displays an annotated 3D rendering of the segmented biological features it contains. It shows Golgi stacks, ER membranes and cytoplasmic components on the left side, while the assembly site on the right side is occupied by assembling vaccinia virions (membranes covered in viral scaffold). The missing membrane density in the bottom right corner is caused by the missing wedge artefact.

3.3 Semi-Automatic Segmentation

As illustrated in the previous chapter, volume-based segmentations of tomographic densities and their 3D rendering are a powerful tool for the analysis of complex biological structures in their cellular context. This is particularly true for large structures such as the poxvirus crescents and immature virions that cannot be fully represented in 2D slices alone. For the systematic analysis of poxvirus assembly intermediates presented in this thesis, access to a large set of segmented viral particles and their environment was essential. To achieve the required segmentation throughput, I established a deep learning-based semi-automatic workflow for whole tomogram segmentations like the one shown in **figure 7c**. This workflow uses the software Dragonfly and is inspired by published protocols (Heebner et al., 2022). All tomograms used in this pipeline were consistently filtered and pre-processed to optimize reproducibility and transferability between datasets.

Training a neural network for the segmentation of whole tomogram volumes requires segmented ground truth training data. To generate this training data for a given tomogram, a small region of interest (ROI) containing examples of all relevant biological features was defined first. Within this designated training ROI, biological features were manually segmented based on their electron-density with a thresholded drawing tool. Depending on the biological contents of the respective tomograms, three, five or seven different classes were segmented, including always a background class, membranes and the viral D13 scaffold, microtubules and (actin) filaments if present, and later two additional classes for ribosomes and the structured VACV genome. Notably, membrane densities were not annotated completely manually at this step, but derived from the external, automatic membrane segmentation tool memBrain-seg (Lamm et al., 2024) and corrected manually.

With such a small dataset, automatic segmentation models of a U-Net neural network architecture can be trained. This type of network is particularly suitable for cryoET data annotation with only a limited amount of segmented training data as it uses data augmentation prior to training (Heebner et al., 2022; Ronneberger et al., 2015). This means expanding the input training dataset through translation and rotation, elastic distortions and intensity-modulating operations, thereby increasing the available amount of training data and robustness. 3D and 2.5-dimensional network architectures were tested, which work either on the whole volume or on sets of adjacent 2D image slices. 2.5D U-Nets performed better than 3D and required significantly fewer computing resources and time for both training and prediction. Therefore, the results presented were obtained using 2.5D networks.

Training was performed in two or three iterations of 50 training epochs to achieve model convergence. This was monitored during training by observing the learning curve depicting the categorical cross-entropy loss function drop consistently and eventually flatten out, asymptotically approaching a value close to zero. After each round of 50 training epochs, the trained model was applied to the whole tomogram volume to visually assess the predictive segmentation performance. If necessary, the predicted segmentation was manually corrected in a new, larger training ROI and used as input for the next training iteration until the training converged and resulted in a model that accurately predicts the whole tomogram segmentation with only a minor need for manual corrections.

A problem frequently encountered in the early stages of training a new network was that the network minimized its loss function by assigning all voxels to the background class – which is invariably the largest class in the input training data – and failing to segment all other classes. In such cases, the loss function in the learning curve dropped drastically within one epoch very early on in training and then remained flat with no further (gradual) reduction of the loss function. This issue could therefore be systematically diagnosed directly from the learning curve in real time – early on during network training – without the need to visually assess model output. The training was then terminated early, and training parameters adjusted before re-training. Increasing data augmentation as well as training patch and batch sizes improved training performance and helped to avoid this background overfitting which can be understood as a local minimum in the optimization landscape. The most effective mitigation strategy was found to be the use of custom weights assigned to each class prior to training. By up-weighing the relevant non-background classes with respect to the background by factors of 4-10 it becomes less favorable for the model to miss-label them as background.

Successfully trained models performed well in automated segmentations of the tomograms from which small ROIs were used as training data, but transferability between datasets varied. In most cases, a pre-trained model was able to predict the segmentation of a new tomogram reasonably well. However, the same model would perform poorly on some other tomograms, even under favorable conditions such as tomograms being acquired with the same imaging parameters and identical pre-processing. One such example of poor transferability is shown in **figure 8**. In these cases, two mitigation strategies have proven effective. If the tomogram to be segmented contains all the classes included in the original model, the model can be re-trained. Otherwise, a new model must be created. Both strategies are analogous to the original training workflow described above: the erroneous predicted segmentation is manually corrected in a small, defined ROI to serve as training data in subsequent model (re-)training (**figure 8a, b**). After two iterations, a

reasonably good prediction is achieved that can be quickly cleaned and corrected to arrive at a whole tomogram segmentation (**figure 8c**). In this example, the model predicted the cellular and viral membranes as well as the viral scaffold, while the structured viral genome and ribosomes were added to the segmentation manually.

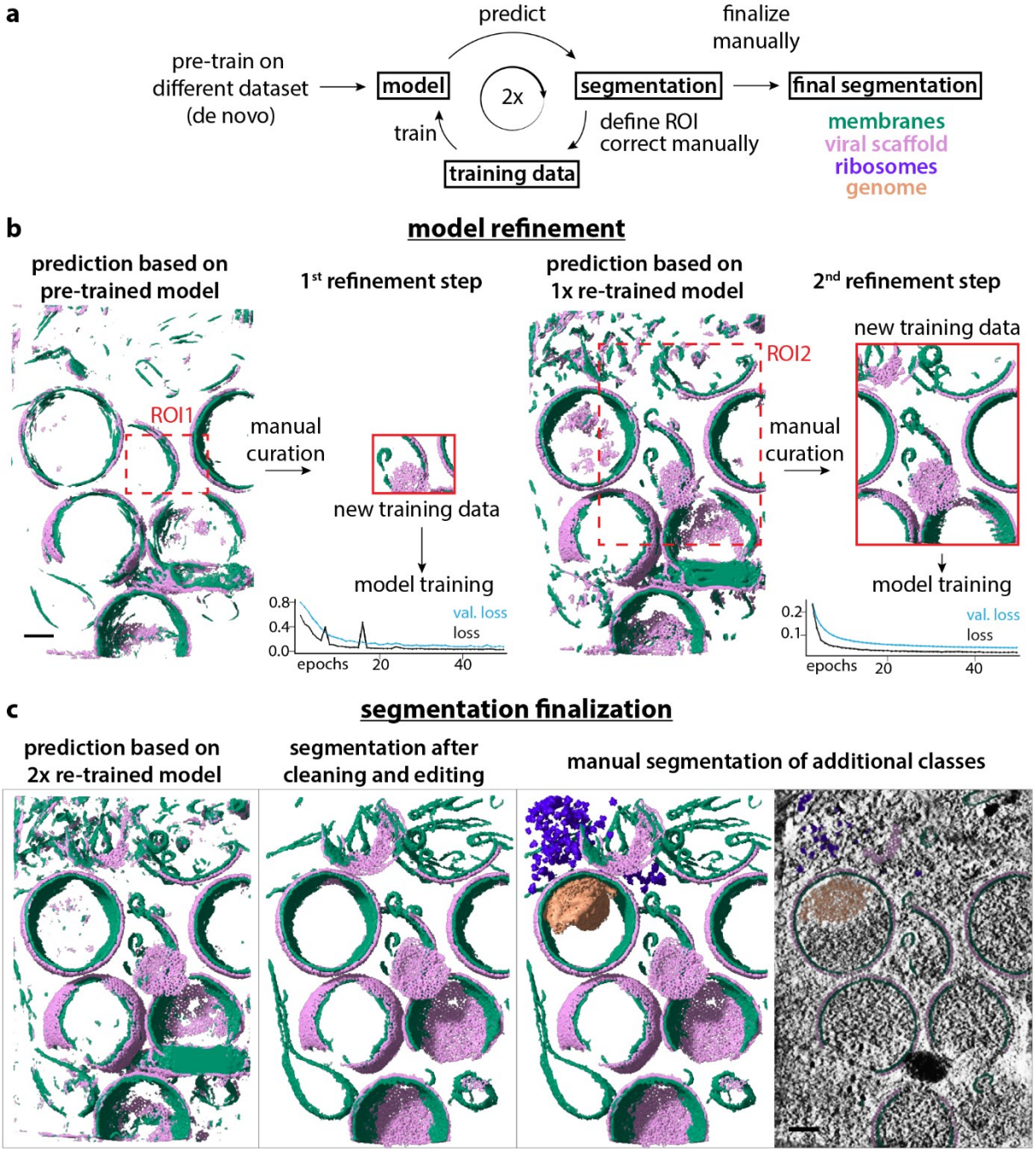

Figure 8: Semi-automatic tomogram segmentation workflow exemplified on tomogram M008: a): schematic workflow employed to train a U-Net model iteratively on manually curated training data and to predict whole tomogram segmentations. The iterative model refinement steps (b) and final manual curation of the segmentation (c) are illustrated with the example of one tomogram for which the initial model, that was pre-trained on a different dataset, performed poorly (b, left). The improvement of the model during consecutive rounds of training with new data is observed through the decrease in the categorical cross entropy loss function on training and validation sets (b, bottom panels). All scale bars indicate 100 nm.

3.4 Viral Assembly Intermediates

3.4.1 Crescent growth

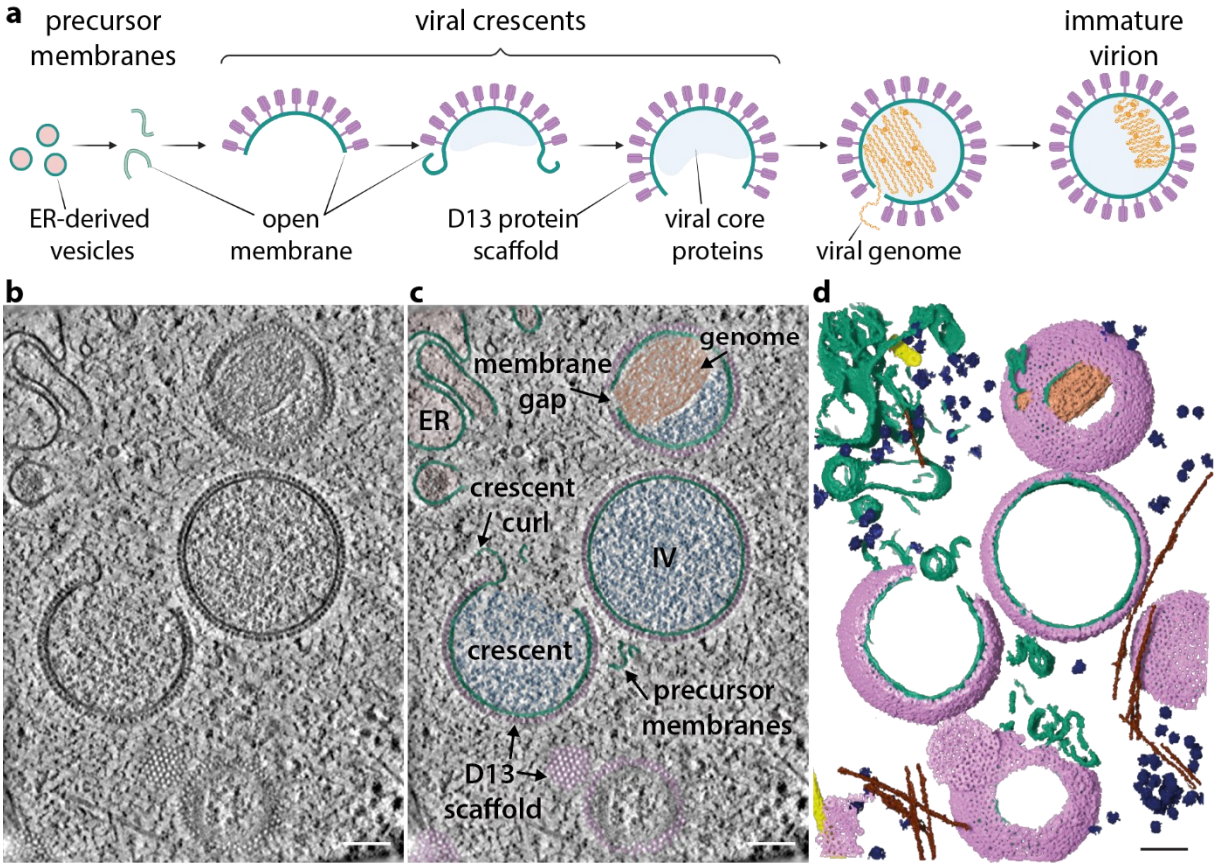

Figure 9: Viral assembly intermediates observed in the assembly site: a): scheme of assembly intermediates leading up to IV formation. b) and c) show a slice through tomogram M2_028 with features annotated according to the color scheme introduced in a). Panel d) shows a 3D rendering of the segmented densities in the same colors. Additional features in d) are ribosomes, microtubules and actin filaments in dark blue, yellow and brown, respectively. All scale bars indicate 100 nm.

Having established the segmentation workflow, I was able to thoroughly characterize VACV assembly sites from 6 tomograms. These segmented tomograms were chosen to be representative of the viral structures observed throughout the A3-YFP VACV dataset. Within the assembly compartment, all the intermediates of the proposed assembly mechanism from small precursor membranes up to immature virions (**figure 9a**) are found and amenable to detailed analysis.

The earliest stage are small pieces of membranes in the viral factory, both in the form of small vesicles (30 – 70 nm diameter) and opened membrane sheets, as observed in 2D slices through the tomograms as well as in three-dimensional analysis of the segmented membrane densities (**figure 9**). The next stage observed are viral crescent membranes which are defined by their open membrane ends and the associated viral protein scaffold which imposes their fixed curvature. The crescents are observed in various sizes, ranging from small, curved patches over quarter- and

half-spheres to almost completely closed, spherical shapes that approximate the complete, spherical immature virion (**figure 10**). Interestingly, curling membranes that are not covered by scaffold proteins are commonly observed at the open ends of membrane crescents (**figures 9, 10b, c, e**). These membrane curls are comparable in size to the small vesicles and ruptured precursor membranes in the vicinity and are in direct continuity with the D13-covered viral membranes. This observation supports a continuous growth model in which the observed intermediates are snapshots of the assembly mechanism (Moss, 2018). Apparently, viral crescents grow stepwise by continually incorporating new, small pieces of membranes from the pool of ruptured precursor membranes available in the assembly site. Subsequently, these membrane areas, too, are coated with the D13 protein scaffold that imposes the membrane curvature typical of IVs.

Notably, no larger protein complexes can be observed at the open ends of the crescent membranes that might protect them. Bearing in mind the size limitations of cryoEM and cellular cryoET in particular, this suggests that if such open ends are specifically stabilized inside the host cytoplasm, then this must be achieved through smaller components like small viral membrane-embedded proteins or specialized lipids.

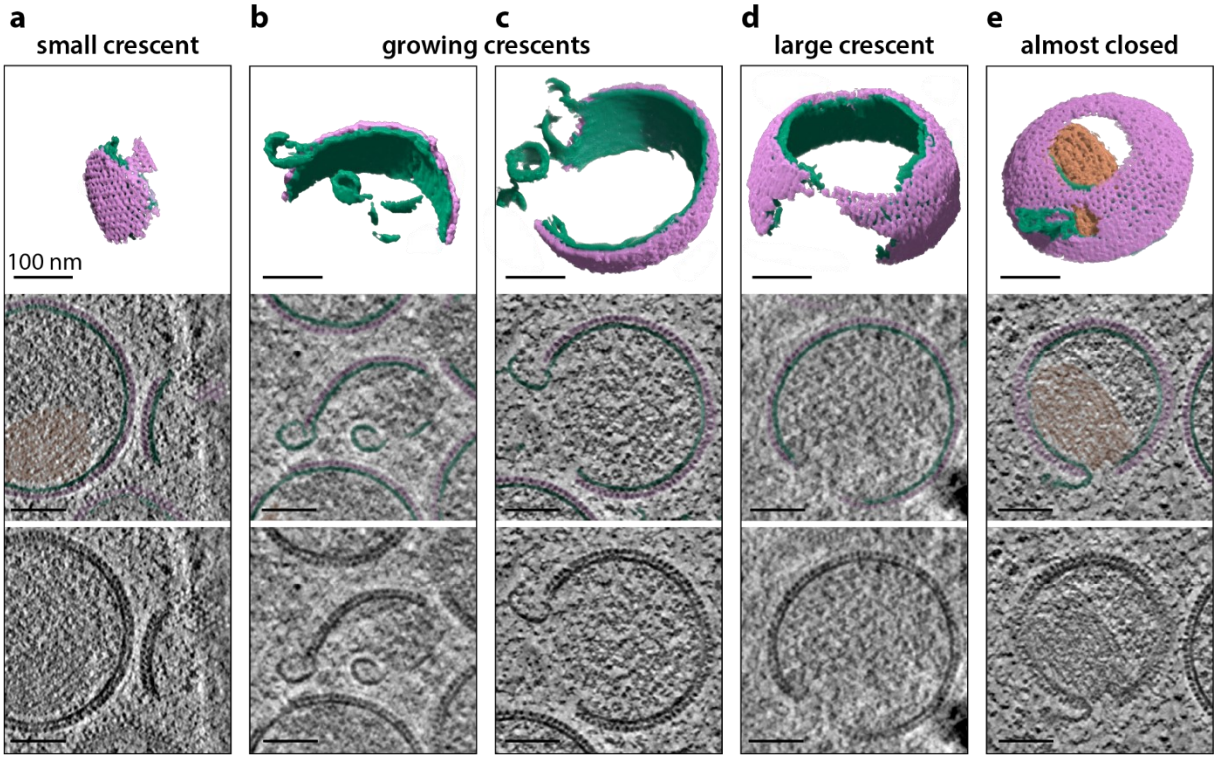

Figure 10: Viral crescents observed in consecutive stages of growth: Representative crescents for each stage are taken from tomograms F043 (a), M008 (b, d), M2_028 (c, e) which are shown in full in figures 11, 8 and 9, respectively. The top panels show a 3D segmentation, middle and bottom panels show tomogram slices. Colors in top and middle panels: viral D13 scaffold – pink, membranes – green, viral genome – orange. All scale bars indicate 100 nm.

Not all virions in the assembly site are perfectly spherical, as illustrated in **figure 11**. Though less frequent than the canonical shapes described previously, crescents are sometimes observed in warped, aberrant shapes that deviate from the ideal crescent shape and could not be extrapolated into a sphere. In addition, other crescents can be found grouped together with their open ends facing each other. Together, such apposing crescents approximate spherical or more ovoid shapes. Potential fusion events between such apposing crescents might result in the formation of non-spherical, ovoid IV. However, it is not clear whether apposing crescents are capable of fusing and if such ovoid IVs contain a genome and represent functional particles.

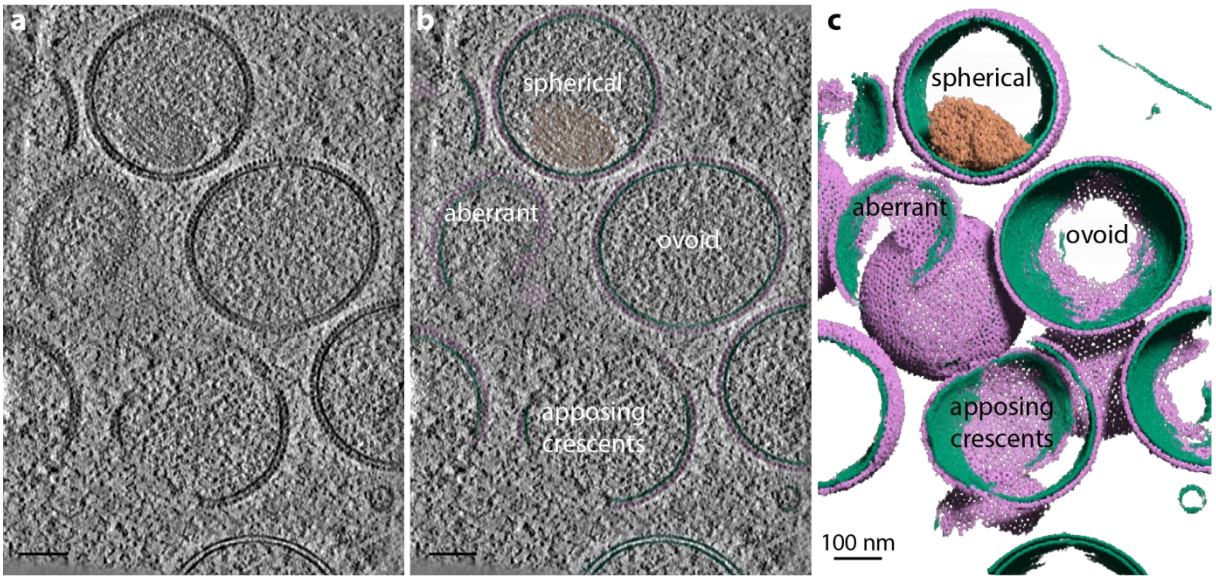

Figure 11: various morphologies of IVs and crescents: Panels a) and b) show a slice through tomogram F043 with annotations and highlights in b). Panel c) shows a 3D rendering of the segmented densities. Colors in b) and c): viral D13 scaffold – pink, membranes – green, viral genome – orange. All scale bars indicate 100 nm.

One fundamental limitation of the membrane segmentations presented here is the artefact of the missing wedge which is inherent to electron tomography and results in a very limited resolution along the axis that is perpendicular to the sample plane (z axis in this case). This results in a smearing of the image volume along this axis, rendering densities that lie flat within the sample plane less visible, particularly severely affecting membrane densities in this plane, as their appearance in such tangential views is relatively featureless to begin with. Therefore, the crescents and IVs presented here appear to have missing membrane areas on the top or bottom where no densities could be segmented due to the missing wedge artefact. The presence of a membrane can however be inferred in these cases due to the presence of the D13 scaffold that is decorating the membrane and provides a strong enough signal to be identified and segmented even in such tangential views.

The assessment of full sphericity and closedness of the membrane and therefore the distinction between large crescents and immature virions is limited by the sample preparation through FIB-milling. As the VACV immature virion has a diameter of ~ 350 nm, whole virions are too large to be contained within a cryo-lamella, which are thinned down to 100 – 250 nm for optimal electron transparency and image contrast formation. Therefore, the analysis is based only on the part of each virion that is accessible in the sample volume and the number of virions that are classified as "immature virion", i.e. having a fully closed membrane is likely an over-estimate. A table of the tomograms presented here, and their corresponding lamella thickness is found in methods chapter 6.6. To balance the needs of achieving a good signal to noise ratio for high-resolution structural analysis by producing very thin lamellae and the need for larger sample volumes for a thorough representation of the assembly site and contextual analysis, lamellae of varying thickness were prepared. Thus, the dataset contains lamellae within a thickness range from 100 nm to 450 nm, the former optimized for good contrast as well as high resolution at the expense of sample volume and context, the latter optimized for context at the expense of resolution and contrast.

3.4.2 Genome incorporation

Closedness of the membrane and full sphericity as markers of complete immature virion formation can only be partially assessed within this dataset. However, a further distinguishing feature is the presence of the viral genome as a nucleoid (L. Liu et al., 2014). The incorporation of the genome is one of the last steps in immature virion formation prior to the sealing of the viral membrane (**figures 9, 12**). The observed genomes are not in the form of amorphous DNA, but structured and distinct from the background, rendering them visible as a distinct entity in tomograms. Observing such a nucleoid within an immature virion provides confidence in the assignment of that virion as a closed IV as opposed to a large crescent with a membrane opening that lies outside of the lamella sample.

Within IVs, the viral DNA genome has a striated structure composed of regularly spaced, dense filaments and appears anchored to the viral membrane at multiple points (**figure 12a**). Interestingly, similar structures of condensed genome are sometimes observed free within the viral assembly site without any direct contact to viral particles or assembly intermediates (**figure 12b**). The presence of these nucleoid structures strongly suggests that the DNA is present in complex with viral proteins fulfilling a histone-like function. To date, no such DNA-binding and structuring proteins have been identified for VACV (Greseth & Traktman, 2022).

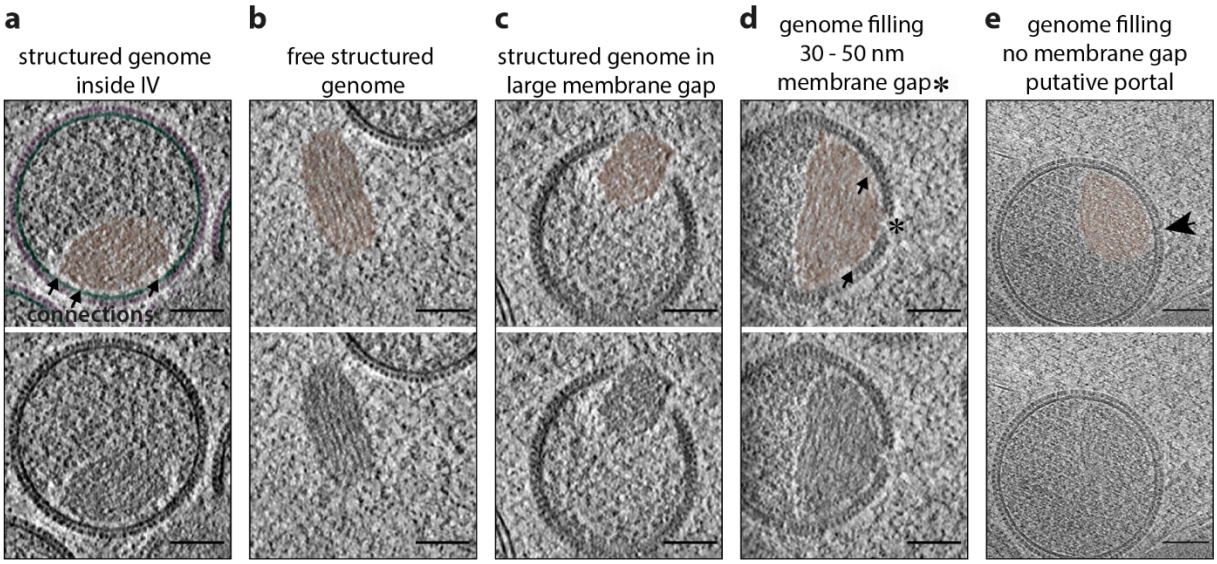

Figure 12: Genome structure and intermediates of genome incorporation: Representative slices for each state were taken from tomograms F043 (a), F046 (b), F044 (c), F048 (d), and M021 (e). The virions in c)-e) are found at tomogram edges and cannot be shown more completely. In the top panels, the structured viral genome is highlighted in orange. Apparent connections between the genome and the viral membrane are indicated with black arrows in a) and d). The asterisk in d) indicates a small membrane opening. In contrast to the deconvoluted tomograms in a)-d), the tomogram in e) is shown after SIRT-like filtering to retain more details of the indicated putative portal density (arrowhead). All scale bars indicate 100 nm.

The process of DNA uptake into the nascent virion can also be observed in this dataset (**figure 12c-e**). These snapshots of viral genome incorporation can be divided into two types: Some viral particles with only a small membrane opening show condensed viral genome structures on the inside, in direct proximity to the opening (**figure 12d**). In one of these cases (**figure 12e**), the pore in the viral membrane is truly minimal (17 nm diameter) and occupied by a distinct visible density. In accordance with one proposed model for poxvirus genome incorporation, this density could be a portal formed by the described viral DNA packaging ATPase A32 (Greseth & Traktman, 2022). In my dataset, the case depicted in **figure 12d** is the most frequently observed type of active genome packaging, with membrane openings ranging 30 – 50 nm in diameter. Other, rare events show the already condensed genome apparently being engulfed by growing crescents with a much larger membrane opening of ~ 100 nm (**figure 12c**).

These observations of virions in the process of incorporating DNA suggest at least two distinct pathways of genome uptake. An alternative explanation for the phenotype shown in **figure 12c** and the free structured genomes could be the loss of nucleoids from defective viral particles after genome condensation and packing.

3.4.3 Membrane curvature

Even though the observed virions are not all perfectly spherical, the overall curvature of immature virions and crescents seems remarkably consistent. All scaffold-covered viral membranes, open or closed, show similar curvedness of around 0.0075 nm^{-1} as determined by vector voting analysis of polygon mesh surfaces derived from membrane segmentations of tomographic data (**figure 13**). However, at the open ends of crescents, where new membrane pieces are being incorporated, the local curvature tends to be much higher, around 0.04 nm^{-1}. At the junction between the D13-covered and uncovered parts the curvature is inverted with respect to the virion surface. These curling membrane areas at the edge of crescents often have a curvature that resembles that of the presumed precursor vesicles and ruptured membrane pieces found in the viral assembly site (**figure 13b, c**).

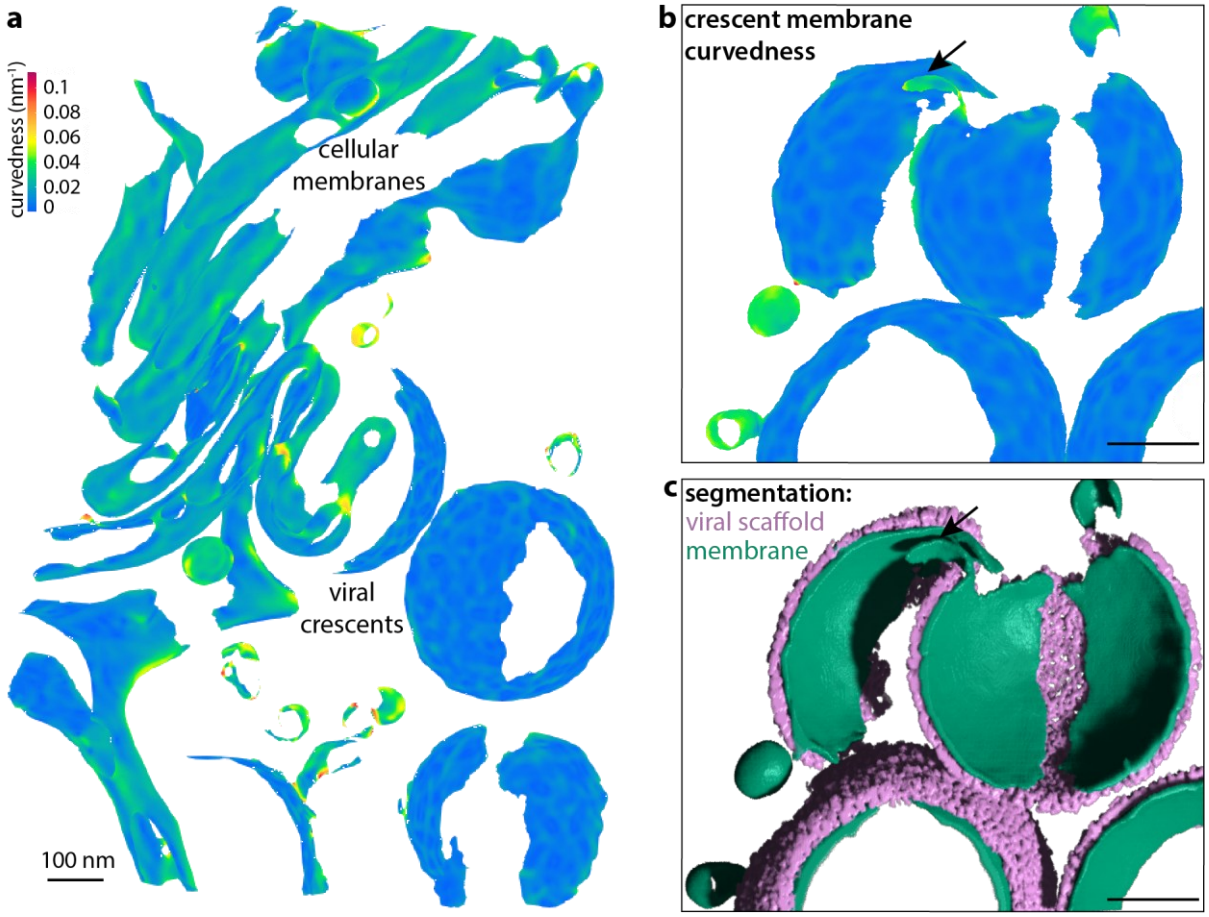

Figure 13: Local membrane curvature analysis: Panels a) and b) show polygon mesh surfaces of segmented membranes colored according to the local membrane curvedness in nm^{-1} determined by pyCurv (Salfer et al., 2020). a): viral and cellular membranes from tomogram M2_027. b): viral crescents and vesicles from tomogram M023, c): corresponding segmentation with membranes in green and viral D13 scaffold in pink. The open membrane at the curling end of a crescent is not covered by D13 and displays a different curvature from the overall viral membrane as indicated in b) and c). All scale bars are 100 nm.

Locally, there are ripples in the viral membranes that lead to locally varying membrane curvatures in the range of 0.0015 to 0.02 nm^{-1}. This wave-like pattern seems to be especially pronounced in viral membranes but is noticeably absent in regions not covered by the scaffold protein D13. This might hint at a connection between the local organization of the scaffolding lattice and the membrane properties below.

3.5 The Viral Scaffold Protein D13

3.5.1 The D13 lattice and its defects

In 2D slices through the tomographic volume, the scaffold protein D13 that covers the viral membrane of crescents and immature virions has distinct appearances depending on the viewing direction. From the side, it appears like spikes protruding from the membrane. When viewed from the top, a continuous honeycomb-like lattice becomes apparent (**figure 14b**). The electron density-based voxel segmentation in **figure 14a** shows the honeycomb lattice in three-dimensions on the curved surface of viral membranes.

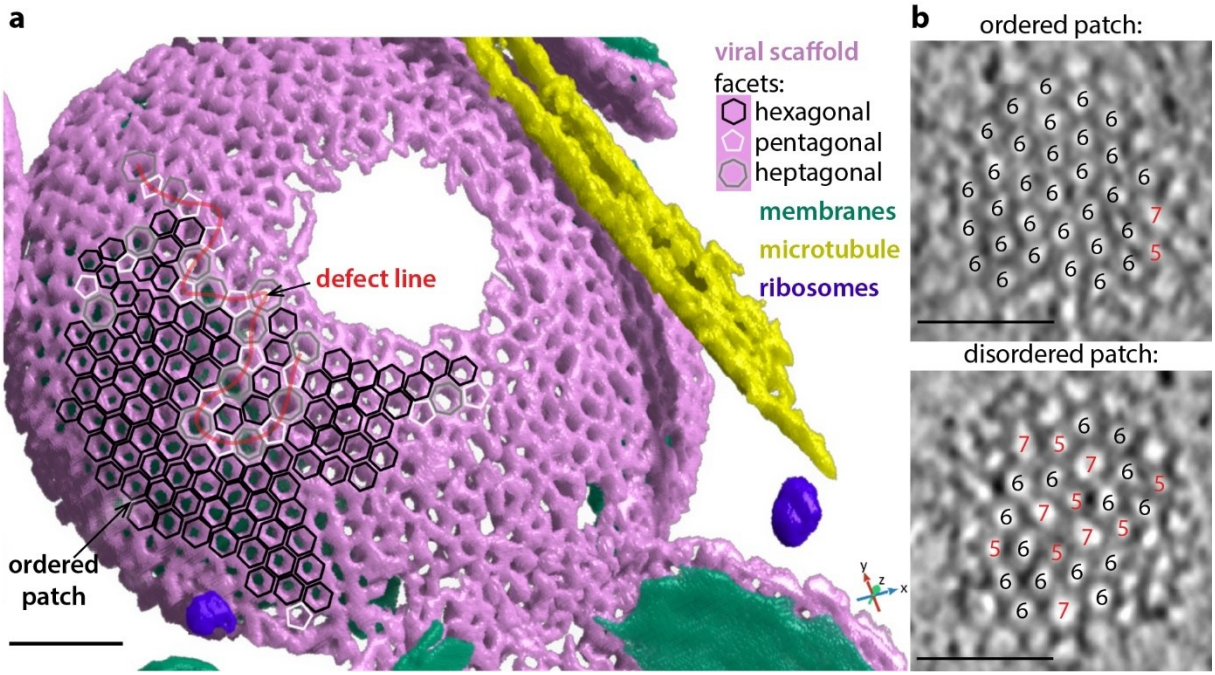

Figure 14: Symmetry breaks in the lattice of the viral D13 protein scaffold: In panel a), segmentation of an IV from tomogram M2_027 shows the facets of the D13 protein lattice forming the viral scaffold. A select region of the segmented lattice is annotated with hexagons, pentagons and heptagons according to the underlying symmetry of the individual facets. This shows ordered patches of hexagonal symmetry as well as heptagonal and pentagonal facets in a defect line (annotated in red). Panel b) shows slices from tomogram F043 with two different patches of D13 top views: one with high hexagonal order that is broken only at the edge (top) and one with numerous heptagonal and pentagonal defects (bottom). All scale bars indicate 50 nm.

Both segmentation of and slices through the original electron density data allow to identify individual facets of the lattice. These facets are mostly hexagonal, consisting of six trimers of the D13 protein each and sharing trimeric subunits with their neighboring hexagonal facets

(**figure 15**). However, these hexagonal facets can only cover patches of limited size on a curved surface and require symmetry breaks. An analysis of the symmetry arrangement of the honeycomb facets observed on the viral membrane in 3D allows a more accurate description of the lattice. For this, the symmetry of any given D13 facet was defined based on the number of neighboring facets with whom it shares a common edge. Large parts of the surface are indeed covered by D13 patches of high hexagonal symmetry, but they are invariably broken by defect lines consisting of facets with alternative symmetries, namely pentagonal and heptagonal facets. **Figure 14** illustrates these three types of facet geometries on the segmented lattice and in tomographic slices and the absence of a clear long-range symmetry.

3.5.2 Custom D13 subvolume averaging workflow

To gain a deeper molecular understanding of the D13 scaffold *in situ*, I developed and employed a custom subvolume averaging workflow to extract individual D13 lattice facets as particles and obtain their average structure. In this workflow, the main focus is on the hexagonal facets as they are the most abundant regular structure within the D13 lattice. The workflow itself is comprised of three consecutive steps of increasing automation, resulting in a scalable SVA particle picking pipeline tailored to D13.

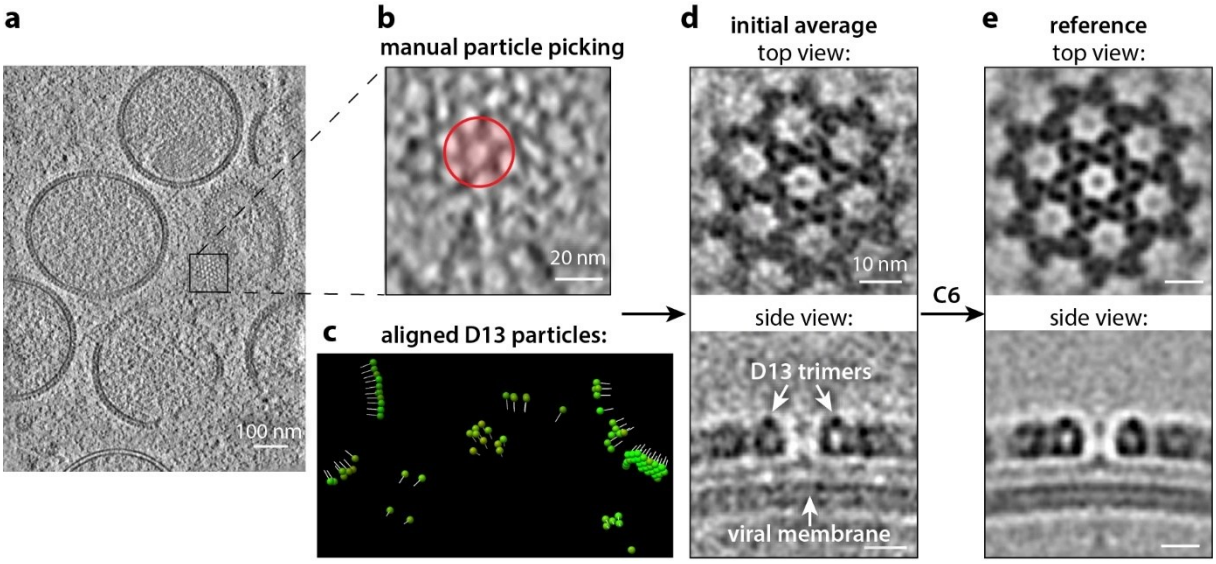

Figure 15: Generation of an initial average structure of hexagonal D13 facets: a, b): 105 hexagonal particles as defined by the red highlight were manually selected for SVA from tomogram F043. c): Positions (green spheres) and orientations (indicated by white pins) of the particles after alignment are visualized in the tomogram coordinate space. For clarity, a cropped image is displayed here. d) and e) show slices through the average volume before and after application of C6 symmetry. The latter is used as a reference in subsequent SVA workflows.

The first step of my workflow aimed at obtaining a good reference volume for alignment of the particles in subsequent subvolume averaging (**figure 15**). To avoid bias that can arise from imposing an external reference, this reference volume was generated from 105 carefully

manually picked hexagonal particles from the dataset itself. The chosen particles sample a wide range of orientations with a general side- to top-view ratio of 80:20 (**figure 15b, c**). In this context, a particle is defined as one hexagonal facet of the D13 lattice with the center position of the picked particle positioned in the empty space at the center of the hexagon. The initial average volume is based on particles picked selectively in regions with good hexagonal symmetry. There, neighboring particles co-align cleanly with the central hexagon despite being excluded from alignment by masking. Thus, the resulting average volume contains 7 interconnected hexamers of trimers, sharing two trimeric subunits each (**figure 15d**). After an initial C1 alignment with no imposed symmetry resulted in a clearly hexagonal average volume, C6 symmetry was applied and subsequently relaxed to yield an average volume with an increased SNR to use as a reference volume in the downstream subvolume average processing (**figure 15e**). At later stages in the workflow, more particles are to be included in the average, also from regions with more heterogeneous symmetries. Therefore, it is important to consistently mask out the neighboring facets to focus the alignment exclusively on the central hexagon to avoid losing particles or blurring the average.

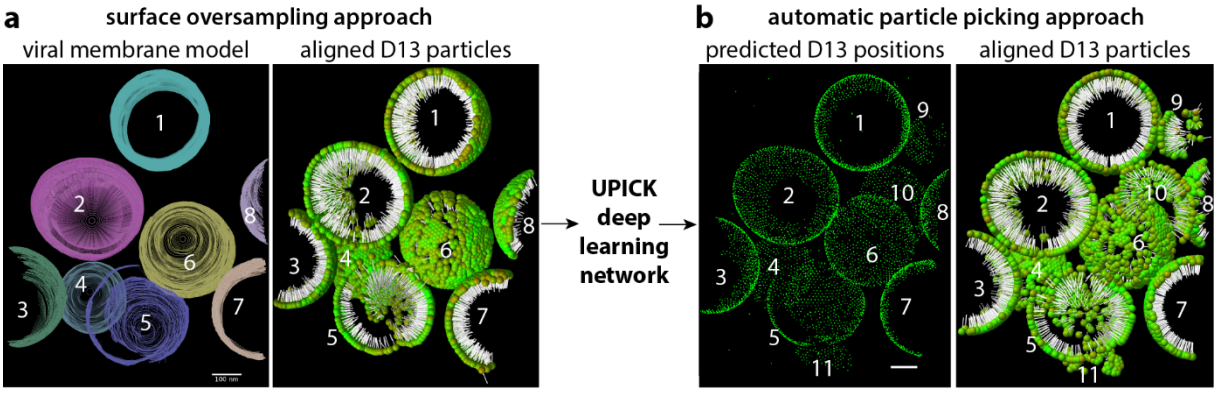

Figure 16: Semi-automatic and automatic D13 particle picking strategies illustrated on tomogram F043: Panel a) shows the semi-automatic oversampling approach based on a viral membrane surface model manually generated in IMOD (left). 8 viral particles (IVs and crescents) were modelled in this tomogram. The right panel shows aligned D13 particle positions (green spheres) and orientations (white pins) after template-matching the oversampled positions against the hexagonal D13 reference from fig.12e). The resulting positions were used to train the Bayesian Flow network UPICK for D13 particle detection. Panel b) shows the D13 coordinates picked by the trained network (left) and the positions and orientations of the corresponding D13 particles after alignment (right). The network detects D13 particles also on virions that were not part of the training data (9 -11 in b).

In the second step, the workflow was extended to extract D13 particles from virion surfaces. Automated membrane segmentations are not suitable to define these surfaces because they miss part of the membrane in the tangential views, where it is invisible due to the missing wedge. In these regions, however, D13 top views of the lattice are still clearly visible in the tomograms and should be sampled. Therefore, the viral membranes of crescents and IVs in two tomograms

were manually modelled using the drawing and interpolation tools in IMOD following published protocols (Danita et al., 2022). Where the missing wedge obscured the membrane density itself, model points for the viral surface were drawn at the inferred membrane position below the visible lattice (**figure 16a**).

This membrane model was used to oversample the virion surface using PEET in template matching mode. For this, the model points were first initiated as particles oriented towards the center of the sphere that best approximates the corresponding virion surface. The particles were then aligned against the D13 reference volume (**figure 15e**) without updating the reference. Subsequent removal of duplicate and ill-aligning particles resulted in a set of ~ 5000 hexagonal D13 facet particles sampled across the accessible virion surfaces for further iterative, increasingly fine alignment. **Figure 16a** shows the aligned particles obtained from 8 exemplary virions.

While the template matching alignment is well-automated within PEET, the need for a manual membrane model limits the throughput achievable with this method and consequently the number of particles available for averaging. As a third and final step, I therefore implemented an automated, deep learning-based particle picking approach in collaboration with the laboratory of Prof. Maya Topf to circumvent this problem. The manual viral membrane models and the D13 particle coordinates after alignment and cleaning of the particle set were provided as input for the training of a neural network, in the following referred to by the name UPICK (**figure 16**). Ultimately, this Bayesian Flow Network is intended to allow the automated annotation of densities in cryoET data with no need for user-guided training or annotation. To this end, several pre-defined and pre-trained classes are needed during development. My membrane data was added to the training data on the already existing membrane class. The picked D13 particles were used to train a new class for protein scaffolds that was added to the model to make it more comprehensive and universal.

After being re-trained on a dataset containing my data, UPICK was able to annotate the positions of D13 facets on virions not included in the training data (**figure 16b**). This version of the network was transferable to other tomograms for D13 particle picking purposes and was fixed under the name UPICK-v2. This network generates binary spheres around the center positions of D13 facets that must be translated into particle model files for PEET input. Using custom scripting, I developed a respective processing workflow that is detailed in the methods section 6.5.3.

With this tailored automated approach, SVA-compatible D13 facet positions can be extracted across datasets with only minimal manual user input. The predominant factor limiting the number

of particles that can be included in this analysis is now the reconstruction of high-quality tomograms to pick particles from. This was done using careful manual fiducial-based tilt series alignment in IMOD, which is both time-consuming and contingent on the serendipitous presence of suitable gold or platinum fiducial markers on the lamella. So far, four of these tomograms were analyzed with UPICK-v2, yielding ~20,000 particles. After particle extraction, alignment, cleaning and rigorous selection by cross-correlation, approximately 5000 refined particles were included for processing of the final subvolume average (**figure 17**).

3.5.3 The quaternary structure of D13

By subvolume averaging, the structure of the hexagonal facets found in the D13 lattice inside VACV-infected cells was determined at an overall resolution estimated to 17.5 Å by Fourier Shell Correlation between two independently refined half-maps (**figure 17a**). In the average, each facet displays six trimeric D13 subunits arranged in a C6 symmetric hexagonal assembly with an outer diameter of 22 nm and an inner diameter of 7 nm. The contacts to neighboring lattice facets are still visible but blur out quickly with increasing distance from the particle center, highlighting the absence of long-range symmetry in the lattice (**figure 17b, c**). Additional slices through the average volume are shown in **figure S2**.

At the given resolution, the crystal structure of the D13 trimer (J.-K. Hyun et al., 2011) (**figure 17d**) can be readily fitted into the SVA map as a rigid body (**figure 17e, f**). The trimers have a hollow center enclosed in the central region by the two jelly roll domains (J1, J2) of each D13 molecule and capped by the protruding head domains. Except for some basal parts of J2 (**figure 17f**), all domains are well aligned and therefore show strong electron density in the average volume. This includes the D13 head domains and the interfaces between the head domains of neighboring trimers (**figure 17 e, f, g**). This indicates that all inter-trimer interfaces within the hexagonal assembly are equivalent, in contrast to previously proposed models derived from *in vitro* data of artificial helical D13 assemblies (J. Hyun et al., 2022).

However, the connection between the D13 scaffold and the viral membrane does not align in the averaging process and is therefore missing from the average structure. This connection is presumed to be mediated by a direct interaction between the viral transmembrane protein A17 and the central opening in the membrane-proximal base of each D13 trimer (Garriga et al., 2018). This suggests that the A17 linker has some flexibility, thus precluding alignment of this feature which also has a low intrinsic electron density due to its small size.

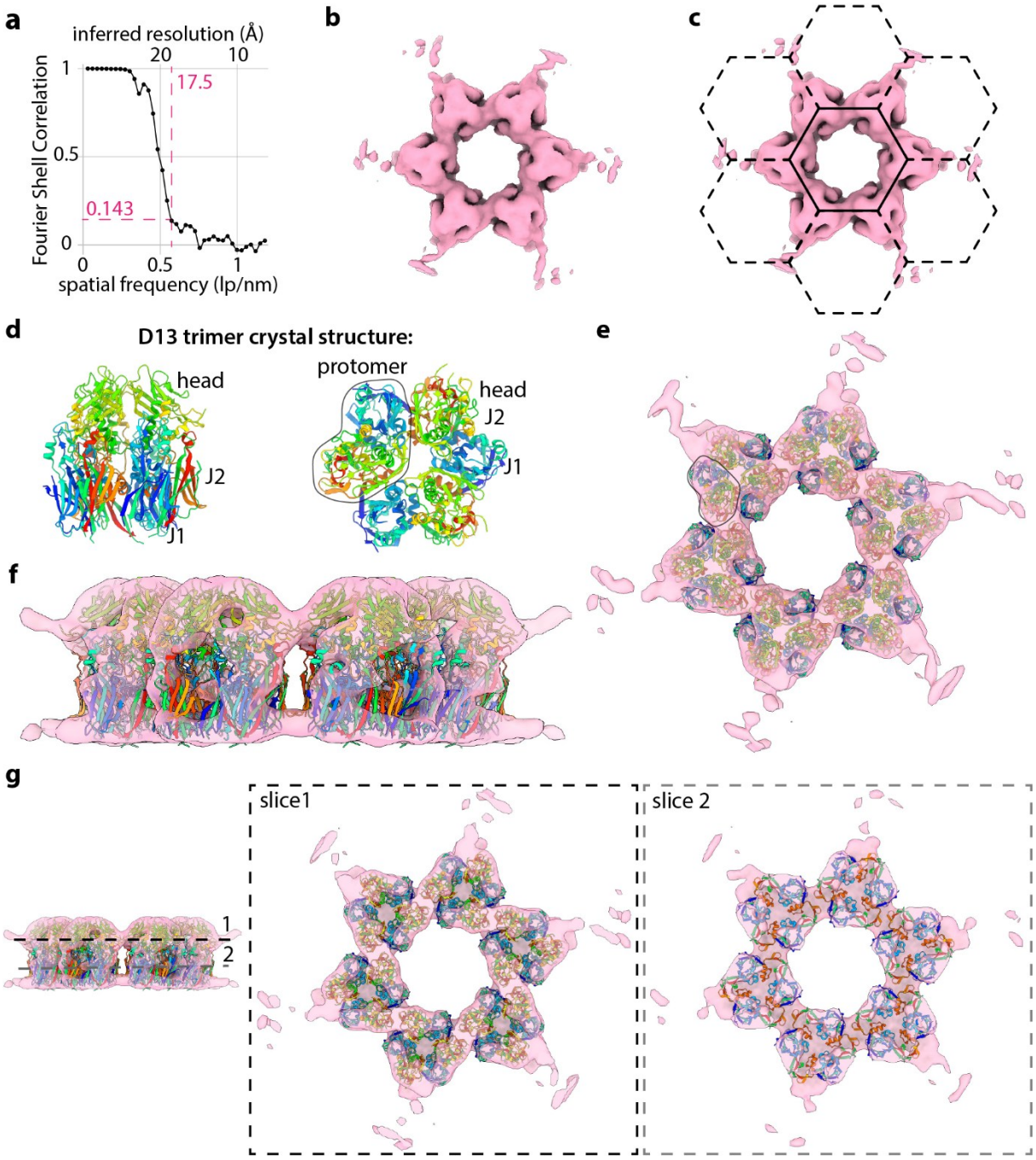

Figure 17: Average structure of the hexagonal D13 assembly from the native in situ lattice of the immature vaccinia virus scaffold: Displayed is the average volume resulting from subvolume averaging of 4900 D13 hexamer particles from four tomograms (F043, M023, M2_027, M2_028), split into two independent half-sets, C6- symmetrized (29400 particles after C6), aligned at a pixel size of 4.242 Å/pix and filtered to a resolution of 17.5 Å with B-factor sharpening (b,c,e,f,g). a): Fourier Shell Correlation between the two half-maps and resolution determined at 0.143 threshold. In c), the central hexagon is indicated in solid black. The connections to the neighboring hexagons in the lattice (indicated by dashed lines) are blurred out due to a lack of long-range symmetry and the heterogeneity within the lattice. Panel d) shows the crystal structure of the D13 trimer (pdb 3saq) in side- and top views with a single protomer outlined in black. The three domains of each protomer, namely J1, J2 and the head domain on top of J2 are also indicated. e) and f) show a rigid body fit of the D13 trimer model (d) into the average volume of a hexamer of trimers viewed from the top (e) and the side (f). All trimeric subunits are equivalent and contact each other via the head and J2 domains. Panel g) shows sliced views of the map-to-model fit as indicated in the left panel.

3.5.4 SVA-based modelling of the D13 lattice

The obtained subvolume average allows for a clearer reconstruction of the virion-spanning lattice than volume-based segmentations as shown in **figure 14**. Plotting back the un-symmetrized bin4 average hexagonal facet volume into the tomogram coordinate system based on the particle coordinates and orientations yields a three-dimensional representation of the D13 lattice that covers large parts of the viral surface (**figure 18**). The observed interlocking of neighboring facets with good superposition of their shared subunits is indicative of good particle alignment and gives license to the applied SVA strategy. Even facets that were not included in the particle set used for the plotback are visualized in the resulting lattice as they can be defined by their neighbors, contributing their respective subunits. This is made particularly clear by the emergence of pentagonal and heptagonal facets in the plotback lattice (**figure 18b, c**).

Importantly, plotback of the essentially flat SVA reconstruction of the hexagonal facet nevertheless results in patches of smoothly curved honeycomb lattices in which the hexagonal facets interlace and are slightly tilted towards each other. While heptameric and pentameric facets might be responsible for accommodating lattice curvature in defect lines, there must be some flexibility within each hexagonal assembly too. Understanding the extent to which there is deviation from perfect hexagonal structures and whether the average obtained only corresponds to an approximation of pseudo-C6 symmetry will require further investigation.

One limitation of this representation is that it suggests holes in the lattice in those areas where D13 particles were excluded from the average due to low cross-correlation. Most prominently, this affects areas where the viral membrane lies flat in the image plane tomogram and is therefore most severely affected by the missing wedge. Consequently, D13 top views were excluded disproportionately in cross-correlation-based particle cleaning when the membrane density was included in the alignment mask. This problem can be partially mitigated by changing the initial spherical to a cylindrical mask that does not include any membrane density and focusses only on the D13 layer above. Other apparent holes in this representation are biologically meaningful, i.e. represent true lattice defects, as they arise from facets with alternative symmetries and therefore do not correlate well with the hexagonal reference.

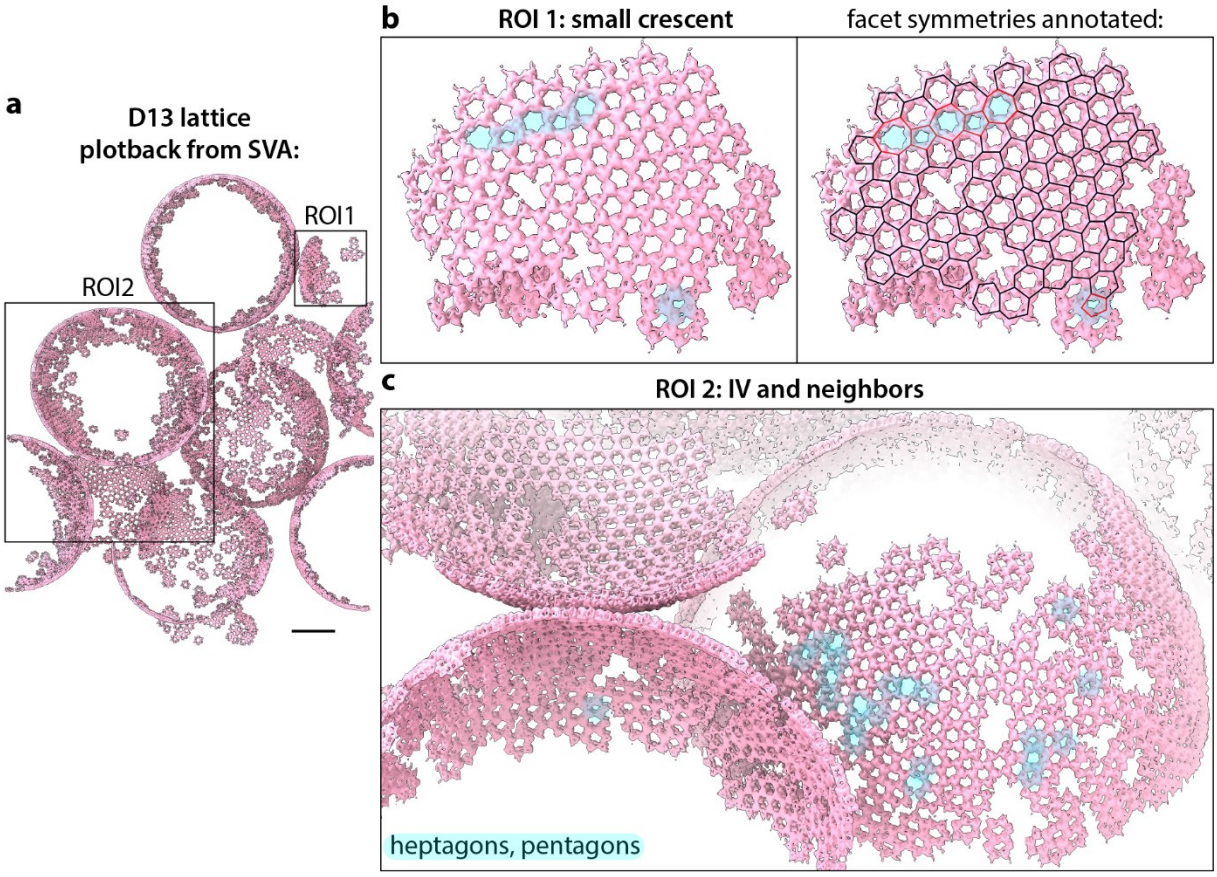

Figure 18: Symmetric patches and defect lines in the VACV scaffold lattice as modeled by subvolume averaging: In panel a), the average volume of the D13 hexagon facet obtained through SVA is plotted back into the original coordinate system of tomogram F043 based on the positions and orientations of the aligned D13 particles contributing to the average. Areas where D13 particles were not sampled or removed from the average due to poor cross correlation appear as holes in this representation of the lattice. Panels b) and c) show detailed views of the modelled lattice in the two ROIs indicated in a). b): In the right panel, the predominant hexagonal facet geometries of the symmetric patch are annotated by black hexagons while symmetry defects are annotated with the corresponding polygons in red. These alternative symmetries are not directly sampled as D13 particles here but are defined by their neighboring hexagonal facets contributing five or seven D13 trimer subunits for a pentagonal or heptagonal facet, respectively. In the left panel of b) and in c), these alternative facet symmetries and the defect lines they form are highlighted in blue.

3.6 Maturation

The D13 protein scaffold and the spherical shape of the viral membrane are distinct defining features of the immature VACV particle that are absent from the infectious mature virion. The process of maturation brings about dramatic changes in the virion morphology, including the removal of the D13 scaffold, the formation of an intricate core structure with associated lateral bodies and a change in overall shape from spherical to brick-shaped (L. Liu et al., 2014). Clearly, the underlying molecular mechanisms must be tightly regulated and most likely encompass a complex, multi-step process. While phosphorylation events and two-step proteolytic cleavage are known to play a role in VACV maturation, intermediates were rarely reported in previous studies. In my dataset of A3-YFP VACV-infected HeLa cells, I observe a subset of viral particles that appear to have an intermediate morphology between the IVs and MVs. I therefore propose these observations capture steps of the maturation process. They are often, although not exclusively, found clustering together with MVs in the perinuclear region, as described in chapter 3.2.

Compared to the crescents, IVs and MVs, these putative intermediate particles are very rare events and appear in approximately 10 % of my tomograms in the A3-YFP dataset. In the wild-type dataset, analogous intermediates are also observed (see **figure S1**), giving license to initially use A3-YFP virus as a model system to study maturation. Due to the low frequency of occurrence of such intermediates, the description and analysis in this chapter is based on observations from the more extensive A3-YFP dataset. The individual intermediate particles observed can be divided into three four with an inferred temporal progression of the proposed dynamic maturation process illustrated in **figure 19**.

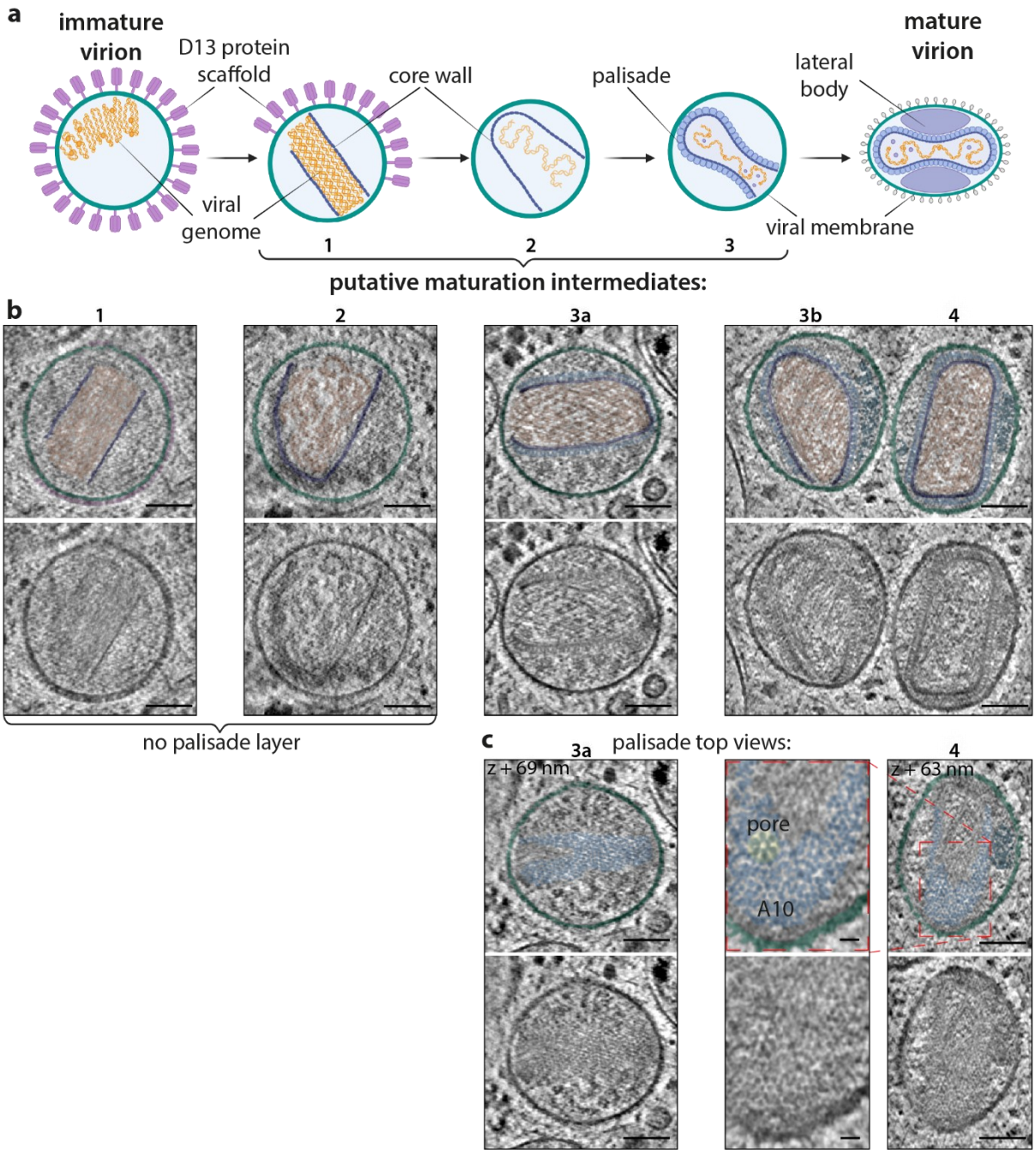

Figure 19: Possible intermediates of maturation: Panel a) presents a model of viral particle maturation from IV to MV based on particles with intermediate morphologies observed here. b): Representative viral particles, corresponding to the 3 types of intermediates and MV sketched in a), are displayed in slices from tomograms M2_047 (1), M022 (2), M2_031 (3a) and M009 (3b, 4). Panel c) shows top views of the palisade layer of the forming core of particles 3a and 4 in tomographic slices 69 nm and 63 nm above the ones shown in b). The middle panel shows a magnification of the boxed region in the right panel. The A10 trimers forming the palisade appear as dots in the top views, next to a flower-shaped core portal highlighted in yellow. The partial D13 scaffold is only present early on (b1, pink) and the core wall (purple) appears to grow during maturation. The core palisade (light blue) on top of the core wall is only present in later stages (3, 4). Putative genome densities (orange) appear striated in 1 and more loosely organized in 2-4. The viral membrane (green) is spherical in the beginning and assumes a more ovoid shape at late stages. Lateral body densities of late intermediates (3) and MV (4) are shown in dark blue. The scale bar in the middle panel of c) represents 20 nm, all others 100 nm.

The first intermediate (**1** in **figure 19**), most closely resembling the IV morphology, still has a completely spherical membrane. However, it is only partially covered by the D13 lattice. On parts of its surface, the lattice has already disassembled, suggesting the onset of the proteolytic cleavage of the A17 linker by the viral protease I7 (Bisht et al., 2009). On the inside of this particle, the genome is not compacted as a nucleoid like those found in IVs, but instead, a different internal structure is beginning to form. At this stage, it is characterized by a brick-shaped, striped density spanning the length of the particle. It is delineated by a more electron-dense layer on the long sides. These structures resemble the filamentous inner layer and the dense core wall, respectively, as observed by cryoET on intact VACV cores (J. Liu et al., 2024). I interpret this to be an early intermediate of viral core formation, where the internal striations/fine filaments are formed by the viral DNA which is being encased in a proteinaceous core structure. The dense layer (4- 5 nm thickness) on the edge of this forming structure would be an early stage of the viral core wall that is supposedly formed by the viral protein A3 (Datler et al., 2024; Moussatche & Condit, 2015). From what is observed here, it seems that the long edges of the core wall form first and the short ends get closed later. Further, this intermediate structure indicates that the disassembly of the D13 lattice and the onset of core formation appear simultaneously, or at least have a temporal overlap, rather than being entirely sequential.

The second type of putative maturation intermediates (**2** in **figure 19**) is already devoid of any D13 lattice as far as it can be assessed here. However, it still retains the perfectly spherical shape and dimensions of the IV, marking it as the logical successor of intermediate **1**. The putative core wall is still not covered by a palisade layer as it would be in the mature core. While the core wall is not completely closed, only one opening on one side remains, resulting in a cup-like shape of the forming core structure. The inner layer, presumably the viral genome and associated proteins, has changed organization. Instead of a finely striated layer, the genome appears as irregular, condensed densities that are loosely connected. Notably, a mixture of both of these arrangements has been reported in purified mature cores observed *in vitro* (J. Liu et al., 2024). This suggests that in the process of maturation, the viral genome first serves as a scaffold for the formation of the core wall and is later relaxed to form locally condensed regions that are loosely connected while some of the genome remains associated to the inside of the core wall.

The proposed third intermediate of maturation is the one most frequently observed (**3** in **figure 19**). The viral membrane is still largely spherical but begins to show deformations. The core structure is still not closed and retains its cup-shaped form. In contrast to the previous state, it is now covered with the palisade layer composed of protein A10 trimers that appear like spikes on the surface of the core wall (Datler et al., 2024; J. Liu et al., 2024). This reveals that the palisade

layer can assemble before the closure of the core wall. Top views of the palisade layer show the expected dotted appearance (**figure 19c**). Interestingly, the sites of most prominent membrane deformations seem to coincide with the opening of the core structure where the inner leaflet of the viral membrane comes closest to the core. A comparison of intermediates **3a** and **3b** in **figure 19b** illustrates that particles with smaller remaining core openings tend to show stronger deviations from a spherical membrane shape. This suggests a correlation between core closure and the adoption of a brick-like membrane shape as found in MVs.

The final stage of maturation observed in this dataset is represented by particles that closely resemble the morphology of a fully mature virion (**4** in **figure 19**). They have a brick-shaped membrane that is in tight contact with the palisade layer of the core at the short ends of the virion. As one of the final steps of maturation, dense lateral bodies have formed between the membrane and the core. The core structure itself is complete with a closed core wall and palisade layer, and core portal structures are now visible. For comparison, additional MVs found in my datasets are depicted in **figure S3**.

4. Discussion

4.1 Organization of the Assembly Site in the Cell

Vaccinia virus induces distinct viral factories within the host cell cytoplasm that are visible by fluorescence microscopy. During viral DNA replication, these compartments have a dense, spherical appearance indicative of phase separation. Indeed, recent studies on the viral factory of the related giant virus mimivirus showed that the viral factory is a biomolecular condensate formed through liquid-liquid phase separation and propose that this is the case for all *Nucleocytoviricota* (Rigou et al., 2024). In the case of orthopoxviruses, which include VACV, the viral protein H5 was predicted as a scaffold protein inducing this process. This segregation of viral content from the cytoplasm is considered favorable for the virus to streamline biochemical reactions within a defined compartment (Glon et al., 2024). It might further shield the viral extranuclear DNA and avoid detection by the innate immune system.

At later post-replication stages of the viral cycle, the viral factory becomes the site of progeny virion assembly. This is observed here in fluoresce microscopy through the appearance of the viral core protein A3 in the factory. Interestingly, at these later stages, the viral factory loses its distinct, condensed spherical morphology and appears more diffuse, with an extended and uneven shape. In cryoET, these late viral factories, or assembly sites, are clearly distinct from the surrounding cytoplasm. Reminiscent of a phase-separated condensate, they show an exclusion of cytoplasmic material and characteristic background granularity, but no clear delineating structure (**figure 7**). However, this exclusion is not complete. Some ribosomes are found within the assembly site, albeit less frequently than in the surrounding cytoplasm. Cytoskeletal elements, most prominently microtubules, and organelles like mitochondria and ER-cisternae can be observed infiltrating the segregated area of the viral assembly site. It is possible that the viral factory progressively loses the characteristics of a biomolecular condensate after viral DNA replication, as progeny virion assembly and their exit from the assembly site might require a higher degree of material exchange with the surrounding cytoplasm. This could be further investigated by fluorescence recovery after photobleaching (FRAP) experiments that quantitatively compare the behavior of assembly sites at 8 hpi with earlier viral factories at the replication stage (Vallbracht et al., 2025).

A previous study proposed that the viral assembly site is surrounded by tubular membrane cisternae of the ER-Golgi intermediate compartment (ERGIC) and a protective cage of vimentin filaments (Risco et al., 2002; S. Zhao et al., 2024). Such tubular membranes, that are likely to be ERGIC cisternae, are also found at the edge of viral assembly sites in my tomograms. However,

the cytoskeletal filaments I observe at the edge of the assembly site do not appear to form a dense cage. Furthermore, their morphology and thickness indicate that these filaments are predominantly actin (Tsuji et al., 2024; Vallbracht et al., 2025). Thicker intermediate filaments, which could be vimentin, are occasionally observed in my data, but do not provide evidence for a vimentin cage.

The lamella-based cryoET approach employed here provides detailed information at a high spatial resolution, allowing analysis of individual viral particles at the molecular level. The contextual information, however, is limited by the size of the lamella, which only provides access to a fraction of the cellular volume in x, y, and most dramatically z. One consequence of this is that immature virions, which have a diameter of 350 nm, are always cut during the milling process and not fully contained within lamellae. This often prevents the distinction between IVs and open crescents and thus hinders quantification of viral assembly intermediates. Further, the amount of cellular context information accessible within any given lamella depends entirely on the positioning of that lamella in the cell. Volume-imaging with a serial slice-and-view approach in a FIB-SEM system is a promising approach to complement the data presented here with a less high-resolution, but complete characterization of the assembly site and its context in the whole cell volume (E. R. Quemin et al., 2019). The analysis of the large volumes of image data generated by this technique will be greatly facilitated by semi-automatic segmentation approaches such as the one I have established for my cryoET data.

The lamella overview TEM data presented here show that there is a separation of assembly intermediates and mature virions which localize to different sites inside the infected cell. This is in agreement with earlier descriptions of intracellular transport of assembled virions, which appears to be dependent on microtubules (Ward, 2005). Interestingly, microtubules are observed in high-magnification tomograms, both in the assembly site in the vicinity of immature virions, and next to mature virions in the perinuclear area. A detailed analysis of these events might reveal motor proteins connecting virions to microtubules to enable transport through the cell. The observation of viral particles that seem to be in intermediate stages of maturation and are localized to the perinuclear cluster of mature virions indicates that intracellular transport is not selective for fully mature viral particles. Furthermore, this implies that virion maturation is not completed within the viral assembly site as previously suggested (L. Liu et al., 2014).

For most of the experimental work, the inaccessibility of wild-type VACV in cryo-lamellae limited the analysis presented here to cells infected with the labelled A3-YFP virus. The structural protein A3 is the major component of the VACV core wall, hence the introduction of the label is unlikely to interfere with the process of IV membrane acquisition. However, care must be taken when

particle maturation is studied in this system, particularly the formation of the core wall. The fluorescence-based comparison between A3-YFP- and wild-type virus-infected cells demonstrates that the introduction of the label does not alter the overall characteristics of the viral assembly site and the progression of the infection cycle. A preliminary comparison between the A3-YFP dataset and wild-type tomograms, that were finally obtained after successful optimization of the sample preparation workflow, confirms the conclusions drawn from the A3-YFP dataset. With wild-type VACV now being accessible for cellular cryoET as well, a more detailed analysis of maturation intermediates will provide further insights into the assembly of the native, unlabeled core structure, including subvolume averaging approaches.

4.2 Viral Membrane Formation

The mechanism of poxviral IV membrane acquisition differs fundamentally from the strategies employed by most enveloped viruses. Most commonly, membranes are acquired by exploiting or mimicking cellular membrane remodeling pathways like vesicle budding, membrane fission and fusion or the formation of double-membrane compartments through wrapping in cisternae (Motsa & Stahelin, 2021; Schauflinger et al., 2013). Membrane acquisition via the formation of ruptured, open-ended membrane structures seems to be a mechanism unique to the phylum *Nucleocytoviricota*, which includes poxviruses (Rodrigues et al., 2021). This mechanism poses a distinctive challenge. At the open membrane ends, a delicate balance must be found between shielding the hydrophobic interior of the lipid bilayer from the hydrophilic environment and enabling membrane fusion for crescent growth. How exactly this is achieved remains one of the principal open questions in the field of poxvirus research.

From immuno-gold labelling of viral crescents in VACV-infected cells, it seems that some of the viral membrane assembly proteins (VMAPs), small viral proteins that are essential for the rupture of the precursor membranes and thus crescent and IV formation, occupy the open ends of the ruptured membranes to prevent re-sealing and stabilize the open ends of crescents. Specifically, localization to the open membrane ends of crescents has been suggested for the VMAPs A11, L2 and inferred for A30.5, which interacts with L2 (Maruri-Avidal et al., 2011, 2013a, 2013b). The largest VMAP, A6 is not directly membrane-bound, but there is some evidence for a protein-protein interaction with A11 which could recruit this protein to the crescent edge as well (X. Wu et al., 2012). One hypothesis is that these VMAPs form a complex at the open crescent ends to induce membrane rupture. After rupture, such a complex could stabilize the open membrane edges and regulate fine-tuned crescent membrane growth (Moss, 2015; Pathak et al., 2018). In this work, no such complex was observed at the open ends of crescents. However, considering the size limitations that apply to cellular cryoET, only a large complex of at least 100 kDa in size

could have possibly been detected (Russo et al., 2022). Given the small size of the involved VMAPS (L2: 10 kDa, A30.5: 4.8 kDa, A11: 36 kDa and A6: 43 kDa) (Moss, 2015), it is conceivable that they form a partially membrane-embedded complex that is too small or irregular to be visible in my cellular cryoET data.

In the context of extensive prior studies on poxvirus membrane assembly in infected cells, (Chlanda et al., 2009; Suárez et al., 2013; Weisberg et al., 2017), the data presented here provides a detailed perspective on viral assembly intermediates preserved in a near-native state, substantiating the current assembly model. The observation of ER cisternae in the immediate neighborhood of viral assembly sites supports the hypothesis that the viral membrane is derived from the host cellular ER. Crescents form through the association of ruptured, ER-derived membranes with the viral scaffold protein D13 that imposes a characteristic curvature. The observation of curling crescent ends, where the membrane is not covered with D13, aligns with the hypothesis that crescents grow continuously through the piecewise incorporation of new membrane material from a pool of ruptured vesicles found in the assembly site. This is further supported by the comparable size and curvedness of curling viral crescent membrane ends and the vesicles and opened membranes found in direct proximity. The curvature between the precursor membranes and the scaffolded virion membrane is inverted because D13 does not bind directly to the membrane but interacts with the N-terminal domain of the viral transmembrane protein A17 (Garriga et al., 2018). A17 is synthesized into the host cell ER membrane with the N-terminal domain on the luminal side which becomes exposed and accessible to D13 in the assembly site through membrane rupture. The D13 scaffold then inverts the curvature, turning the ER-derived membrane inside-out, thus rendering the previously ER-luminal membrane leaflet the outer leaflet of the viral membrane. Crescent edges that are not yet covered by D13 retain the original curvature and therefore appear to be curling in the opposite direction compared to the scaffolded crescent membrane. Notably, this inversion of the ER-derived membrane by D13 is required to position the ER-luminal domains of membrane-resident viral glycoproteins on the outer surface of the nascent virion. This membrane orientation, whereby the cytoplasmic membrane leaflet of the cellular origin membrane becomes the inner leaflet of the virion membrane constitutes a unifying principle among all enveloped viruses.

Having access to the viral membrane in a vitrified, near-native sample allows a detailed analysis of membrane properties such as local curvature, revealing distinct features of the viral and surrounding cellular membranes (**figure 13**). Slight wave-like local curvature variations are observed in some areas of low overall curvature of the ER membrane in my data and also apparent in comparable analyses of mitochondrial and Golgi membranes (Barad et al., 2023;

Boneš et al., 2024; Salfer et al., 2020). However, the membranes of viral crescents and immature virions observed here consistently show a pronounced waviness as apparent from ripples in the local membrane curvedness. These are more distinct than in surrounding cellular membranes and seem to be an inherent feature of the viral membrane. Notably, these ripples are absent from crescent membrane curls which are not covered by the D13 lattice. These curling ends, in contrast, share the more highly curved, but smooth appearance of small vesicles and open-ended precursor membranes found in the surrounding. It is therefore tempting to speculate that the ripple-like local membrane curvature variations of the IV and crescent membranes are induced by the viral D13 scaffold. To test if there is a correlation between the regions of higher local membrane curvature and the lattice defect lines, a direct superposition of the D13 lattice facet geometries and the membrane polygon mesh is desirable. In the absence of a suitable superposition method with the currently available representations of the D13 lattice, only a preliminary comparison of corresponding surfaces can be made. Based on this, it appears that the symmetric hexagonal patches observed in the D13 lattice tend to be larger than the local areas of generally low curvature observed on the membrane. This suggests that hexagonal patches of the D13 lattice can induce local variability in the membrane curvature, as well. This could be explained by flexibility within the hexagonal lattice facets.

The local membrane curvedness analysis performed here on a small dataset demonstrates that this type of analysis is well suited for segmented VACV IV and crescent membranes from cryoET data. It is therefore promising to pursue this type of analysis on a larger dataset, enabling the statistical analysis of measured parameters. The calculation of local membrane properties relies on a polygon mesh representation of the membrane. As an alternative to the screened Poisson algorithm used here for the conversion of binary membrane segmentation masks into such polygon meshes, it could be beneficial to use an improved method for membrane polygon mesh modeling based on mid-surface extraction (Boneš et al., 2024). The surface morphometrics toolkit offers more possibilities for analysis, but requires additional custom scripting (Barad et al., 2023). The distances and orientations between different types of membrane classes, e.g. between curling crescent edges and the surrounding vesicles, are worth exploring. Most prominently, it will be interesting to correlate the local membrane curvedness with the geometry of the D13 lattice. This analysis is feasible with the surface morphometrics toolkit, as soon as a successful classification of hexagonal, pentagonal and heptagonal D13 lattice facets is achieved so that they can be treated as different classes for membrane – D13 distance measurements.

4.3 The Scaffold Protein D13

4.3.1 Lattice and defect lines

Spherical viral lattices have been observed across viral families and their organizational principles vary widely. While hexagonal lattice facets are fundamental components, they alone cannot form spheres. Consequently, different viral strategies have evolved to form imperfect hexagonal lattices on curved surfaces. In spherical, immature HIV particles, the lattice is strictly hexagonal, but covers only part of the surface and is complemented by vacancy defects (Schur et al., 2015; Tan et al., 2021). The spherical lattice formed by the herpesvirus nuclear egress complex (NEC), on the other hand, appears to have densities in non-hexagonal regions, suggesting disordered patches of the lattice (Pražák et al., 2024). Notably, both HIV Gag and herpesvirus NEC scaffold the membrane from the inside, whereas VACV D13 does so from the outside.

As apparent from my data, the D13 lattice on the immature VACV membrane forms a continuous honeycomb-like lattice with primarily hexagonal lattice facets that includes symmetry breaks by incorporating alternative facet geometries. No holes in the lattice could be observed. Even though this lattice lacks icosahedral symmetry, the principles for the formation of continuous, closed lattices described for icosahedral capsids can be useful here. In principle, the introduction of 12 pentameric symmetry defects would suffice to convert a flat, entirely hexagonal lattice into a closed shape, which is the case for icosahedral viral capsids approximating a sphere or the cone-shaped fullerene-core of the mature HIV capsid (Twarock & Luque, 2019; G. Zhao et al., 2013). In the D13 lattice, however, pentagonal symmetry defects are observed more frequently than this and are accompanied by heptagonal facets as well. Furthermore, they are not found in regular positions, but form strings of non-hexagonal facets in defect lines. These scar-like symmetry defects are predicted by the Thomson problem theory and relieve the high topological tension that an isolated pentagonal symmetry defect would have in a large spherical assembly (Bausch et al., 2003). Their observation in the curved D13 lattice is in good agreement with the defect lines found in colloidal particle systems and that were predicted for sufficiently large viral capsids. This highlights the overall pleiomorphic nature of the immature poxvirus scaffold, despite the structural homology of D13 to viral double-barrel capsid proteins from e.g. adenoviruses which form perfect icosahedral assemblies (J.-K. Hyun et al., 2011).

Local defects in the D13 lattice have been observed previously by deep-etch EM on top views of the immature virion surface in cryo-sections of high pressure-frozen samples (Heuser, 2005; Szajner et al., 2005). My data confirm these earlier observations and show that symmetry breaks are arranged as defect lines spanning the curved virion surface. Heptagons and pentagons are

adjacent to each other and clusters of heptagonal and pentagonal facets form elongated stretches at the edges of more regularly hexagonally ordered patches. With the advanced technology of cellular cryoET, I now have access not only to a stereo-image of the lattice top view, but to the 3D volume of the whole lattice as it is contained within a cryo-lamella in a native, frozen-hydrated state. Importantly, by preserving the native state of the virion in the cryoET workflow, a correlation of membrane and lattice properties becomes feasible.

In order to achieve a quantitative, whole virion representation of the lattice and its different facet arrangements, different computational avenues established in this work can be followed. Obtaining such a holistic model of the lattice will open new avenues for thorough statistical analysis of lattice properties such as the size and shape of symmetric patches and defect lines, respectively, and the relative abundance of facet geometries. These are key to a deeper understanding of the lattice assembly process through mathematical modelling of the underlying local rules.

One approach to model the lattice applied here is the tracing of D13 densities across the accessible viral surface in the tomogram using a segmentation approach. This proved suitable for visualization and manual annotation of facet geometries as shown in **figure 14**. In principle, the skeletons of these segmentations can be used to generate a network representation of the lattice where the D13 trimers are represented as nodes and the inter-trimer connections as edges of a graph. The advantage of a segmentation-based lattice representation is that it covers the entire accessible surface and also closely represents the ground truth of the electron density in the original tomographic data, with no assumed idealizations. The disadvantage is that it is corrupted by noise and the anisotropic resolution inherent to tomography and is therefore not equally interpretable throughout the whole volume. The use of morphological operations applied to segmentations such as smoothing and mask erosion prior to skeletonization might mitigate some of these problems.

The alternative approach employed here for 3D modelling of the D13 lattice uses the refined D13 hexamer positions and orientations determined by subvolume averaging (**figure 18**). As this workflow was focused on the hexagonal D13 lattice facet, the positions of pentagonal and heptagonal facets are excluded during the SVA process and not directly included in this set of facet coordinates. Their locations, however, are often implied through their neighboring facets contributing the relevant subunits. Based on this set of particles, a shift of the defined particle position from the center of each (hexagonal) lattice facet towards its six trimeric D13 subunits and focusing the alignment on these can provide a set of particle coordinates that include the subunits belonging to all different facet geometries. Such a set of D13 trimer coordinates in 3D

space can be used to build an interaction network representation of the lattice by connecting each subunit node to its two nearest neighbors. From this, the tiling of the lattice can be interpreted (Fatehi & Twarock, 2023). While a complete sampling and alignment of D13 trimers across the lattice by SVA would be ideal to obtain the desired network representation, the relatively small size of the trimer and the connections to neighboring particles will pose challenges during particle picking and alignment that must be overcome with a careful masking strategy and likely a limitation in rotational freedom during particle alignment. If successful, an alignment focusing on the trimers might also be able to resolve the flexible connection between the D13 trimer and the membrane-embedded A17.

Complementarily, and in keeping with my original particle definition for SVA as one lattice facet, a classification-based approach can provide a facet-based model of the lattice. In a strategy similar to the one applied to identify incomplete hexamers of the HIV Gag lattice (Tan et al., 2021), pentagonal and heptagonal D13 lattice facets should be distinguishable from hexagonal ones by principle component analysis as well as volume-based classification. This approach has the advantage that it offers not only access to the coordinates of pentagonal and heptagonal facets for the description of the lattice properties, but also the average structures of such facets, provided a sufficiently large number of the respective particles.

For classification, in general, a large input dataset is required to compensate for the effects of noise and the missing wedge. For this, the set of fine-aligned tomograms as a basis for particle picking will be extended. With UPICK-v2, particle picking is automated and no longer a time-limiting factor. However, as UPICK was trained on hexagonal facets, caution must be taken to include the non-hexagonal facets in the dataset destined for classification. Facets not sampled by UPICK will therefore be recuperated from the aligned positions of their neighbors through symmetry expansion. Subsequent particle cleaning will rely less strictly on cross correlation with a hexagonal reference. This comes at the expense of blurring the overall average structure as facet heterogeneity as well as non-excluded ill-aligning particles will contribute noise. Truly ill-aligning particles can be removed later during the classification by sorting them into a junk class. To avoid the disproportionate exclusion of D13 top views during cross correlation-based cleaning, the membrane density will be masked out during alignment by using a cylindrical mask.

4.3.2 The hexagonal lattice facet

The average structure of the hexagonal D13 lattice facet obtained *in situ* at a resolution of 17.5 Å shows clear head-to-head domain contacts between trimers. This allows me to propose a model for the hexagonal arrangement that is different from models proposed previously based on *in vitro* data (J.-K. Hyun et al., 2011; J. Hyun et al., 2022).

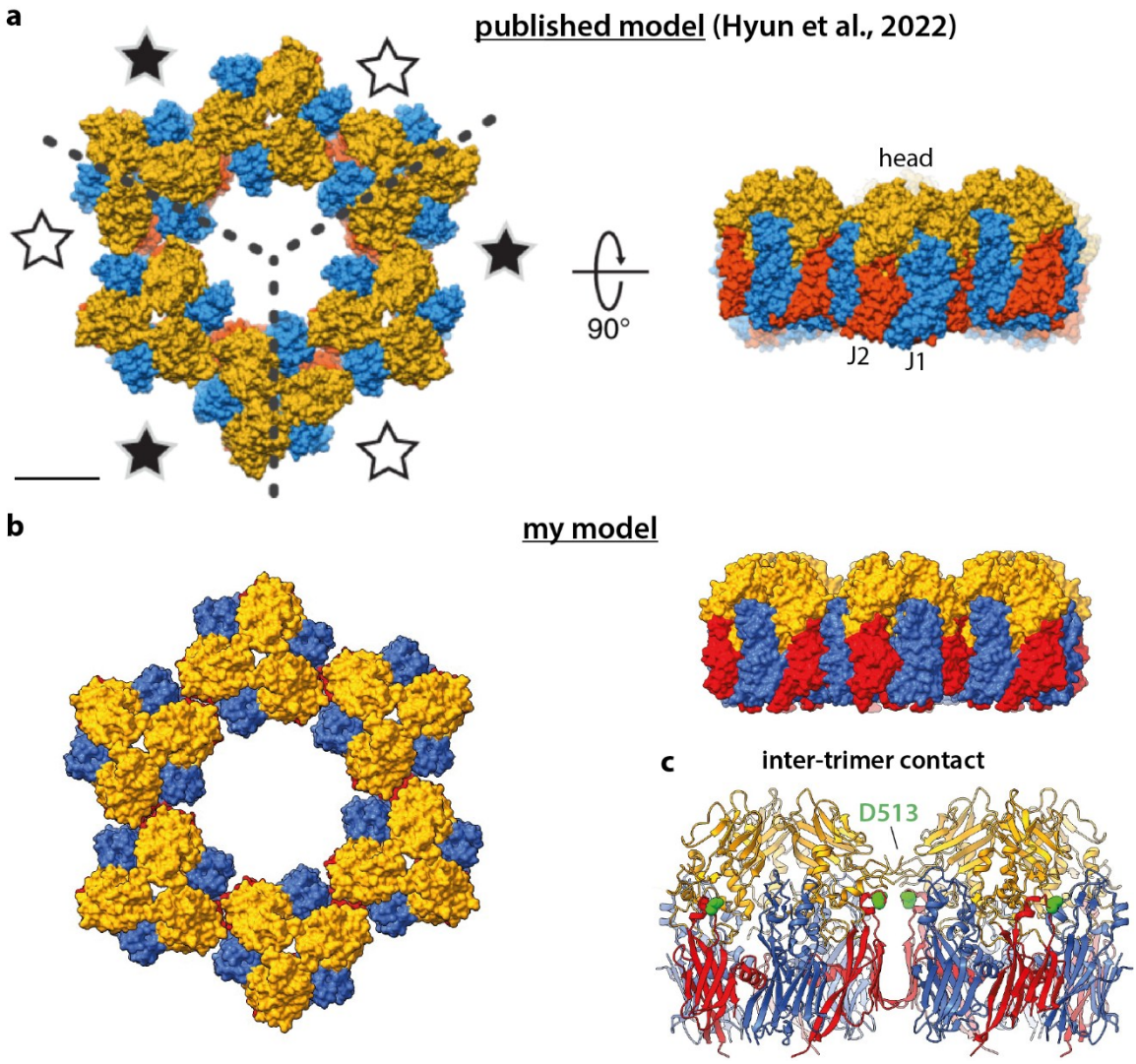

Figure 20: Comparison of models proposed for the hexagonal D13 lattice assembly: a): In the model previously proposed by Hyun et al. there is no hexagonal symmetry within the hexamer of D13 trimers. Instead, trimers are tilted, not flat, and connected via two distinct, alternating interfaces (stars). Viewed from the side, this results in a twisted assembly. b): The pseudo-atomic model obtained by docking the D13 trimer crystal structure into my SVA of the *in situ* lattice shows a C6 symmetric, flat arrangement with equivalent D13 trimer positions and inter-trimer contacts. These contacts (c), mediated by the head domains, involve residue D513 which was previously shown to be crucial for the formation of spherical lattices (Szajner et al., 2005). Panel a) is modified from J. Hyun et al., 2022 under the Creative Commons Attribution 4.0 International License. J1, J2 and head domains are shown in blue, red and orange.

Hyun et al. proposed a model for the assembly of D13 trimers into a hexagonal facet of the curved D13 lattice on the viral membrane (**figure 20a**). This model is based on their *in vitro* studies of N-terminally truncated $D13_{18\text{-}548}$ which self-assembles into spherical and tubular structures under low-salt conditions as observed by cryoEM (J. Hyun et al., 2022). A low-resolution structure of the tubular assembly was obtained by helical single particle analysis. This highly curved, tubular lattice is formed by interconnected hexamers of trimers with two distinct modes of inter-trimer contacts that result in a kink of each lattice facet along its two-fold symmetry axis. Based on these findings, the authors modelled a hypothetical, C3-symmetric arrangement of six D13 trimers that

would allow to accommodate spherical lattice curvature, employing the two modes of inter-trimer contacts in an alternating fashion. In this model, the axes of the individual trimers are tilted with regard to each other, positioning their head domains in different planes and resulting in an overall warping of the hexagon. The existence of these different contact modes and trimer torsions certainly demonstrates the ability of the D13 protein to accommodate various arrangements and speaks to an inherent flexibility of the D13 lattice. However, and especially considering the apparent variability of assemblies formed by D13 *in vitro* under different experimental conditions, these models may not accurately describe the biologically relevant arrangement of the lattice on the viral surface. In the model based on the *in situ* average obtained here, I observe head-to-head domain contacts between trimers that are consistent throughout the hexagonal assembly and not alternating (**figure 20b**). All subunits appear equivalent and in the same plane, forming a flat, C6 symmetric hexagon. Notably, the C6 symmetry during refinement was only imposed after the symmetric structure became apparent from C1 alignment.

Intriguingly, the inter-trimer interface with head-to-head domain contacts observed in my average contains the residue D513 which is located at the junction between the head and J2 domains of D13 (**figure 20c**). Mutation of this residue to glycine has been shown to have a dramatic effect on the self-assembly properties of D13 in infected cells, inducing a shift from the functional spherical lattice that is found on the surface of immature virions to large, flat 2D lattices composed entirely of hexagonal facets (Szajner et al., 2005). This suggests that the corresponding loop plays a crucial role in the ability of D13 to form the different facets of the curved viral lattice as opposed to flat, strictly hexagonal assemblies, presumably conferring some flexibility at the inter-trimer interface. The fact that this crucial region of the D13 protein is located at the interface described here further supports my model for the hexagonal assembly of D13 in the curved viral lattice. Complementarily, a model obtained from 2D crystallography of a flat, perfectly hexagonal D13 lattice *in vitro* proposed an entirely different inter-trimer interface for the flat lattice with contacts between the J1 and J2 domains and no contribution of D513 to the interface (J.-K. Hyun et al., 2011). Taken together, these findings indicate that the D13 protein can form various inter-trimer interfaces which affect the type of lattice that is formed (e.g. tubular, spherical, flat). To produce the curved, spherical lattice found on the surface of the immature poxvirus membrane, an approximately C6-symmetric hexagonal arrangement with head-to-head domain contacts involving residue D513, as it is observed from the *in situ* SVA here, seems to be crucial.

Within the average structure of the hexagonal D13 lattice facet I obtained, some density is missing from the D13 trimers, particularly in the J2 domain. Interestingly, this occurs at the sites of inter-trimer contacts. While these contacts show well-aligned density for the interaction between the

head domains, the density of the J2 domains below is blurred out. This hints at a degree of variability of the inter-trimer contacts in this region, resulting in heterogeneity among the hexagon particles contributing to this average. This could be related to the slight deviations from perfect C6 symmetry within the assembly of six trimers needed for the arrangement of adjacent hexagonal facets on a curved surface. Classification of a large set of well-aligned D13 hexagon particles is a promising avenue to characterize this biologically relevant heterogeneity and resolve the missing densities in the J2 domain.

A comparison of my average structure with the low-resolution SVA of the D13 lattice *in situ* previously published by Hernandez-Gonzalez et al., 2023 highlights two key differences in the experimental and data processing approach. Experimentally, the production of 100- 250 nm thin cellular samples through FIB-milling allowed me to collect data with a more advantageous signal-to-noise ratio and closer to focus when compared to their whole-mount tomography approach in the thin periphery of adherent cells. While this approach has the advantage of containing whole virions within the accessible sample volume, the necessary sample thickness of at least 350 nm contributes noise in TEM imaging and limits the obtainable resolution. In the published SVA structure, C6 symmetry is imposed over a large subvolume box spanning a total of 19 interlacing hexagons. Given the heterogeneity of the D13 lattice, the contribution of non-hexagonal facets within the subvolume likely limits the alignment and results in a blurred average. My processing strategy which focused the alignment strictly on one central hexagon by masking out the neighbor facets allowed a more precise alignment and resulted in an average structure which resolves the D13 hexagon at a higher level of detail thus enabling me to propose a pseudo-atomic model for the hexagonal assembly.

4.4 Genome Condensation and Packaging

After crescent formation, the next step in poxvirus morphogenesis is the incorporation of the viral genome into the immature virus particle, a process that is generally poorly understood for poxviruses and other large nucleocytoplasmic DNA viruses (NCLDVs) (Talbert et al., 2023). Two distinct modes of putative genome packaging are observed here, both showing a structuring of the viral genome into a dense, striated nucleoid (**figure 12**).

While histone-like proteins that bind to DNA and organize it into a condensed structure have been described for some NCLDVs, little is known about genome organization in poxviruses and the current literature consensus is that such proteins are lacking (Greseth & Traktman, 2022; Talbert et al., 2023). Alternatively, low molecular weight polyamines have been proposed to play a role in the dense packing of the poxvirus genome. The highly ordered structure of the viral nucleoid as observed by cryoET here and in another recent study suggest that the genome may indeed be structured as a nucleoprotein complex (Hernandez-Gonzalez et al., 2023). The striated appearance of the genome may be interpreted as a tightly packed DNA filament, looped in an orderly fashion. Further insights into the underlying structure can perhaps be obtained in a dedicated study through filament tracing and subvolume averaging. Even in the absence of a bespoke histone-like DNA-binding protein, the viral DNA might form a regular complex with the viral RNA polymerase and co-factors of the viral transcription machinery required to initiate transcription of early genes independently of the host cell nucleus (Grimm et al., 2022).

The predominant mode of genome incorporation observed here is consistent with a proposed ATPase-dependent packaging mechanism through a dedicated pore (Greseth & Traktman, 2022). Such a mechanism is reminiscent of other dsDNA viruses such as herpesviruses and siphoviruses in which a capsid portal vertex actively translocates naked dsDNA into the pre-assembled viral capsid, thereby simultaneously condensing it (Pajak et al., 2024). In poxviruses, an analogous mechanism has not been identified yet, but the viral DNA-dependent ATPase A32 was shown to be essential for genome incorporation into IVs (Cassetti et al., 1998; Ramakrishnan et al., 2025). A32's high sequence homology with the pore-forming, bacterial DNA translocase FtsK suggests that it might indeed act as a packaging ATPase (Massey et al., 2006; Ramakrishnan et al., 2024). The outer diameter of the reported FtsK pore structure that accommodates one dsDNA molecule matches the 17 nm size of the putative VACV portal density observed here (**figure 12e**). However, a strict reliance on a portal structure in an otherwise closed particle is at odds with my observation of genome filling through larger membrane openings of 30-50 nm. This might be explained by the presence of an already active translocating ATPase A32 at an open

membrane edge well before the complete closure of the membrane. Recruitment of A32 to the open ends of late crescent membranes might be achieved by the interaction with the VMAP A11 which has been reported by co-immunoprecipitation (Resch et al., 2005). A11 has been shown to localize to the open end of crescent membranes using immunogold labelling (Maruri-Avidal et al., 2013a), but direct evidence for complex formation with A32 in crescents is missing.

In herpesviruses, translocated DNA is simultaneously condensed due to the rising pressure in the rigid capsid (Bauer et al., 2015). In poxviruses, which disassemble the external D13 scaffold in the process of maturation, such high pressures cannot be conceivably sustained. Also, in the observed nascent virions with partially open membranes (**figure 12d**), pressure-based condensation of incorporating DNA would be impossible. Yet, condensation of DNA on the inside of these viral particles is clearly visible, arguing for the need of a molecular condensing agent, presumably concentrated in the viral interior.

A remarkably different phenotype is the appearance of structured, already densely packed genomes in transit through significantly larger membrane openings (**figure 12c**). Combined with the observation of equally structured genomes found freely in the viral assembly site (**figure 12b**), this finding offers two possible interpretations. In accordance with previous reports based on conventional EM (Chlanda et al., 2009), this might be a second uptake mechanism of pre-structured genomes, that does not require a portal. In this case, it is unclear how the genome is condensed independently of uptake and how it is later specifically targeted for incorporation into the virion. Alternatively, these observations might relate to aberrant particles losing their already structured nucleoid after portal-based packaging. It is conceivable that a failure to fully seal the membrane or a lack of the otherwise typically observed genome-membrane anchors (**figure 12a, d**) would cause this phenomenon.

4.5 Maturation

My cryoET dataset of A3-YFP VACV-infected cells also yielded a small subset of particles with a morphology intermediate between that of an immature and a mature virion. I interpret these particles as intermediates in the maturation process. While this is certainly one explanation for the observation of these particles, I cannot exclude the possibility that they are instead dead-end products of an arrested maturation process that has run out of material for complete core formation. Such dead-end products of viral assembly could be released as aberrant particles, such as those recently described as "irregularly shaped virions" in a cryoET study of purified monkeypox virus (MPXV) (Hong et al., 2024). Notably, the reported aberrant internal structures of these particles do not correspond to any of the putative maturation intermediates I describe here. In any case, the observed intermediate viral particle morphologies provide valuable information about the hitherto mostly enigmatic process of maturation, particularly the formation of the intricate internal core structure.

Sorting the observed intermediates into a temporal sequence allows me to propose a possible mechanism for the stepwise maturation of the VACV particle with a focus on core assembly (**figure 19**). According to this proposed mechanism, the removal of the D13 scaffold from the IV membrane and the onset of core wall formation have a temporal overlap. A finely striated layer, which could be the viral genome, seems to serve as a scaffold for the assembly of the core wall around it. This inner layer becomes more relaxed and irregular as maturation progresses. The core wall remains open at one side while the palisade layer starts to form on top. Palisade-covered core walls with loosely organized internal densities, probably corresponding to the viral genome, then proceed to progressively close the remaining opening of the core. This coincides with a change in viral membrane shape from spherical to brick-like and the condensation of lateral body densities.

Interestingly, the putative VACV maturation intermediates I observe here are different from the ones described in one recent cryoET-based study (Hernandez-Gonzalez et al., 2023). There, only particles with completely formed, closed viral core structures including the palisade layer have been observed, some retaining parts of the D13 lattice on their roughly spherical envelope. My dataset does not contain any such particles. The intermediates I observe have incomplete core structures and only the earliest one still displays a part of the D13 lattice. A possible explanation for this is that in their study, Hernandez-Gonzales et al. did not employ FIB-milling to thin samples and therefore had access only to the thin, peripheral regions of the cell. In contrast, my analysis was focused on the thicker, cytoplasmic and even perinuclear regions of the cell made

accessible through the milling of lamellae in infected cells. Thus, FIB-milling provides access to the cluster of maturing virions found next to the nucleus. It is possible that the same intermediates with partial core structures I observe were also present in their samples, but inaccessible due to the sample thickness in the respective region.

The analysis presented here is based only on a few observations of individual particles that represent rare events. More data need to be acquired specifically on these intermediate particles and thoroughly analyzed to validate the proposed mechanism. Further, this analysis should be performed on the wild-type virus to ensure a native core architecture that is undisturbed by the YFP-tag on the major core protein A3. With the optimized sample preparation workflow established here, such wild-type data are now available. Importantly, a preliminary analysis of the first WT dataset confirmed the existence of intermediate particles like the ones described here (**figure S1**). Should a specific targeting of the putative perinuclear maturation site for lamella production be required, a cryoCLEM workflow based on alternative tagging strategies with fluorescent labels on viral membrane proteins or those that localize to the lateral bodies can be exploited.

Further, the high spatial resolution offered by cryoET can be harnessed to explore mutant viruses that delay or abrogate the maturation process. Several such phenotypes have been described, among them an uncleavable A17 mutant that prevents the disassembly of the D13 scaffold (Bisht et al., 2009; L. Liu et al., 2014). Such phenotypes might produce a higher number of specific intermediate particles amenable to detailed structural analysis and provide further mechanistic insights.

5. Outlook

A detailed discussion of further analyses and follow-up experiments directly related to the data presented in this thesis is found in the previous chapters.

Cellular cryoET is a powerful technique to access virus-host interactions in high detail at the nm scale. With ongoing advancements like the development of increasingly precise and streamlined cryoCLEM workflows, more contextual biological information becomes available and can be used for the direct targeting even of rare events. Increasing automation of the lamella production and parallelized data acquisition schemes significantly boosts the amount of data that can reasonably be produced (Berger et al., 2023; Eisenstein et al., 2023). Processing and the analysis of such large datasets are arguably now the new limiting factors. While automated batch reconstruction of lamella tomograms is valuable for screening, I find that the best reconstructions achieved in this work were still based on careful manual alignment of tilt series. Automated tilt series alignment still works best for *in vitro* samples with defined gold fiducials that can be robustly detected automatically (Mastronarde & Held, 2017). For lamella samples, only patch-tracking based methods are currently suitable for automation (S. Zheng et al., 2022).

Automated data annotation tools are key to the analysis of the growing amount of 3D image data, but a universally applicable tool is still lacking (Heebner et al., 2022). Human intervention is currently required to ensure high-quality input data, to define the analysis and to validate predictions made by automated tools. One example provided here is the U-Net based semi-automatic voxel segmentation approach in Dragonfly that requires manual training data and definition of expected classes of biological densities as well as manual editing of the model's prediction. UPICK, developed by my collaborators as a more robust and universal automatic annotation tool, aims to minimize such human input. I provided center positions of the viral D13 lattice facets from SVA as training data. While this specific way of representing a membrane-coating protein lattice yielded a valuable particle picking tool, a more generalizable tool for seamless transfer to different lattices might require a different type of lattice representation. Therefore, the next generation of the network will be trained using the electron density-based segmentation of the D13 lattice as input for the general class "protein lattice" instead of the hexamer facet center positions.

A fundamental limitation inherent to the technique of cryoET is that it provides snapshots of biological processes at high spatial resolution that are, however, quite literally frozen in time. Complementary techniques that can provide a dynamic temporal context are fluorescence-based live-cell imaging approaches, particularly super-resolution approaches like structured

illumination microscopy (SIM) (Olaya-Bravo et al., 2025). With a state-of-the-art live-cell SIM setup and a dedicated labelling strategy, the temporal progression of VACV maturation processes such as core formation could potentially be studied. Also, *in vitro* minimal systems can complement the highly complex data obtained by cryoET of intact cells for a detailed mechanistic understanding. Reconstitution of the membrane remodeling and rupture induced by poxviral VMAPs *in vitro* would provide a tractable system to study the temporal progression and gain detailed insights into the molecular mechanism.

Understanding this unique membrane rupture, stabilization and re-sealing mechanism in molecular detail promises to inform the development of specific anti-poxviral drugs. The VMAPs, which are conserved among all chordopoxviruses (Moss, 2015), are promising candidates for therapeutic intervention. In principle, druggability of the poxvirus membrane assembly pathway has long been demonstrated through the inhibition of viral assembly by the binding of rifampicin to D13. The resulting abrogation of viral scaffold formation via the D13-A17 interaction is, however, commonly met with resistance mutations (Garriga et al., 2018). As D13 is highly conserved within the genus *Orthopoxvirus*, which includes mpox and other current zoonotic threats, future drug candidates targeting the D13 scaffold assembly promise to be effective broad-spectrum anti-poxvirals. Conceivably, disturbing the inter-trimer interfaces of the native, curved D13 lattice with a small molecule would favor the formation of aberrant, flat lattices and thus block virion assembly. While the inter-trimer contacts of the hexagonal facet in the native VACV D13 lattice are described here, the structures of its alternative facet geometries remain to be determined.

To access these and to improve the resolution of the average D13 structure, the analysis will be extended to a larger *in situ* dataset in combination with a classification approach, as discussed in chapter 4.3. Complementarily, cryoET data from an *in vitro* sample of a close-to-native D13 lattice would be beneficial. Employing the described uncleavable A17 (Bisht et al., 2009) or novel mutants that stabilize the D13 lattice by strengthening the inter-trimer interactions, mutant viruses could be engineered that do not disassemble the D13 scaffold. Such stalled, coated particles would arguably be amenable to purification from infected cells for subsequent *in vitro* analysis. This would provide an advantageous signal-to-noise ratio and promises to yield structural information at a higher resolution when compared to cellular cryoET. However, analysis of such *in vitro* particles should be limited to individual facets as the overall lattice architecture is likely to be altered by the physical stresses of sample preparation such as the compression and flattening of the large, spherical viral particles in a thin film of ice (Wang et al., 2024).

An interesting future direction is to compare the VACV lattice described here with the native honeycomb lattices of related poxviruses. MPXV, but also more distantly related poxviruses outside the genus *Orthopoxvirus*, such as Yatapox, could be studied. CryoET of such poxviruses will be enabled in a biosafety level 3 facility like the one currently under construction at the CSSB. Looking beyond poxviruses, the membrane acquisition mechanism involving open membrane crescents is conserved throughout the phylum *Nucleocytoviricota*, but the membrane-scaffolding proteins and resulting capsid shapes differ vastly and are distinct from the poxviral honeycomb (E. R. Quemin et al., 2019; Rodrigues et al., 2021; Suarez et al., 2015; Suárez et al., 2013). The investigation of these membrane-shaping lattices in molecular detail by cryoET promises to reveal fundamental similarities and differences compared to the principle of open membrane stabilization and curvature induction observed for VACV D13.

6. Materials and Methods

6.1 Materials and Instruments

Table 1: list of materials and reagents used

Type	Specification	Provider
Cells	HeLa CRM-CCL-2	ATCC
Virus strains	VACV Western Reserve Recombinant A3-YFP	Michael Way Way (The Francis Crick Institute, London, UK)
	VACV Western Reserve wild type (WT)	Jacomine Krijnse-Locker (Paul-Ehrlich-Institut, Langen, Germany)
Cell culture media and additives	*Serum-free medium:* DMEM (1X) Dulbecco's Modified Eagle Medium + 4.5 g/L D-Glucose + 0.11 g/L Sodium Pyruvate	gibco
	Complete medium: DMEM + 10% (v/v) FBS + 1% (v/v) GlutaMAX	
	FBS Superior Lot 0001659021 Supplemented Fetal Bovine Serum, Brazil	Sigma
	GlutaMAX (100X) 200 mM L-alanyl-L-glutamine dipeptide	gibco
Cell culture reagents	TrypLE Express Trypsin replacement enzyme	gibco
	Dulbecco's Phosphate Buffered Saline (DPBS)	sigma
	Fibronectin used for 50 µg/mL sterile-filtered solution in DPBS	sigma
	DMSO	Roth
	PFA 4 %	Roth
CryoEM supplies	SiO_2 film R 1/4 Au 200 mesh grids	Quantifoil
	Au/Au UltrAuFoil R 0.6/1.2 200 mesh grids	Quantifoil
	Au/Au UltrAuFoil R 1.2/1.3 300 mesh grids	Quantifoil
	Autogrids modified for FIB preparation (Schaffer et al., 2015)	custom
Fluorescent dyes	Hoechst 33342 DNA dye	invitrogen
	Propidium Iodide	Merck
Cell culture dishes	µ-Slide 2 Well Co-Culture two major wells, 18 minor wells	ibidi

Table2: list of microscopes and equipment used

Type	Specification	Provider
Fluorescence light microscopes	Room temperature SP8 confocal point scanning microscope	Leica
	CryoCLEM wide field microscope	Leica
Cryo FIB-SEM systems	Aquilos2 cryo FIB-SEM with gallium beam	Thermo Fisher Scientific
	Arctis cryo FIB-SEM with plasma beam (xenon, oxygen, argon) and in-line fluorescence microscope	Thermo Fisher Scientific
Cryo TEM	Titan Krios G3 operated at 300 kV acceleration voltage and equipped with field emission gun (Thermo Fisher Scientific), BioQuantum energy filter and K3 direct electron detector (Gatan)	Thermo Fisher Scientific Bioquantum Gatan
CryoET sample preparation equipment	glow-discharging of grids in GloQube	Quorum
	sample vitrification in EM GP2 plunge freezer	Leica

6.2 Sample Preparation for cellular cryoET

6.2.1 Cell Culture

Samples for cellular cryoET were prepared from HeLa cell cultures maintained in complete medium (see **table 1**) at low passage numbers (10-30). Cells were detached from a ~ 80 % confluent culture, spun down, resuspended in complete medium and counted in a Neubauer chamber. They were then diluted to 1.6 * 10^5 cells/mL to achieve a seeding density of 148 cells/mm^2. In the minor 50 µL wells of an ibidi co-culture µ-slide, the cells were then sown onto cryoEM support grids (see **table 1**) that were previously glow-discharged for 90 s at 25 mA and coated with fibronectin. After overnight incubation at 37 °C in a controlled 5 % CO_2 environment for cell attachment, they were infected with vaccinia virus (VACV).

All samples containing VACV were kept and handled in a controlled BSL-2 environment. Concentrated stocks of purified virus (3.6 * 10^8 pfu/mL for VACV A3-YFP and 3.24 * 10^8 pfu/mL for VACV WT) were kept at -70 °C. For infection experiments, the respective virus stock solution was thawed rapidly and sonicated in a sonicator bath prior to the preparation of virus dilutions in serum-free medium. The optimized virus dilution used for A3-YFP samples corresponds to a multiplicity of infection (MOI) of 20 with regard to the seeding cell density. The WT virus was used at a lower concentration, aiming for an MOI of 10, after initial experiments with MOI 20 had shown a reduced cellular fitness on grids.

Cells were incubated with the viral inoculum for 30 min at room temperature to allow attachment of virions to the cell surface and then 15 min at 37 °C for synchronization of entry events. The inoculum was then removed and replaced with complete medium for further incubation at 37° C. This timepoint marks the beginning of the infection time and is defined here as 0 hours post infection (hpi). At 7.5 hpi the medium was changed to complete medium with 5 µg/mL of the membrane-permeable DNA dye Hoechst (compatible with live cells) for the last 30 min of incubation time.

6.2.2 Vitrification by Plunge-Freezing

At 8 hpi, the samples were vitrified by plunge-freezing in a liquid ethane-propane mixture cooled down to liquid nitrogen temperature using a Leica EM GP2 instrument. Grids were picked up out of the cell culture dish with dedicated tweezers to be locked into the plunger. A 2 µL drop of serum-free medium was applied to each grid and excess liquid subsequently removed by back-blotting, thus consistently producing a thin film of medium around the cells for optimal vitrification while avoiding any direct contact between the cells and the blotting paper. In order to reduce cell stress and enhance consistency, this was performed in the temperature- and humidity-controlled environment of the GP2 system set to 37 °C and 80 % relative humidity. Blotting times were varied in the range of 6 – 8 s. After plunge-freezing, grid samples were clipped into FIB-optimized autogrids and kept at liquid nitrogen temperature.

After plunge-freezing, the cells remaining at the bottom of the cell culture dish were chemically fixed with 4 % PFA and analyzed by confocal fluorescence microscopy as a read-out for the experiment and expected phenotypes of interest. For this purpose, one additional well of uninfected control cells (without cryoEM grids) was always included in my set-up.

6.2.3 Lamella Production

To produce electron-transparent samples of the cellular interior on the plunge-frozen grid samples, they were subjected to focused ion beam (FIB) milling. For this, three different workflows were applied in the work presented here, each accommodating different requirements for targeting the lamella production sites and employing the microscope hardware available at the CSSB multi-user cryoEM facility at the respective time (see **Table 2**).

1) <u>Correlative approach using standalone cryoCLEM wide field microscope and Aquilos2 cryo FIB-SEM:</u>

   This targeting approach was applied to HeLa cells infected with A3-YFP VACV in the early stages of the project, including those that lead to the “February” dataset presented here (tomogram names beginning with F – indicated in figure legends).

Grids were first screened using the cryo-stage of the wide field cryoCLEM microscope to acquire whole grid overview images and focus stacks at higher magnification. The reflected light channel was used for focusing and to capture the grid geometry. Hoechst-stained DNA signal was captured in the blue channel and YFP signal from the labelled viral core protein (A3-YFP recombinant virus) in the green channel. Both served to identify viral assembly sites in infected cells on the grid directly after plunge freezing.

Once samples had been transferred to the Aquilos2 cryo FIB-SEM microscope, positions of these sites were recovered through 2D image correlation between the fluorescence/reflected light grid overview images and the SEM view of the grid surface using the TFS Maps software and selected as target sites for lamella preparation and milling. Setup of target sites and milling of lamellae were automated using the autoTEM software (TFS) with milling angles ranging from 8° to 12°. Roughly milled lamellae were subsequently polished manually directly in the xT microscope user interface aiming for a final thickness of 100 – 200 nm based on visual inspection.

2) Un-targeted approach using Aquilos2 cryo FIB-SEM:

For subsequent samples of A3-YFP VACV-infected HeLa cells, including the "March" and "March2" datasets presented here (indicated with M and M2_ in figure legends), no cryoCLEM workflow was applied prior to FIB-milling. Instead, samples were directly loaded into the Aquilos2 microscope and target sites suitable for lamella preparation were selected solely based on the SEM and FIB views. Lamella preparation then proceeded as described above.

The same approach was also tested on samples of HeLa cells infected with WT VACV.

3) Correlative approach using Arctis cryo FIB-SEM with plasma beam with in-line fluorescence microscope:

The optimized workflow for preparing lamellae from WT VACV-infected HeLa cells relies on the identification of viral assembly sites based on the Hoechst signal of extranuclear viral DNA alone. For this approach, both steps of cryoCLEM targeting and lamella milling were performed in the Arctis system using the dedicated WebUI software for target site selection and automated milling. The blue channel of the integrated in-line fluorescence microscope was used to acquire grid overview tile sets for initial target selection and detailed focus stacks during target site setup for more precise lamella positioning.

Lamellae were milled at milling angles ranging from 8 ° to 15 ° using the argon plasma beam in automation using WebUI. The lamellae were manually polished in the xT microscope user interface aiming for a final thickness of 100 – 200 nm.

6.3 Fluorescence Light Microscopy

Confocal fluorescence light microscopy of chemically fixed samples at room temperature was performed as quality control for all conducted cryoET experiments as described in section 6.2.2. It was also used initially to characterize the model system here and optimize experimental procedures before adapting them to cells grown on EM grids. For this, dedicated samples were prepared in the same way as described in section 6.2.1, only without the grids to mimic the experimental conditions as closely as possible. At specific time points, cells were fixed with 4 % PFA for 10 min, stored and imaged in Hepes buffer solution. Here, seeding cell densities, MOI and incubation time were varied and optimized parameters defined (as given in section 6.2.1). During the optimization of experimental conditions for WT virus-infected samples of HeLa cells, an additional step of staining with propidium iodide (PI) was performed to check for apoptosis. For this, the cells were incubated with complete medium containing 5 µg/mL Hoechst and 2 µg/mL PI for the last 30 min before chemical fixation. The signal of PI-stained DNA in apoptotic cells was detected in the red channel. The LASX Software Suite was used for confocal microscopy data acquisition and image analysis.

6.4 cryoET Data Acquisition

Tilt series for cryoET were collected at the CSSB cryoEM multi-user facility on a Titan Krios microscope operated at an acceleration voltage of 300 kV and equipped with a BioQuantum energy filter set with a slit width of 20 eV inserted and a Gatan K3 direct detector operated in electron counting mode. All data acquisition was performed using SerialEM software (Mastronarde, 2003).

Tilt series with a nominal magnification of 42000x were acquired as dose fractionated movies with a pixel spacing of 2.121 $\frac{\text{Å}}{\text{pix}}$ and adjusted electron exposures aiming for camera dose rates of approximately 15 $\frac{\text{e}^-}{\text{pix} * \text{s}}$ over the sample. Depending on the thickness of lamellae, this resulted in total electron exposure doses of 120 to 200 $\frac{\text{e}^-}{\text{Å}^2}$ distributed over 40 - 43 tilts. The tilt series were acquired according to a dose-symmetric tilt sche (Hagen et al., 2017), starting at the effective zero tilt angle that compensates for the lamella milling angle (specific for each lamella) and covering a tilt range of ± 60 ° using 3 ° increment steps. Apertures of 50 µm for the C2 and 100 µm for the Au objective were inserted during data acquisition. The target defocus value was either set to -5 µm (February dataset) or cycled in the range of -2 to -5 µm (all other datasets).

For the WT virus-infected dataset in particular, tilt series on a given lamella were acquired in parallel employing the PACEtomo script (Eisenstein et al., 2023) implemented in SerialEM.

Overview images acquired at a nominal magnification of 3600x were saved using SerialEM implementation for all lamellae prior to high-magnification data acquisition of tilt series. On a selection of lamellae, low-magnification tilt series for so-called “overview tomograms” were acquired employing a custom script developed by Robert Gebauer and Vojtěch Pražák in the group.

6.5 cryoET Data Processing Pipelines

6.5.1 Pre-Processing, Tomogram Reconstruction and Filtering

Dose-fractionated movie frames were aligned and saved as motion-corrected tilt images by SerialEM during data acquisition employing an implementation of motioncor2 (S. Q. Zheng et al., 2017). Tilt series were then visually inspected to exclude dark images from alignment and tomogram reconstruction. Tilt series were aligned based on patch tracking using AreTomo (S. Zheng et al., 2022) and reconstructed with a binning factor of 4 or 8 for analysis. Tilt series with promising content that also had trackable gold or platinum specks were carefully aligned based on manual tracking of these fiducial markers in IMOD and reconstructed with 3D CTF corrected weighted back projection (wbp) (Mastronarde & Held, 2017; Turoňová et al., 2017). Such 3D CTF-corrected tomograms destined for subvolume averaging were reconstructed at the un-binned pixel size of 2.1 Å, from which binned versions of the tomograms were generated with binning factors 2, 4 and 8.

For better visualization, a SIRT-like filter equivalent to 5 – 15 iterations was applied during reconstruction. Tomograms reconstructed through wbp without SIRT-like filtering were filtered with a SIRT-like filter using the program mtffilter or CTF-deconvoluted using the deconv module from the software package IsoNet (Y. Liu et al., 2022). Notably, options in IsoNet for missing wedge compensation were not used in the work presented here. Most of the data displayed in this thesis were reconstructed in IMOD based on careful manual fiducial alignment, reconstructed with wbp, binned by a factor of 4 and subsequently deconvoluted with isonet. Tomographic data is visualized as 2D slices through the volume data viewed with 3dmod or Dragonfly software.

6.5.2 Segmentations

Segmentation for 3D rendering of the biological entities contained in a tomographic volume were performed on bin4 tomograms filtered by isonet deconvolution. Automatic membrane segmentations were performed on these tomograms using memBrain-seg (Lamm et al., 2024) based on the recent pre-trained segmentation model checkpoints v9_b and v10_alpha available from the authors’ GitHub page. After manual cleaning in Dragonfly, these predicted membrane segmentations were used as input for downstream analysis (1) and the development of custom semi-automatic multi-class segmentation workflows (2).

For (1), triangular membrane surface meshes were constructed from the memBrain membrane segmentation masks using the surface morphometrics toolkit developed by (Barad et al., 2023). Within the morphometrics toolkit, local membrane curvature was calculated for these membrane meshes using the provided wrapper for the pyCurv algorithm (Salfer et al., 2020). In paraview, the polygon mesh representations of segmented membranes were visualized and colour-coded according to the local curvedness of the membrane in nm^{-1} as determined through vector voting by pyCurv.

For more comprehensive multi-class segmentations of whole tomogram volumes (2), I developed a custom semi-automatic segmentation workflow using the Dragonfly software suite and its integrated deep-learning tool similar to the one published in (Heebner et al., 2022). The basis for these segmentations were high-magnification tomograms at a binned pixel spacing of 8.484 Å and filtered with isonet deconvolution. Tomograms had to be imported into Dragonfly with an axis transformation to mitigate a stitching error that consistently occurred specifically with isonet-treated tomograms. This error must originate from an incompatibility between isonet and Dragonfly in writing and reading the image data matrices, resulting in an observed frameshift in the x dimension. An axis transformation during import resolved the frameshift and was then reversed using the "modify and transform" functions within Dragonfly to arrive back at the familiar axis assignment with the xy plane representing the plane of the lamella, i.e. being in plane with the tilt axis of the microscope and the z axis being perpendicular to the tilt axis. After import into Dragonfly, tomograms were calibrated according to the mode and standard deviation of their intensity value histogram and additionally filtered using histogram equalization, Gaussian filtering and unsharpening. To train a convolutional neural network of a 5 layer 2.5D U-Net architecture for the prediction of whole tomogram segmentations, training data was annotated in a defined region of interest (ROI) of the tomogram. Initially, this was done on the tomogram M2_027. The corresponding membrane segmentation mask predicted by memBrain was also imported into Dragonfly, converted into a multi-ROI and used as membrane class for training after some manual corrections. Additional classes were added to the multi-ROI for the viral D13 scaffold, microtubules and actin filaments and manually segmented in a small ROI within the tomogram. Manual segmentation steps were performed using Dragonfly's ROI painter tool with local Otsu thresholding. All un-labelled voxels were then added to a background class and the completely annotated multi-ROI used as input for training the first U-Net. Optimal training parameters were a data augmentation value of 12, box size 64 x 64 voxels and batch size 64, in combination with custom class weights in the range of 1 – 10. The trained model was then applied to the whole tomogram to predict segmentations. Cleaning of the predicted multi-class segmentations and subsequent re-training were used in an iterative manner to improve these

prediction models. Final segmentation cleaning steps included setting a minimum threshold of 5000 voxels for each connected component using the “process islands” function and re-assigning mis-labelled voxels in between classes.

Once generated and trained on the data of the M2_027 tomogram, the network was applied to different tomograms from the same and different datasets. In some cases, a re-training of the network on the new dataset was required to improve the prediction performance. Depending on the biological content of different tomograms, different models with more (additionally including ribosomes and the viral genome) or less classes (only membranes and the viral D13 scaffold) were generated and trained. The number of classes to be segmented is an inherent property of the model and cannot be changed once a model is created.

6.5.3 Subvolume Averaging

SVA of the D13 protein was performed on a selection of tomograms reconstructed after motion-correction, fine alignment and 3D CTF-correction (see above). My custom workflow for particle picking and data processing is outlined in **figure M1** and described in chapter 3.5 of the results. Additional details related to specific processing aspects are provided in the following text. All SVA was performed in PEET in combination with custom TEMPy-based (Cragnolini et al., 2021) python scripts developed in the group by Vojtěch Pražák and Daven Vashistan, referred to as *pex_script_name*. Further operations on volumes and model files were done using the IMOD suite and Bsoft software.

Duplicates and misaligning particles were removed using *pex_remove_duplicates* with suitable maximal neighbor distances and cross correlation thresholds. Aligned particles were visualized after plot back as pin models for inspection in ChimeraX (Pettersen et al., 2004) using *pex_make_chim_markers_from_prm*. For the final SVA alignment, picked particles were split into half-sets using *pex_split_for_FSC*. C6 symmetry was applied using *pex_symmetrise* once it became apparent in averages, un-symmetrized initially. The Fourier Shell Correlation (FSC) between the independently refined half-maps was calculated with *simpleFSC* and the resolution determined at the 0.143 threshold. The two half-maps were combined using *clipvol* and filtered with B-factor sharpening using *bfilter* to apply a B-factor of -2000 and a high-resolution cutoff of 17.5 Å. Average volumes are visualized as 2D slices in 3dmod (see e.g. **figure S2**). For isosurface representations in ChimeraX, the contrast of the average volumes was inverted. Rigid body fitting of the D13 trimer crystal structure (pdb 3saq) was performed in ChimeraX using the *fit in map* volume tool.

Plotback of an unsymmetrized average into the tomogram coordinate system based on the positions and orientations of particles after alignment was performed using *pex_plotback*. The resulting lattice representation was visualized in ChimeraX (see **figure 15**).

For the deep learning-based particle picking employed here, aligned D13 positions were used to train UPICK, a Bayesian Flow network developed by Dr. Manaz Khaleel, Dr. Joseph Beton and Dr. Fabian Hausmann in the laboratory of Prof. Maya Topf at CSSB, Hamburg, Germany. Model training on D13 particles and first predictions were performed by J. Beton. The trained version of the model was fixed by J. Beton under the name UPICK-v2 and subsequently used by me for further predictions with the support of F. Hausmann. To translate the UPICK-v2 output into PEET-readable particles for SVA, I developed the following workflow employing custom scripting: Segmentation masks predicted by UPICK-v2 were first thresholded to extract only the level corresponding to the D13 class using *bmask* and then scaled back to the original bin4 tomogram pixel spacing using *squeezevol*. To extract the coordinates of the center position, i.e. the coordinates of the picked particle in the tomogram coordinate system, the D13 mask was skeletonized using the *skimage a*nd *mrc* packages in python. The skeleton of a binary volume that contains isolated spheres is a set of isolated points, each in the center of one sphere. As some of the annotated spheres corresponding to neighboring D13 facets in the mask file were touching each other, they could not be separated in the skeletonization, resulting in artefactual points in the output. To avoid this, an erosion step using *bmask* was introduced into the workflow prior to skeletonization. In 2 iterations of mask erosion, voxels from the edges of each masked volume were removed, effectively shrinking the spheres and removing the artefactual bridges between neighboring spheres. The xyz coordinates from the mask's skeleton were then written as an IMOD-readable text file which was then converted into an IMOD model file using the *point2model* function. The resulting file was used as an input model file for subvolume averaging in PEET together with an initial motive list generated using *pex_make_model_using_centres*.

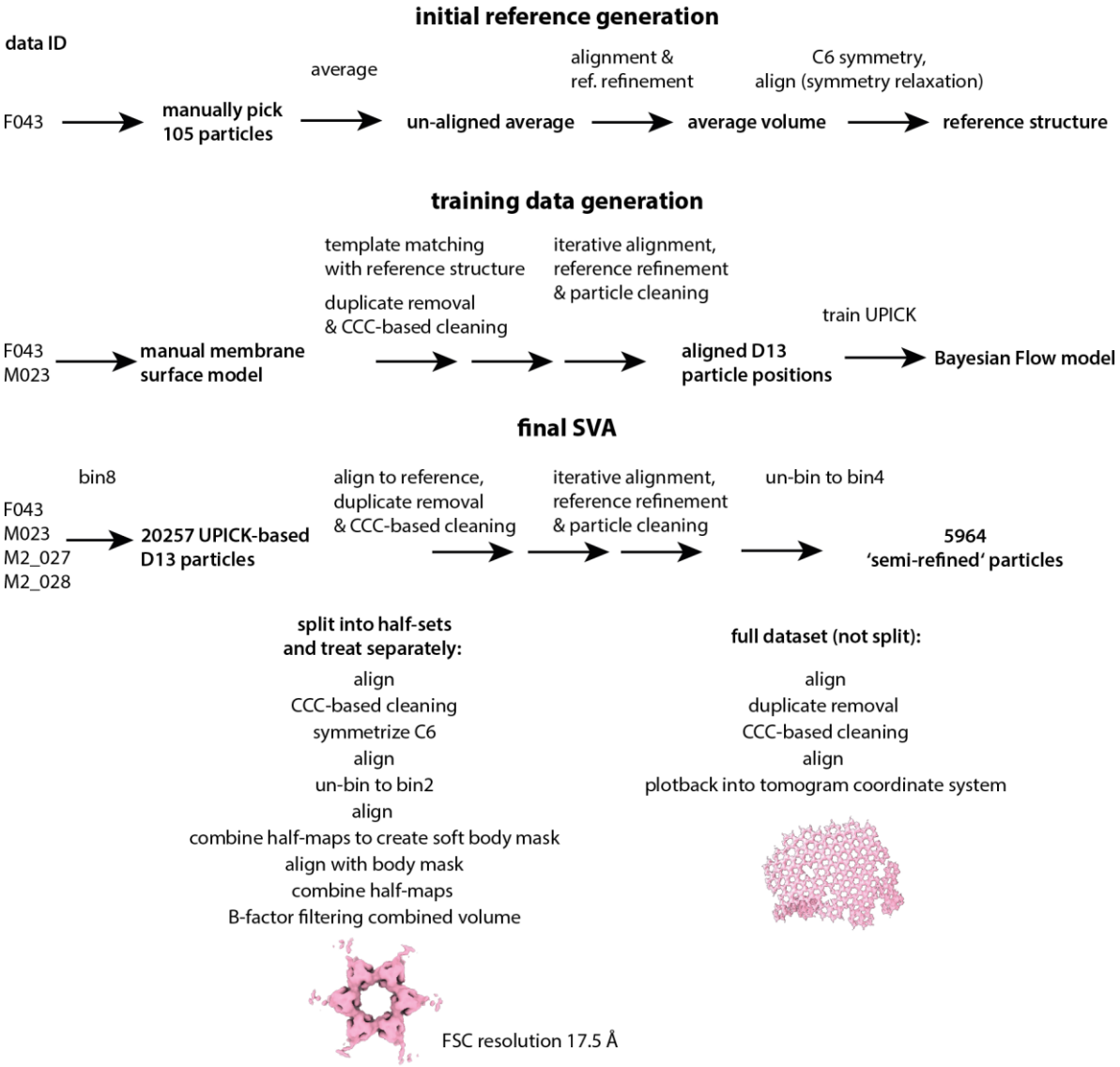

Figure M1: Subvolume averaging workflow applied to the D13 hexamer of the viral protein scaffold.

6.6 Tomograms shown in the Thesis

Table 3: Tomograms shown throughout the thesis and corresponding imaging parameters

Data ID	date	virus	Sample ID	Pix. Size (Å)	De-focus (µm)	dose ($\frac{e^-}{Å^2}$)	Alignment and reconstruction	Thickness (nm)	Milling angle	tilts	Used for
F043	14. 02. 2023	A3-YFP	C10_2	2.212	-5	134	IMOD fiducial	215	10.2 °	40	D13 SVA, seg
F044						134	IMOD fiducial	225	10.2 °	40	D13 SVA, genome
F045						134	IMOD fiducial	205	10.2 °	40	D13 SVA
F046						134	IMOD fiducial	215	10.2 °	40	D13 SVA, genome
F047						134	IMOD fiducial	190	10.2 °	40	D13 SVA, genome
F048						160	IMOD fiducial	250	10.2 °	40	D13 SVA, genome
F052						157	AreTomo patch	270	9 °	39	Figure S3
M003	08. 03. 2023		C10_3		-3.5	185	IMOD fiducial	160	11.8 °	41	D13 SVA, genome
M008					-2.75	200	IMOD fiducial	180	9.3 °	42	seg
M009					-3.5	190	AreTomo patch	180	9.3 °	40	Maturation analysis
M021	09. 03. 2023				-3.5	190	IMOD fiducial	180	8 °	42	D13 SVA, Seg, Genome
M022					-2	200	AreTomo patch	180	8 °	44	Maturation analysis
M023					-2.75	200	IMOD fiducial	180	8 °	43	D13 SVA, Seg, pycurv
M026					-5	190	AreTomo patch	150	8 °	42	genome
M036					-2.75	214	AreTomo patch	130	10.5 °	45	Figure S3
M2_ 027	29. 03. 2023		C11_3		-4	167	IMOD fiducial	100	9.9 °	42	D13 SVA, Seg, pycurv
M2_ 028					-5	167	IMOD fiducial	100	9.9 °	42	D13 SVA, seg
M2_031	30. 03. 2023				-4	167	AreTomo patch	100	9.9 °	42	Maturation analysis
M2_047					-4	167	IMOD fiducial	210	10 °	43	Maturation analysis
WT1_ 009	09. 09. 2024	WT	C18_2	2.150	-5	131	IMOD fiducial	205	9 °	43	Figure S1
WT1_ 016					-5	219	IMOD fiducial	375	12 °	36	Figure S1
WT1_ 026			C19_2		-5	131	AreTomo patch	155	12 °	43	Figure S1

7. References

Adrian, M., Dubochet, J., Lepault, J., & McDowall, A. W. (1984). Cryo-electron microscopy of viruses. *Nature*, *308*(5954), 32–36. https://doi.org/10.1038/308032a0

Antun, V., Renna, F., Poon, C., Adcock, B., & Hansen, A. C. (2020). On instabilities of deep learning in image reconstruction and the potential costs of AI. *Proceedings of the National Academy of Sciences*, *117*(48), 30088–30095. https://doi.org/10.1073/pnas.1907377117

Arakawa, Y., Cordeiro, J. V., Schleich, S., Newsome, T. P., & Way, M. (2007). The Release of Vaccinia Virus from Infected Cells Requires RhoA-mDia Modulation of Cortical Actin. *Cell Host & Microbe*, *1*(3), 227–240. https://doi.org/10.1016/j.chom.2007.04.006

Ayache, J., Beaunier, L., Boumendil, J., Ehret, G., & Laub, D. (2010). *Sample Preparation Handbook for Transmission Electron Microscopy*. Springer New York. https://doi.org/10.1007/978-1-4419-5975-1

Aylward, F. O., Moniruzzaman, M., Ha, A. D., & Koonin, E. V. (2021). A phylogenomic framework for charting the diversity and evolution of giant viruses. *PLOS Biology*, *19*(10), e3001430. https://doi.org/10.1371/journal.pbio.3001430

Bahar, M. W., Graham, S. C., Stuart, D. I., & Grimes, J. M. (2011). Insights into the evolution of a complex virus from the crystal structure of vaccinia virus D13. *Structure*, *19*(7), 1011–1020. https://doi.org/10.1016/j.str.2011.03.023

Baker, L. A., Grange, M., & Grünewald, K. (2017). Electron cryo-tomography captures macromolecular complexes in native environments. *Current Opinion in Structural Biology*, *46*, 149–156. https://doi.org/10.1016/j.sbi.2017.08.005

Barad, B. A., Medina, M., Fuentes, D., Wiseman, R. L., & Grotjahn, D. A. (2023). Quantifying organellar ultrastructure in cryo-electron tomography using a surface morphometrics pipeline. *Journal of Cell Biology*, *222*(4). https://doi.org/10.1083/jcb.202204093

Bauer, D. W., Li, D., Huffman, J., Homa, F. L., Wilson, K., Leavitt, J. C., Casjens, S. R., Baines, J., & Evilevitch, A. (2015). Exploring the Balance between DNA Pressure and Capsid Stability in Herpesviruses and Phages. *Journal of Virology*, *89*(18), 9288–9298. https://doi.org/10.1128/JVI.01172-15

Bausch, A. R., Bowick, M. J., Cacciuto, A., Dinsmore, A. D., Hsu, M. F., Nelson, D. R., Nikolaides, M. G., Travesset, A., & Weitz, D. A. (2003). Grain Boundary Scars and Spherical Crystallography. *Science*, *299*(5613), 1716–1718. https://doi.org/10.1126/science.1081160

Berger, C., Dumoux, M., Glen, T., Yee, N. B. y., Mitchels, J. M., Patáková, Z., Darrow, M. C., Naismith, J. H., & Grange, M. (2023). Plasma FIB milling for the determination of structures in situ. *Nature Communications*, *14*(1), 1–12. https://doi.org/10.1038/s41467-023-36372-9

Bhadra, S., Kelkar, V. A., Brooks, F. J., & Anastasio, M. A. (2021). On Hallucinations in Tomographic Image Reconstruction. *IEEE Transactions on Medical Imaging*, *40*(11), 3249–3260. https://doi.org/10.1109/TMI.2021.3077857

Bidgood, S., & Mercer, J. (2015). Cloak and Dagger: Alternative Immune Evasion and Modulation Strategies of Poxviruses. *Viruses*, *7*(8), 4800–4825. https://doi.org/10.3390/v7082844

Bisht, H., Weisberg, A. S., Szajner, P., & Moss, B. (2009). Assembly and Disassembly of the Capsid-Like External Scaffold of Immature Virions during Vaccinia Virus Morphogenesis. *Journal of Virology*, *83*(18), 9140–9150. https://doi.org/10.1128/jvi.00875-09

Boltje, D. B., Hoogenboom, J. P., Jakobi, A. J., Jensen, G. J., Jonker, C. T. H., Kaag, M. J., Koster, A. J., Last, M. G. F., Pinto, C. de A., Plitzko, J. M., Raunser, S., Tacke, S., Wang, Z., van der Wee, E. B., Wepf, R., & Hoedt, S. Den. (2022). A cryogenic, coincident fluorescence, electron and ion beam microscope. *ELife*, *11*, 1–18. https://doi.org/10.7554/eLife.82891

Boneš, E., Khan, D., Bohak, C., Barad, B. A., Grotjahn, D. A., Viola, I., & Theußl, T. (2024). *MidSurfer: A Parameter-Free Approach for Mid-Surface Extraction from Segmented Volumetric Data*. 1–20. http://arxiv.org/abs/2405.19339

Boylston, A. (2012). The origins of inoculation. *Journal of the Royal Society of Medicine*, *105*(7), 309–313. https://doi.org/10.1258/jrsm.2012.12k044

Brüssow, H. (2025). Monkeypox Virus: WHO ’s Second Public Health Emergency of International Concern Within 2 Years. *Microbial Biotechnology*, *18*(4). https://doi.org/10.1111/1751-7915.70142

Caplan, A., & Mamo, N. (2024). The challenging concept of eradication: A core concept guiding and frustrating public health. *Canadian Journal of Public Health*, 109–112. https://doi.org/10.17269/s41997-024-00947-w

Cassetti, M. C., Merchlinsky, M., Wolffe, E. J., Weisberg, A. S., & Moss, B. (1998). DNA Packaging Mutant: Repression of the Vaccinia Virus A32 Gene Results in Noninfectious, DNA-Deficient, Spherical, Enveloped Particles. *Journal of Virology*, *72*(7), 5769–5780. https://doi.org/10.1128/jvi.72.7.5769-5780.1998

Chenchula, S., Atal, S., Krishna, M., Rao, C., Karunakaran, S., Chaitanya, K., Sarma, P., Prakash, S., Sahitya, L., Padmavathi, R., Anitha, K., Varshini, T. S., Vardhan, K. V., Kaore, S., & Sadasivam, B. (2025). Emerging variants of Mpox virus and tecovirimat resistance : Genomic insights and implications for treatment strategies. *Virology*, *608*(December 2024), 110532. https://doi.org/10.1016/j.virol.2025.110532

Chlanda, P., Carbajal, M. A., Cyrklaff, M., Griffiths, G., & Krijnse-Locker, J. (2009). Membrane Rupture Generates Single Open Membrane Sheets during Vaccinia Virus Assembly. *Cell Host & Microbe*, *6*(1), 81–90. https://doi.org/10.1016/j.chom.2009.05.021

Condit, R. C., Moussatche, N., & Traktman, P. (2006). *In A Nutshell: Structure and Assembly of the Vaccinia Virion* (pp. 31–124). https://doi.org/10.1016/S0065-3527(06)66002-8

Cragnolini, T., Sahota, H., Joseph, A. P., Sweeney, A., Malhotra, S., Vasishtan, D., & Topf, M. (2021). TEMPy 2: a Python library with improved 3D electron microscopy density-fitting and validation workflows. *Acta Crystallographica Section D Structural Biology*, *77*(1), 41–47. https://doi.org/10.1107/S2059798320014928

Creekmore, B. C., Kixmoeller, K., Black, B. E., Lee, E. B., & Chang, Y. W. (2024). Ultrastructure of human brain tissue vitrified from autopsy revealed by cryo-ET with cryo-plasma FIB milling. *Nature Communications*, *15*(1), 1–12. https://doi.org/10.1038/s41467-024-47066-1

Cyrklaff, M., Risco, C., Fernández, J. J., Jiménez, M. V., Estéban, M., Baumeister, W., & Carrascosa, J. L. (2005). Cryo-electron tomography of vaccinia virus. *Proceedings of the National Academy of Sciences of the United States of America*, *102*(8), 2772–2777. https://doi.org/10.1073/pnas.0409825102

Dales, S., & Mosbach, E. H. (1968). Vaccinia as a Model for Membrane Biogenesis'. In *VIROLOGY* (Vol. 36).

Damaso, C. R. (2018). Revisiting Jenner's mysteries, the role of the Beaugency lymph in the evolutionary path of ancient smallpox vaccines. *The Lancet Infectious Diseases*, *18*(2), e55–e63. https://doi.org/10.1016/S1473-3099(17)30445-0

Danita, C., Chiu, W., & Galaz-Montoya, J. G. (2022). Efficient manual annotation of cryogenic electron tomograms using IMOD. *STAR Protocols*, *3*(3). https://doi.org/10.1016/j.xpro.2022.101658

Datler, J., Hansen, J. M., Thader, A., Schlögl, A., Bauer, L. W., Hodirnau, V.-V., & Schur, F. K. M. (2024). Multi-modal cryo-EM reveals trimers of protein A10 to form the palisade layer in poxvirus cores. *Nature Structural & Molecular Biology*, *31*(7), 1114–1123. https://doi.org/10.1038/s41594-023-01201-6

Deng, Y., Navarro-Forero, S., & Yang, Z. (2025). Temporal expression classes and functions of vaccinia virus and mpox (monkeypox) virus genes. *MBio*, *16*(4). https://doi.org/10.1128/mbio.03809-24

Dhungel, P., Cantu, F. M., Molina, J. A., & Yang, Z. (2020). Vaccinia Virus as a Master of Host Shutoff Induction: Targeting Processes of the Central Dogma and Beyond. *Pathogens*, *9*(5), 400. https://doi.org/10.3390/pathogens9050400

Dubochet, J. (2012). Cryo-EM-the first thirty years. *Journal of Microscopy*, *245*(3), 221–224. https://doi.org/10.1111/j.1365-2818.2011.03569.x

Egerton, R. F. (2016). *Physical Principles of Electron Microscopy*. Springer International Publishing. https://doi.org/10.1007/978-3-319-39877-8

Eisenstein, F., Yanagisawa, H., Kashihara, H., Kikkawa, M., Tsukita, S., & Danev, R. (2023). Parallel cryo electron tomography on in situ lamellae. *Nature Methods*, *20*(1), 131–138. https://doi.org/10.1038/s41592-022-01690-1

El-Jesr, M., Teir, M., & Maluquer de Motes, C. (2020). Vaccinia Virus Activation and Antagonism of Cytosolic DNA Sensing. *Frontiers in Immunology*, *11*(October). https://doi.org/10.3389/fimmu.2020.568412

Esparza, J., Schrick, L., Damaso, C. R., & Nitsche, A. (2017). Equination (inoculation of horsepox): An early alternative to vaccination (inoculation of cowpox) and the potential role of horsepox virus in the origin of the smallpox vaccine. In *Vaccine* (Vol. 35, Issue 52, pp. 7222–7230). Elsevier Ltd. https://doi.org/10.1016/j.vaccine.2017.11.003

Fatehi, F., & Twarock, R. (2023). An interaction network approach predicts protein cage architectures in bionanotechnology. *Proceedings of the National Academy of Sciences of the United States of America*, *120*(50), 1–8. https://doi.org/10.1073/pnas.2303580120

Faul, N., Chen, S.-Y., Lamberz, C., Bruckner, M., Dienemann, C., & Burg, T. P. (2025). Cryo-iCLEM: Cryo correlative light and electron microscopy with immersion objectives. *Journal of Structural Biology*, *217*(1), 108179. https://doi.org/10.1016/j.jsb.2025.108179

Fenner, F., Henderson, D. A., Arita, I., Jezek, Z., & Ladnyi, I. D. (1988). Smallpox and its eradication. In *World Health Organization*. https://jech.bmj.com/lookup/doi/10.1136/jech.43.1.92

Frangakis, A. S. (2021). It's noisy out there! A review of denoising techniques in cryo-electron tomography. In *Journal of Structural Biology* (Vol. 213, Issue 4). Academic Press Inc. https://doi.org/10.1016/j.jsb.2021.107804

Franken, L. E., Grünewald, K., Boekema, E. J., & Stuart, M. C. A. (2020). A Technical Introduction to Transmission Electron Microscopy for Soft-Matter: Imaging, Possibilities, Choices, and Technical Developments. *Small*, *16*(14). https://doi.org/10.1002/smll.201906198

Garriga, D., Headey, S., Accurso, C., Gunzburg, M., Scanlon, M., & Coulibaly, F. (2018). Structural basis for the inhibition of poxvirus assembly by the antibiotic rifampicin. *Proceedings of the National Academy of Sciences of the United States of America*, *115*(33), 8424–8429. https://doi.org/10.1073/pnas.1810398115

Glingston, R. S., Deb, R., Kumar, S., & Nagotu, S. (2019). Organelle dynamics and viral infections: at cross roads. In *Microbes and Infection* (Vol. 21, Issue 1, pp. 20–32). Elsevier Masson SAS. https://doi.org/10.1016/j.micinf.2018.06.002

Glon, D., Léonardon, B., Guillemot, A., Albertini, A., Lagaudrière-Gesbert, C., & Gaudin, Y. (2024). Biomolecular condensates with liquid properties formed during viral infections. *Microbes and Infection*, *26*(8), 105402. https://doi.org/10.1016/j.micinf.2024.105402

Greseth, M. D., & Traktman, P. (2022). The Life Cycle of the Vaccinia Virus Genome. *Annual Review of Virology*, *9*(1), 239–259. https://doi.org/10.1146/annurev-virology-091919-104752

Grimm, C., Bartuli, J., & Fischer, U. (2022). Cytoplasmic gene expression: lessons from poxviruses. *Trends in Biochemical Sciences*, *47*(10), 892–902. https://doi.org/10.1016/j.tibs.2022.04.010

Grünewald, K., Desai, P., Winkler, D. C., Heymann, J. B., Belnap, D. M., Baumeister, W., & Steven, A. C. (2003). Three-Dimensional Structure of Herpes Simplex Virus from Cryo-Electron Tomography. *Science*, *302*(5649), 1396–1398. https://doi.org/10.1126/science.1090284

Grünewald, K., Medalia, O., Gross, A., Steven, A. C., & Baumeister, W. (2002). Prospects of electron cryotomography to visualize macromolecular complexes inside cellular compartments: implications of crowding. *Biophysical Chemistry*, *100*(1–3), 577–591. https://doi.org/10.1016/S0301-4622(02)00307-1

Hagen, W. J. H., Wan, W., & Briggs, J. A. G. (2017). Implementation of a cryo-electron tomography tilt-scheme optimized for high resolution subtomogram averaging. *Journal of Structural Biology*, *197*(2), 191–198. https://doi.org/10.1016/j.jsb.2016.06.007

Hassan, Z., Kumar, N. D., Reggiori, F., & Khan, G. (2021). How Viruses Hijack and Modify the Secretory Transport Pathway. *Cells*, *10*(10), 2535. https://doi.org/10.3390/cells10102535

Heebner, J. E., Purnell, C., Hylton, R. K., Marsh, M., Grillo, M. A., & Swulius, M. T. (2022). Deep Learning-Based Segmentation of Cryo-Electron Tomograms. *Journal of Visualized Experiments*, *2022*(189), 1–14. https://doi.org/10.3791/64435

Hernandez-Gonzalez, M., Calcraft, T., Nans, A., Rosenthal, P. B., & Way, M. (2023). A succession of two viral lattices drives vaccinia virus assembly. *PLOS Biology*, *21*(3), e3002005. https://doi.org/10.1371/journal.pbio.3002005

Heuser, J. (2005). Deep-etch EM reveals that the early poxvirus envelope is a single membrane bilayer stabilized by a geodetic “honeycomb” surface coat. *The Journal of Cell Biology*, *169*(2), 269–283. https://doi.org/10.1083/jcb.200412169

Hong, Y., Huang, B., Zhang, J., Peng, C., Kong, W., Tan, W., & Li, S. (2024). Molecular architecture of monkeypox mature virus. *Cell Discovery*, *10*(1), 108. https://doi.org/10.1038/s41421-024-00741-5

Hyun, J.-K., Accurso, C., Hijnen, M., Schult, P., Pettikiriarachchi, A., Mitra, A. K., & Coulibaly, F. (2011). Membrane Remodeling by the Double-Barrel Scaffolding Protein of Poxvirus. *PLoS Pathogens*, *7*(9), e1002239. https://doi.org/10.1371/journal.ppat.1002239

Hyun, J., Matsunami, H., Kim, T. G., & Wolf, M. (2022). Assembly mechanism of the pleomorphic immature poxvirus scaffold. *Nature Communications*, *13*(1). https://doi.org/10.1038/s41467-022-29305-5

Indelicato, G., Cermelli, P., & Twarock, R. (2020). Surface stresses in complex viral capsids and non-quasi-equivalent viral architectures. *Journal of The Royal Society Interface*, *17*(169), 20200455. https://doi.org/10.1098/rsif.2020.0455

Jacobs, B. L., Langland, J. O., Kibler, K. V., Denzler, K. L., White, S. D., Holechek, S. A., Wong, S., Huynh, T., & Baskin, C. R. (2009). Vaccinia virus vaccines: Past, present and future. *Antiviral Research*, *84*(1), 1–13. https://doi.org/10.1016/j.antiviral.2009.06.006

Kelley, K., Raczkowski, A. M., Klykov, O., Jaroenlak, P., Bobe, D., Kopylov, M., Eng, E. T., Bhabha, G., Potter, C. S., Carragher, B., & Noble, A. J. (2022). Waffle Method: A general and flexible approach for improving throughput in FIB-milling. *Nature Communications*, *13*(1), 1–13. https://doi.org/10.1038/s41467-022-29501-3

Kinman, L. F., Powell, B. M., Zhong, E. D., Berger, B., & Davis, J. H. (2023). Uncovering structural ensembles from single-particle cryo-EM data using cryoDRGN. *Nature Protocols*, *18*(2), 319–339. https://doi.org/10.1038/s41596-022-00763-x

Klein, S., Wimmer, B. H., Winter, S. L., Kolovou, A., Laketa, V., & Chlanda, P. (2021). Post-correlation on-lamella cryo-CLEM reveals the membrane architecture of lamellar bodies. *Communications Biology*, *4*(1), 137. https://doi.org/10.1038/s42003-020-01567-z

Klumpe, S., Senti, K. A., Beck, F., Sachweh, J., Hampoelz, B., Ronchi, P., Oorschot, V., Brandstetter, M., Yeroslaviz, A., Briggs, J. A. G., Brennecke, J., Beck, M., & Plitzko, J. M. (2025). In-cell structure and snapshots of copia retrotransposons in intact tissue by cryo-ET. *Cell*, *188*(8), 2094-2110.e18. https://doi.org/10.1016/j.cell.2025.02.003

Koonin, E. V, Dolja, V. V, Krupovic, M., Varsani, A., Wolf, Y. I., Yutin, N., Zerbini, F. M., & Kuhn, J. H. (2020). *Global Organization and Proposed Megataxonomy of the Virus World*. https://doi.org/10

Kreysing, J. P., Heidari, M., Zila, V., Cruz-León, S., Obarska-Kosinska, A., Laketa, V., Rohleder, L., Welsch, S., Köfinger, J., Turoňová, B., Hummer, G., Kräusslich, H.-G., & Beck, M. (2025). Passage of the HIV capsid cracks the nuclear pore. *Cell*, *188*(4), 930-943.e21. https://doi.org/10.1016/j.cell.2024.12.008

Kudryashev, M. (2024). The big chill: Growth of in situ structural biology with cryo-electron tomography. *QRB Discovery*, *5*, e10. https://doi.org/10.1017/qrd.2024.10

Lamm, L., Zufferey, S., Righetto, R. D., Wietrzynski, W., Yamauchi, K. A., Burt, A., Liu, Y., Zhang, H., Martinez-Sanchez, A., Ziegler, S., Isensee, F., Schnabel, J. A., Engel, B. D., & Peng, T. (2024). MemBrain v2: an end-to-end tool for the analysis of membranes in cryo-electron tomography. In *BioRxiv*. https://doi.org/10.1101/2024.01.05.574336

Li, S., Wang, Z., Jia, X., Niu, T., Zhang, J., Yin, G., Zhang, X., Zhu, Y., Ji, G., & Sun, F. (2023). ELI trifocal microscope: a precise system to prepare target cryo-lamellae for in situ cryo-ET study. *Nature Methods*, *20*(2), 276–283. https://doi.org/10.1038/s41592-022-01748-0

Liu, J., Corroyer-Dulmont, S., Pražák, V., Khusainov, I., Bahrami, K., Welsch, S., Vasishtan, D., Obarska-Kosińska, A., Thorkelsson, S. R., Grünewald, K., Quemin, E. R. J., Turoňová, B., & Locker, J. K. (2024). The palisade layer of the poxvirus core is composed of flexible A10 trimers. *Nature Structural & Molecular Biology*, *31*(7), 1105–1113. https://doi.org/10.1038/s41594-024-01218-5

Liu, L., Cooper, T., Howley, P., & Hayball, J. (2014). From Crescent to Mature Virion: Vaccinia Virus Assembly and Maturation. *Viruses*, *6*(10), 3787–3808. https://doi.org/10.3390/v6103787

Liu, Y., Zhang, H., Wang, H., Tao, C., Bi, G., & Zhou, Z. H. (2022). Isotropic reconstruction for electron tomography with deep learning. *Nature Communications*, *13*(1), 6482. https://doi.org/10.1038/s41467-022-33957-8

Lucas, B. A., & Grigorieff, N. (2023). Quantification of gallium cryo-FIB milling damage in biological lamellae. *Proceedings of the National Academy of Sciences*, *120*(23), 2017. https://doi.org/10.1073/pnas.2301852120

Maruri-Avidal, L., Weisberg, A. S., & Moss, B. (2011). Vaccinia Virus L2 Protein Associates with the Endoplasmic Reticulum near the Growing Edge of Crescent Precursors of Immature Virions and Stabilizes a Subset of Viral Membrane Proteins. *Journal of Virology*, *85*(23), 12431–12441. https://doi.org/10.1128/JVI.05573-11

Maruri-Avidal, L., Weisberg, A. S., & Moss, B. (2013a). Association of the Vaccinia Virus A11 Protein with the Endoplasmic Reticulum and Crescent Precursors of Immature Virions. *Journal of Virology*, *87*(18), 10195–10206. https://doi.org/10.1128/JVI.01601-13

Maruri-Avidal, L., Weisberg, A. S., & Moss, B. (2013b). Direct Formation of Vaccinia Virus Membranes from the Endoplasmic Reticulum in the Absence of the Newly Characterized L2-Interacting Protein A30.5. *Journal of Virology*, *87*(22), 12313–12326. https://doi.org/10.1128/JVI.02137-13

Massey, T. H., Mercogliano, C. P., Yates, J., Sherratt, D. J., & Löwe, J. (2006). Double-Stranded DNA Translocation: Structure and Mechanism of Hexameric FtsK. *Molecular Cell*, *23*(4), 457–469. https://doi.org/10.1016/j.molcel.2006.06.019

Mastronarde, D. N. (2003). SerialEM: A Program for Automated Tilt Series Acquisition on Tecnai Microscopes Using Prediction of Specimen Position. *Microscopy and Microanalysis*, *9*(S02), 1182–1183. https://doi.org/10.1017/S1431927603445911

Mastronarde, D. N., & Held, S. R. (2017). Automated tilt series alignment and tomographic reconstruction in IMOD. *Journal of Structural Biology*, *197*(2), 102–113. https://doi.org/10.1016/j.jsb.2016.07.011

Meng, X., Embry, A., Rose, L., Yan, B., Xu, C., & Xiang, Y. (2012). Vaccinia Virus A6 Is Essential for Virion Membrane Biogenesis and Localization of Virion Membrane Proteins to Sites of Virion Assembly. *Journal of Virology*, *86*(10), 5603–5613. https://doi.org/10.1128/JVI.00330-12

Monticelli, S. R., Earley, A. K., Stone, R., Norbury, C. C., & Ward, B. M. (2020). Vaccinia Virus Glycoproteins A33, A34, and B5 Form a Complex for Efficient Endoplasmic Reticulum to trans -Golgi Network Transport. *Journal of Virology*, *94*(7). https://doi.org/10.1128/JVI.02155-19

Moser, F., Prazák, V., Mordhorst, V., Andrade, D. M., Baker, L. A., Hagen, C., Grünewald, K., & Kaufmann, R. (2019). Cryo-SOFI enabling low-dose super-resolution correlative light and electron cryo-microscopy. *Proceedings of the National Academy of Sciences of the United States of America*, *116*(11), 4804–4809. https://doi.org/10.1073/pnas.1810690116

Moss, B. (2015). Poxvirus membrane biogenesis. *Virology*, *479–480*, 619–626. https://doi.org/10.1016/j.virol.2015.02.003

Moss, B. (2016). Membrane fusion during poxvirus entry. *Seminars in Cell & Developmental Biology*, *60*, 89–96. https://doi.org/10.1016/j.semcdb.2016.07.015

Moss, B. (2018). Origin of the poxviral membrane: A 50-year-old riddle. *PLOS Pathogens*, *14*(6), e1007002. https://doi.org/10.1371/journal.ppat.1007002

Motsa, B. B., & Stahelin, R. V. (2021). Lipid–protein interactions in virus assembly and budding from the host cell plasma membrane. *Biochemical Society Transactions*, *49*(4), 1633–1641. https://doi.org/10.1042/BST20200854

Moussatche, N., & Condit, R. C. (2015). Fine structure of the vaccinia virion determined by controlled degradation and immunolocalization. *Virology*, *475*, 204–218. https://doi.org/10.1016/j.virol.2014.11.020

Nguyen, H. T. D., Perone, G., Klena, N., Vazzana, R., Kaluthantrige Don, F., Silva, M., Sorrentino, S., Swuec, P., Leroux, F., Kalebic, N., Coscia, F., & Erdmann, P. S. (2024). Serialized on-grid lift-in sectioning for tomography (SOLIST) enables a biopsy at the nanoscale. *Nature Methods*, *21*(9), 1693–1701. https://doi.org/10.1038/s41592-024-02384-6

Olaya-Bravo, K., Martínez-Flores, D., Rodríguez-Hernández, A. P., Tobías-Juárez, I., Castro-Rodríguez, J. A., Sampieri, A., & Vaca, L. (2025). Resolving viral structural complexity by super-resolution microscopy. *Archives of Virology*, *170*(1), 5. https://doi.org/10.1007/s00705-024-06192-3

Olson, V., & Shchelkunov, S. (2017). Are We Prepared in Case of a Possible Smallpox-Like Disease Emergence? *Viruses*, *9*(9), 242. https://doi.org/10.3390/v9090242

Pajak, J., Prokhorov, N. S., Jardine, P. J., & Morais, M. C. (2024). The mechano-chemistry of a viral genome packaging motor. *Current Opinion in Structural Biology*, *89*, 102945. https://doi.org/10.1016/j.sbi.2024.102945

PALM007 Writing Group, Ali, R., Alonga, J., Biampata, J.-L., Kombozi Basika, M., Maljkovic Berry, I., Bisento, N., Blum, E., Bonnett, T., Cone, K., Crozier, I., Davey, R., Dilu, A., Dodd, L. E., Gulati, I., Hruby, D., Ibanda, A., Isse, F., Kasareka, S. S., … Weyers, S. (2025). Tecovirimat for Clade I MPXV Infection in the Democratic Republic of Congo. *New England Journal of Medicine*, *392*(15), 1484–1496. https://doi.org/10.1056/NEJMoa2412439

Pathak, P. K., Peng, S., Meng, X., Han, Y., Zhang, B., Zhang, F., Xiang, Y., & Deng, J. (2018). Structure of a lipid-bound viral membrane assembly protein reveals a modality for enclosing the lipid bilayer. *Proceedings of the National Academy of Sciences*, *115*(27), 7028–7032. https://doi.org/10.1073/pnas.1805855115

Patwardhan, A., Henderson, R., & Russo, C. J. (2025). Extending the reach of single-particle cryoEM. *Current Opinion in Structural Biology*, 103005. https://doi.org/10.1016/j.sbi.2025.103005

Pettersen, E. F., Goddard, T. D., Huang, C. C., Couch, G. S., Greenblatt, D. M., Meng, E. C., & Ferrin, T. E. (2004). UCSF Chimera—A visualization system for exploratory research and analysis. *Journal of Computational Chemistry*, *25*(13), 1605–1612. https://doi.org/10.1002/jcc.20084

Pierson, J., Vos, M., McIntosh, J. R., & Peters, P. J. (2011). Perspectives on electron cryo-tomography of vitreous cryo-sections. *Microscopy*, *60*(suppl 1), S93–S100. https://doi.org/10.1093/jmicro/dfr014

Prasad, B. V. V., Wang, G. J., Clerx, J. P. M., & Chiu, W. (1988). Three-dimensional structure of rotavirus. *Journal of Molecular Biology*, *199*(2), 269–275. https://doi.org/10.1016/0022-2836(88)90313-0

Pražák, V., Mironova, Y., Vasishtan, D., Hagen, C., Laugks, U., Jensen, Y., Sanders, S., Heumann, J. M., Bosse, J. B., Klupp, B. G., Mettenleiter, T. C., Grange, M., & Grünewald, K. (2024). Molecular plasticity of herpesvirus nuclear egress analysed in situ. *Nature Microbiology*, *9*(7), 1842–1855. https://doi.org/10.1038/s41564-024-01716-8

Pyle, E., & Zanetti, G. (2021). Current data processing strategies for cryo-electron tomography and subtomogram averaging. *Biochemical Journal*, *478*(10), 1827–1845. https://doi.org/10.1042/BCJ20200715

Quemin, E. R., Corroyer-Dulmont, S., Baskaran, A., Penard, E., Gazi, A. D., Christo-Foroux, E., Walther, P., Abergel, C., & Krijnse-Locker, J. (2019). Complex Membrane Remodeling during Virion Assembly of the 30,000-Year-Old Mollivirus Sibericum. *Journal of Virology*, *93*(13), 1–19. https://doi.org/10.1128/JVI.00388-19

Quemin, E. R. J., Machala, E. A., Vollmer, B., Pražák, V., Vasishtan, D., Rosch, R., Grange, M., Franken, L. E., Baker, L. A., & Grünewald, K. (2020). Cellular Electron Cryo-Tomography to Study Virus-Host Interactions. *Annual Review of Virology*, *7*(1), 239–262. https://doi.org/10.1146/annurev-virology-021920-115935

Ramakrishnan, U., Aggarwal, T., & Kondabagil, K. (2024). Sequence and Biochemical Analysis of Vaccinia Virus A32 Protein: Implications for in vitro Stability and Coiled-Coil Motif Mediated Regulation of the DNA-Dependent ATPase Activity. *Preprints*, 1–15. https://doi.org/10.1371/journal.pone.0316818

Ramakrishnan, U., Aggarwal, T., & Kondabagil, K. (2025). Sequence and biochemical analysis of vaccinia virus A32 protein: Implications for in vitro stability and coiled-coil motif mediated regulation of the DNA-dependent ATPase activity. *PLOS ONE*, *20*(1), e0316818. https://doi.org/10.1371/journal.pone.0316818

Resch, W., Weisberg, A. S., & Moss, B. (2005). Vaccinia Virus Nonstructural Protein Encoded by the A11R Gene Is Required for Formation of the Virion Membrane. *Journal of Virology*, *79*(11), 6598–6609. https://doi.org/10.1128/jvi.79.11.6598-6609.2005

Rheinemann, L., Downhour, D. M., Bredbenner, K., Mercenne, G., Davenport, K. A., Schmitt, P. T., Necessary, C. R., McCullough, J., Schmitt, A. P., Simon, S. M., Sundquist, W. I., & Elde, N. C. (2021). RetroCHMP3 blocks budding of enveloped viruses without blocking cytokinesis. *Cell*, *184*(21), 5419-5431.e16. https://doi.org/10.1016/j.cell.2021.09.008

Rigort, A., Bauerlein, F. J. B., Villa, E., Eibauer, M., Laugks, T., Baumeister, W., & Plitzko, J. M. (2012). Focused ion beam micromachining of eukaryotic cells for cryoelectron tomography. *Proceedings of the National Academy of Sciences*, *109*(12), 4449–4454. https://doi.org/10.1073/pnas.1201333109

Rigou, S., Schmitt, A., Moreno, A. B., Lartigue, A., Danner, L., Giry, C., Trabelsi, F., Belmudes, L., Olivero-Deibe, N., Guenno, H. Le, Couté, Y., Berois, M., Legendre, M., Jeudy, S., Abergel, C., & Bisio, H. (2024). *Nucleocytoviricota viral factories are transient organelles made by liquid-liquid phase separation*. https://doi.org/10.1101/2024.09.01.610734

Risco, C., Rodríguez, J. R., López-Iglesias, C., Carrascosa, J. L., Esteban, M., & Rodríguez, D. (2002). Endoplasmic Reticulum-Golgi Intermediate Compartment Membranes and Vimentin Filaments Participate in Vaccinia Virus Assembly. *Journal of Virology*, *76*(4), 1839–1855. https://doi.org/10.1128/JVI.76.4.1839-1855.2002

Rodrigues, R. AL, de Souza, F. G., de Azevedo, B. L., da Silva, L. C., & Abrahão, J. S. (2021). The morphogenesis of different giant viruses as additional evidence for a common origin of Nucleocytoviricota. *Current Opinion in Virology*, *49*, 102–110. https://doi.org/10.1016/j.coviro.2021.05.004

Roingeard, P., Eymieux, S., Burlaud-Gaillard, J., Hourioux, C., Patient, R., & Blanchard, E. (2022). The double-membrane vesicle (DMV): a virus-induced organelle dedicated to the replication of SARS-CoV-2 and other positive-sense single-stranded RNA viruses. *Cellular and Molecular Life Sciences*, *79*(8), 425. https://doi.org/10.1007/s00018-022-04469-x

Ronneberger, O., Fischer, P., & Brox, T. (2015). U-Net: Convolutional Networks for Biomedical Image Segmentation. In N. Navab, J. Hornegger, W. M. Wells, & A. F. Frangi (Eds.), *Medical Image Computing and Computer-Assisted Intervention – MICCAI 2015. MICCAI 2015. Lecture Notes in Computer Science* (Vol. 9351, Issue Cvd). Springer International Publishing. https://doi.org/10.1007/978-3-319-24574-4

Ruma, Y. N., Nannenga, B. L., & Gonen, T. (2025). Unraveling atomic complexity from frozen samples. *Structural Dynamics*, *12*(2), 1–8. https://doi.org/10.1063/4.0000303

Russo, C. J., Dickerson, J. L., & Naydenova, K. (2022). Cryomicroscopy in situ : what is the smallest molecule that can be directly identified without labels in a cell? *Faraday Discussions*, *240*, 277–302. https://doi.org/10.1039/D2FD00076H

Salfer, M., Collado, J. F., Baumeister, W., FernándezBusnadiego, R., & Martínez-Sánchez, A. (2020). Reliable estimation of membrane curvature for cryo-electron tomography. *PLoS Computational Biology*, *16*(8), 1–29. https://doi.org/10.1371/journal.pcbi.1007962

Schaffer, M., Engel, B., Laugks, T., Mahamid, J., Plitzko, J., & Baumeister, W. (2015). Cryo-focused Ion Beam Sample Preparation for Imaging Vitreous Cells by Cryo-electron Tomography. *BIO-PROTOCOL*, *5*(17). https://doi.org/10.21769/BioProtoc.1575

Schauflinger, M., Villinger, C., Mertens, T., Walther, P., & von Einem, J. (2013). Analysis of human cytomegalovirus secondary envelopment by advanced electron microscopy. *Cellular Microbiology*, *15*(2), 305–314. https://doi.org/10.1111/cmi.12077

Schmidt, F. I., Bleck, C. K. E., Helenius, A., & Mercer, J. (2011). Vaccinia extracellular virions enter cells by macropinocytosis and acid-activated membrane rupture. *The EMBO Journal*, *30*(17), 3647–3661. https://doi.org/10.1038/emboj.2011.245

Schur, F. K. M., Hagen, W. J. H., Rumlová, M., Ruml, T., Müller, B., Kräusslich, H.-G., & Briggs, J. A. G. (2015). Structure of the immature HIV-1 capsid in intact virus particles at 8.8 Å resolution. *Nature*, *517*(7535), 505–508. https://doi.org/10.1038/nature13838

Sexton, D. L., Burgold, S., Schertel, A., & Tocheva, E. I. (2022). Super-resolution confocal cryo-CLEM with cryo-FIB milling for in situ imaging of Deinococcus radiodurans. *Current Research in Structural Biology*, *4*(November 2021), 1–9. https://doi.org/10.1016/j.crstbi.2021.12.001

Sivan, G., Weisberg, A. S., Americo, J. L., & Moss, B. (2016). Retrograde Transport from Early Endosomes to the trans -Golgi Network Enables Membrane Wrapping and Egress of Vaccinia Virus Virions. *Journal of Virology*, *90*(19), 8891–8905. https://doi.org/10.1128/JVI.01114-16

Suarez, C., Andres, G., Kolovou, A., Hoppe, S., Salas, M. L., Walther, P., & Krijnse Locker, J. (2015). African swine fever virus assembles a single membrane derived from rupture of the endoplasmic reticulum. *Cellular Microbiology*, *17*(11), 1683–1698. https://doi.org/10.1111/cmi.12468

Suárez, C., Welsch, S., Chlanda, P., Hagen, W., Hoppe, S., Kolovou, A., Pagnier, I., Raoult, D., & Krijnse Locker, J. (2013). Open membranes are the precursors for assembly of large DNA viruses. *Cellular Microbiology*, *15*(11), n/a-n/a. https://doi.org/10.1111/cmi.12156

Szajner, P., Weisberg, A. S., Lebowitz, J., Heuser, J., & Moss, B. (2005). External scaffold of spherical immature poxvirus particles is made of protein trimers, forming a honeycomb lattice. *Journal of Cell Biology*, *170*(6), 971–981. https://doi.org/10.1083/jcb.200504026

Talbert, P. B., Henikoff, S., & Armache, K.-J. (2023). Giant variations in giant virus genome packaging. *Trends in Biochemical Sciences*, *48*(12), 1071–1082. https://doi.org/10.1016/j.tibs.2023.09.003

Tan, A., Pak, A. J., Morado, D. R., Voth, G. A., & Briggs, J. A. G. (2021). Immature HIV-1 assembles from Gag dimers leaving partial hexamers at lattice edges as potential substrates for proteolytic maturation. *Proceedings of the National Academy of Sciences*, *118*(3). https://doi.org/10.1073/pnas.2020054118

Tegunov, D., & Cramer, P. (2019). Real-time cryo-electron microscopy data preprocessing with Warp. *Nature Methods*, *16*(11), 1146–1152. https://doi.org/10.1038/s41592-019-0580-y

Tolonen, N., Doglio, L., Schleich, S., & Locker, J. K. (2001). Vaccinia Virus DNA Replication Occurs in Endoplasmic Reticulum-enclosed Cytoplasmic Mini-Nuclei. *Molecular Biology of the Cell*, *12*(7), 2031–2046. https://doi.org/10.1091/mbc.12.7.2031

Tsuji, C., Bradshaw, M., Allen, M. F., Jackson, M. L., Mantell, J., Borucu, U., Poole, A. W., Verkade, P., Hers, I., Paul, D. M., & Dodding, M. P. (2024). CryoET reveals actin filaments within platelet microtubules. *Nature Communications*, *15*(1), 5967. https://doi.org/10.1038/s41467-024-50424-8

Tuijtel, M. W., Cruz-León, S., Kreysing, J. P., Welsch, S., Hummer, G., Beck, M., & Turoňová, B. (2024). Thinner is not always better: Optimizing cryo-lamellae for subtomogram averaging. *Science Advances*, *10*(17), 1–10. https://doi.org/10.1126/sciadv.adk6285

Turk, M., & Baumeister, W. (2020). The promise and the challenges of cryo-electron tomography. *FEBS Letters*, *594*(20), 3243–3261. https://doi.org/10.1002/1873-3468.13948

Turoňová, B., Schur, F. K. M., Wan, W., & Briggs, J. A. G. (2017). Efficient 3D-CTF correction for cryo-electron tomography using NovaCTF improves subtomogram averaging resolution to 3.4 Å. *Journal of Structural Biology*, *199*(3), 187–195. https://doi.org/10.1016/j.jsb.2017.07.007

Twarock, R., & Luque, A. (2019). Structural puzzles in virology solved with an overarching icosahedral design principle. *Nature Communications*, *10*(1), 4414. https://doi.org/10.1038/s41467-019-12367-3

Vallbracht, M., Bodmer, B. S., Fischer, K., Makroczyova, J., Winter, S. L., Wendt, L., Wachsmuth-Melm, M., Hoenen, T., & Chlanda, P. (2025). Nucleocapsid assembly drives Ebola viral factory maturation and dispersion. *Cell*, *188*(3), 704-720.e17. https://doi.org/10.1016/j.cell.2024.11.024

van Helvoort, T., & Sankaran, N. (2019). How Seeing Became Knowing: The Role of the Electron Microscope in Shaping the Modern Definition of Viruses. *Journal of the History of Biology*, *52*(1), 125–160. https://doi.org/10.1007/s10739-018-9530-2

Van Veen, D., Galaz-Montoya, J. G., Shen, L., Baldwin, P., Chaudhari, A. S., Lyumkis, D., Schmid, M. F., Chiu, W., & Pauly, J. (2024). Missing Wedge Completion via Unsupervised Learning with Coordinate Networks. *International Journal of Molecular Sciences*, *25*(10), 5473. https://doi.org/10.3390/ijms25105473

Veratti, P., Wyler, E., Read, C., Scherer, M., Tan, J., Walther, P., Wider, S., Weidl, D., & Full, F. (2024). Poxviruses induce a nuclear environment in the cytoplasm to promote viral replication. In *bioRxiv : the preprint server for biology* (Vol. 15, Issue 1, pp. 37–48). https://doi.org/10.1101/2024.11.21.624458

Villa, E., Schaffer, M., Plitzko, J. M., & Baumeister, W. (2013). Opening windows into the cell: focused-ion-beam milling for cryo-electron tomography. *Current Opinion in Structural Biology*, *23*(5), 771–777. https://doi.org/10.1016/j.sbi.2013.08.006

Volz, A., & Sutter, G. (2017). Modified Vaccinia Virus Ankara: History, Value in Basic Research, and Current Perspectives for Vaccine Development. In *Advances in Virus Research* (Vol. 97, pp. 187–243). Academic Press Inc. https://doi.org/10.1016/bs.aivir.2016.07.001

Wang, H., Liao, S., Yu, X., Zhang, J., & Zhou, Z. H. (2024). TomoNet: A streamlined cryogenic electron tomography software pipeline with automatic particle picking on flexible lattices. *Biological Imaging*, *4*. https://doi.org/10.1017/s2633903x24000060

Ward, B. M. (2005). Visualization and Characterization of the Intracellular Movement of Vaccinia Virus Intracellular Mature Virions. *Journal of Virology*, *79*(8), 4755–4763. https://doi.org/10.1128/JVI.79.8.4755-4763.2005

Weisberg, A. S., Maruri-Avidal, L., Bisht, H., Hansen, B. T., Schwartz, C. L., Fischer, E. R., Meng, X., Xiang, Y., & Moss, B. (2017). Enigmatic origin of the poxvirus membrane from the endoplasmic reticulum shown by 3D imaging of vaccinia virus assembly mutants. *Proceedings of the National Academy of Sciences*, *114*(51), E11001–E11009. https://doi.org/10.1073/pnas.1716255114

Wiedemann, S., & Heckel, R. (2024). A deep learning method for simultaneous denoising and missing wedge reconstruction in cryogenic electron tomography. *Nature Communications*, *15*(1), 8255. https://doi.org/10.1038/s41467-024-51438-y

Wu, M., & Lander, G. C. (2020). How low can we go? Structure determination of small biological complexes using single-particle cryo-EM. *Current Opinion in Structural Biology*, *64*, 9–16. https://doi.org/10.1016/j.sbi.2020.05.007

Wu, X., Meng, X., Yan, B., Rose, L., Deng, J., & Xiang, Y. (2012). Vaccinia Virus Virion Membrane Biogenesis Protein A11 Associates with Viral Membranes in a Manner That Requires the Expression of Another Membrane Biogenesis Protein, A6. *Journal of Virology*, *86*(20), 11276–11286. https://doi.org/10.1128/JVI.01502-12

Yang, Z., Gray, M., & Winter, L. (2021). Why do poxviruses still matter? *Cell & Bioscience*, *11*(1), 96. https://doi.org/10.1186/s13578-021-00610-8

Zhao, G., Perilla, J. R., Yufenyuy, E. L., Meng, X., Chen, B., Ning, J., Ahn, J., Gronenborn, A. M., Schulten, K., Aiken, C., & Zhang, P. (2013). Mature HIV-1 capsid structure by cryo-electron microscopy and all-atom molecular dynamics. *Nature*, *497*(7451), 643–646. https://doi.org/10.1038/nature12162

Zhao, S., Miao, C., Gao, X., Li, Z., Eriksson, J. E., & Jiu, Y. (2024). Vimentin cage – A double-edged sword in host anti-infection defense. *Current Opinion in Cell Biology*, *86*, 102317. https://doi.org/10.1016/j.ceb.2023.102317

Zheng, S. Q., Palovcak, E., Armache, J.-P., Verba, K. A., Cheng, Y., & Agard, D. A. (2017). MotionCor2: anisotropic correction of beam-induced motion for improved cryo-electron microscopy. *Nature Methods*, *14*(4), 331–332. https://doi.org/10.1038/nmeth.4193

Zheng, S., Wolff, G., Greenan, G., Chen, Z., Faas, F. G. A., Bárcena, M., Koster, A. J., Cheng, Y., & Agard, D. A. (2022). AreTomo: An integrated software package for automated marker-free, motion-corrected cryo-electron tomographic alignment and reconstruction. *Journal of Structural Biology: X*, *6*(April). https://doi.org/10.1016/j.yjsbx.2022.100068

Zimmermann, L., Zhao, X., Makroczyova, J., Wachsmuth-Melm, M., Prasad, V., Hensel, Z., Bartenschlager, R., & Chlanda, P. (2023). SARS-CoV-2 nsp3 and nsp4 are minimal constituents of a pore spanning replication organelle. *Nature Communications*, *14*(1), 7894. https://doi.org/10.1038/s41467-023-43666-5

8. Supplement

8.1 Supplementary Figures

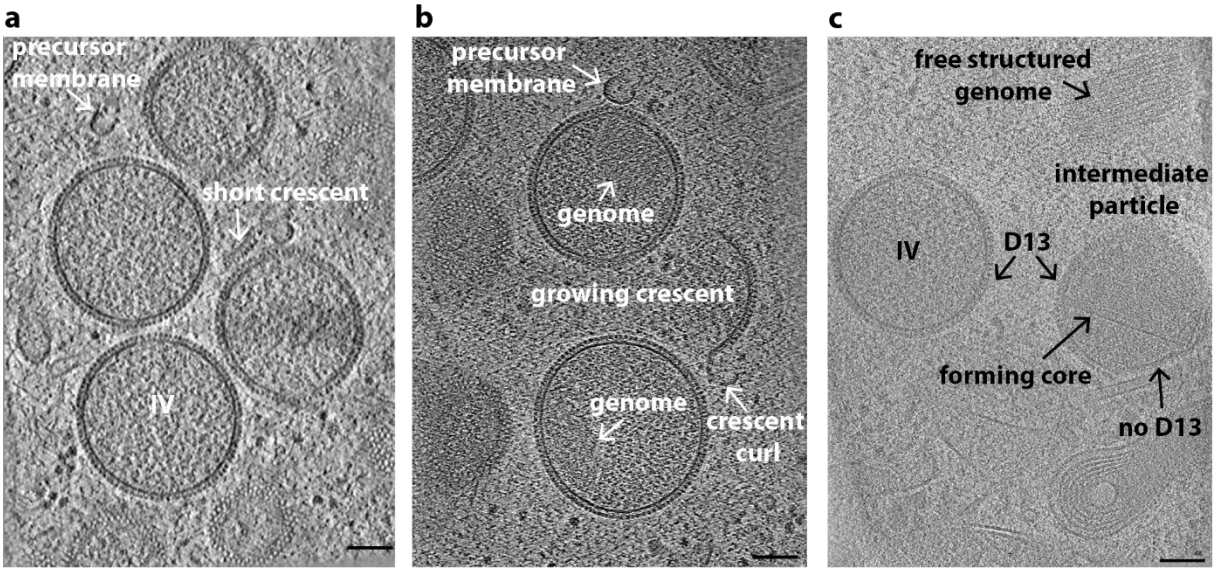

Figure S1: Assembly intermediates and precursor membranes of wild-type VACV: structures analogous to those observed in A3-YFP labelled virus can be identified in tomographic slices of wild-type VACV infected HeLa cells. Panels a), b), c) show slices of tomograms WT1_009, WT1_026, WT1_016, that were filtered using isonet deconvolution, SART-like filtering in AreTomo and SIRT-like filtering in IMOD, respectively. All scale bars indicate 100 nm.

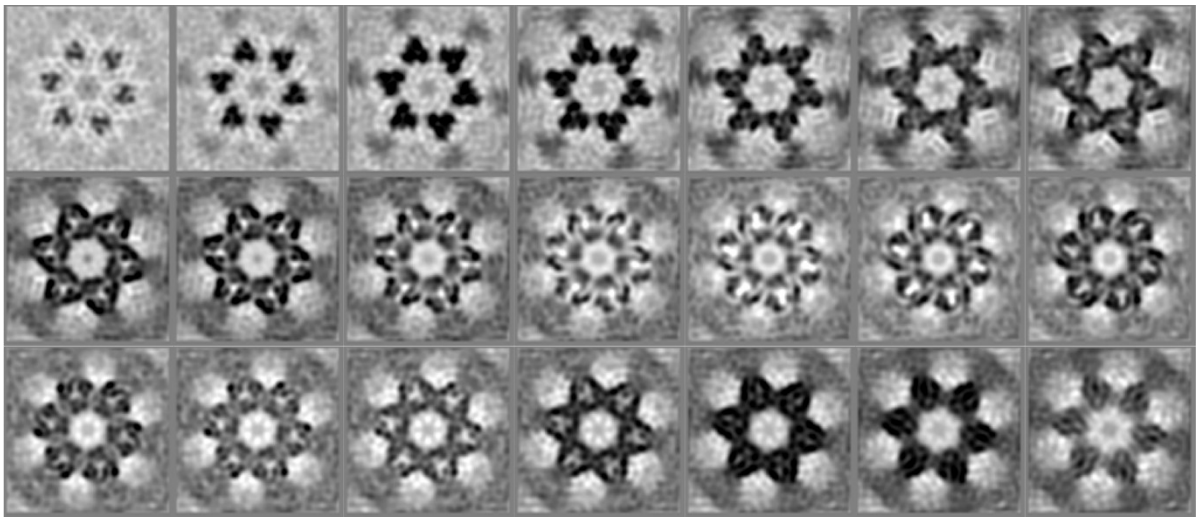

Figure S2: Slices through the average D13 hexamer volume obtained by SVA (see figures 17, M1) filtered to 17.5 Å resolution with B-factor sharpening. Shown are slices through the volume from the top of the structure (top left panel) to the bottom (bottom right panel).

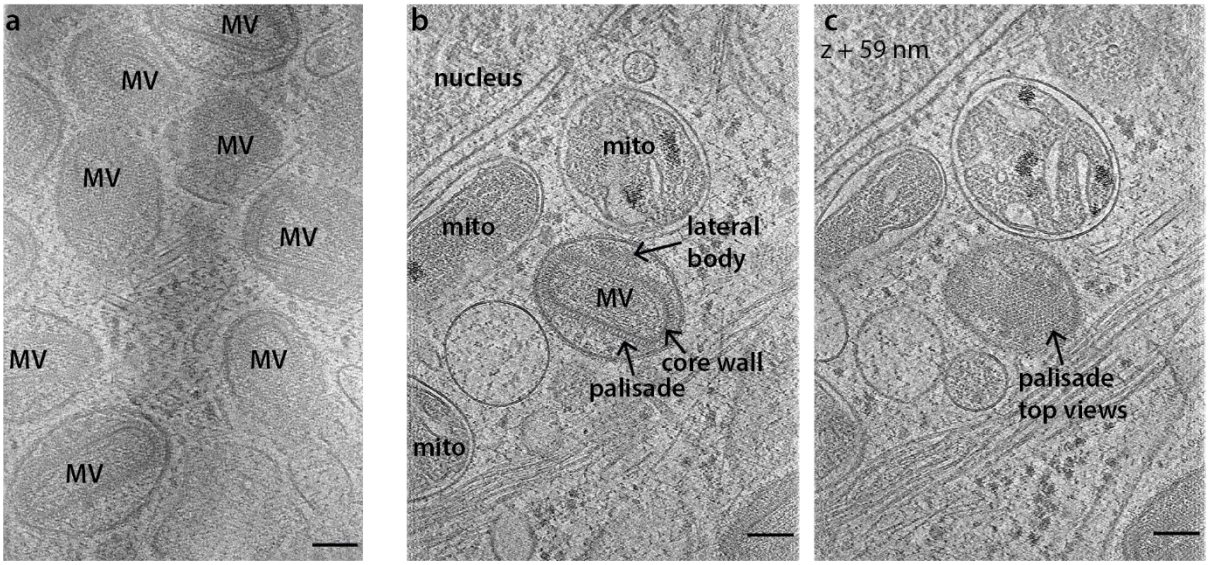

Figure S3: mature A3-YFP VACV particles observed inside infected cells: Tomographic slices show various individual mature virions with complete internal core structures and lateral bodies. Not all cores appear to be dumbbell shaped. Panel a) is taken from tomogram F052, b, c) from M036. c) shows top views of the core palisade in a slice 59 nm above the one in b). All scale bars represent 100 nm.

8.2 List of Hazardous Substances

Table 4: Hazardous substances in the context of this thesis

Substance	GHS symbol	Hazard statements	Precautionary statements
Paraformaldehyde 4%		317, 318, 351	280, 302 + 352, 305 + 351 + 338, 310
Liquid nitrogen		281	282, 336 + 315, 403
Ethane/propane mix		220, 280	210, 377, 381, 403, 410 + 403
Cis-platinum		300, 315, 317, 319, 334, 335, 350	201, 280, 301 + 310, 302 + 352, 304 + 340 + 312
Argon		280	403
OPTISEPT (glyoxal, didecyldimethyl-ammoniumchloride, formaldehyde, glutaral)		302 + 332, 314, 334, 317, 341, 350, 335, 410	202, 260, 280, 303 + 361 + 353, 304 + 340, 305 + 351 + 338, 308 + 313, 405, 501
Bacillol AF (propanol, isopropanol, ethanol)		226, 318, 336	102, 210, 261, 280, 305 + 351 + 338 + 310, 501

Acknowledgements

This thesis would not have been possible without the support of many people to whom I am deeply grateful.

Firstly, I would like to thank my supervisors, Kay and Emmanuelle, for giving me the opportunity to work on this project and for providing such a great environment in which to do so. It has been a pleasure working with you ever since I started my first internship with you as a Master's student, and I have always enjoyed our scientific discussions. Thank you also for your support beyond the science itself, for your mentorship, and for encouraging me to take on growth opportunities.

Thank you, Charlotte, for taking on the role of co-supervisor and always offering valuable feedback and support.

I would like to thank all the current and former group members of the SCBV team who have shared this time with me and made it so valuable – especially Simon, Yuliia, Vojta, Jan, Dounia, Uli, Tim, Emily, Henriette, Roberto, Ben and Siggi. Thank you for the countless exciting discussions about science, for your help, teaching and advice, and for the great conversations and fun times, both at work and beyond.

The same goes for the RAPUS group at I2BC: Thank you, Pavlina, Marcel, Chloé and Sandra for welcoming me to Paris and Gif and sharing the excitement about poxvirus research.

Thank you Uli, Cornelia, Carolin and Roland for running the CSSB cryoEM and ALFM multi-user facilities and for all the microscope training and support you gave me.

Susanne, thank you for your administrative support.

As collaborators, I thank Maya, Joe, Fabian and Manaz for taking me along on the UPICK journey and letting me use it as a particle picking tool.

I also want to thank Fasséli Coulibaly and Reidun Twarock for our inspiring discussions on D13 and its lattice defect lines. Further, I thank Benjamin Barad for introducing me to segmentations with Dragonfly at the U Michigan Summer School last year.

My final "thank you" goes to my family and friends who accompanied me throughout this time, celebrating the highs and picking me up in the lower moments. Especially to you, Robert. I don't know how I could have possibly done this without you.

Eidesstattliche Versicherung

Hiermit versichere ich an Eides statt, die vorliegende Dissertationsschrift selbst verfasst und keine anderen als die angegebenen Quellen und Hilfsmittel benutzt zu haben. Sofern im Zuge der Erstellung der vorliegenden Dissertationsschrift generative Künstliche Intelligenz (gKI) basierte elektronische Hilfsmittel verwendet wurden, versichere ich, dass meine eigene Leistung im Vordergrund stand und dass eine vollständige Dokumentation aller verwendeten Hilfsmittel gemäß der Guten wissenschaftlichen Praxis vorliegt. Ich trage die Verantwortung für eventuell durch die gKI generierte fehlerhafte oder verzerrte Inhalte, fehlerhafte Referenzen, Verstöße gegen das Datenschutz- und Urheberrecht oder Plagiate.
Ich versichere die inhaltliche und formale Gleichheit der eingereichten Print- und Digitalexemplare.

Clara Andrea Feldmann

Hamburg, 16.07.2025